

①

AFIT/GAE/ENY/92D-27

**AD-A259 146**



A COMPARISON OF COMPUTATIONAL FLUID  
DYNAMICS COMPUTER PROGRAMS FOR HYPERSONIC  
PROPULSIVE NOZZLE FLOWFIELDS

THESIS

Kennedy B. Wilson Jr., Captain, USAF

AFIT/GAE/ENY/92D-27

**DTIC**  
**S** **E** **D**  
ELECTE  
JAN 1 1993

0/2225  
**93-00078**



12/85

Approved for public release; distribution unlimited

93 1 4 7 4 21

AFIT/GAE/ENY/92D-27

A COMPARISON OF COMPUTATIONAL FLUID DYNAMICS COMPUTER  
PROGRAMS FOR HYPERSONIC PROPULSIVE NOZZLE FLOWFIELDS

THESIS

Presented to the Faculty of the School of Engineering  
of the Air Force Institute of Technology  
Air University  
In Partial Fulfillment of the  
Requirements for the Degree of  
Master of Science in Aeronautical Engineering

Kennedy B. Wilson Jr., B.S.  
Captain, USAF

December 1992

Approved for public release; distribution unlimited

### Acknowledgements

I would like to thank my advisor, Captain John Doty, for his guidance and instruction throughout the preparation of this thesis. His interest and knowledge in the subject was inspiring and he was always there. Additionally, I would like to express thanks to Captain Sandra Snelling whose advice and instruction on using the SCHNOZ code was invaluable.

I thank my parents for always supporting me in everything. I am happy to know that my thesis will sit side-by-side with my father's gathering dust on an AFIT library bookshelve in the years to come. I am even more glad that my mother will be able to read this - of course she'll find it incredibly boring - for she has taught me more in my life than I have ever learned elsewhere. And most of all, I would like to thank my wonderful wife, and best friend, Angelica for encouraging me and keeping me sane during the last few months.

Accession For	
NTIS CRA&I	<input checked="checked" type="checkbox"/>
DTIC TAB	<input type="checkbox"/>
Unannounced	<input type="checkbox"/>
Justification	
By	
Distribution /	
Availability Codes	
Dist	Avail and/or Special
A-1	

## Table of Contents

Acknowledgements . . . . .	ii
List of Figures . . . . .	v
List of Tables . . . . .	viii
List of Symbols . . . . .	ix
Abstract . . . . .	xiii
I. Introduction . . . . .	1-1
1.1 Background . . . . .	1-1
1.2 Purpose . . . . .	1-2
1.3 Scope . . . . .	1-3
1.4 Approach . . . . .	1-5
II. Theory . . . . .	2-1
2.1 Governing Equations . . . . .	2-1
2.2 Thermodynamic Models . . . . .	2-2
2.3 Computational Methodologies . . . . .	2-4
2.3.1 PNS Solvers . . . . .	2-4
2.3.2 Flux-Difference-Splitting . . . . .	2-6
III. Methodology . . . . .	3-1
3.1 FDS Code Description . . . . .	3-1
3.1.1 Governing Flow Equations . . . . .	3-1
3.1.2 Computational Scheme . . . . .	3-1
3.1.3 Boundary Conditions . . . . .	3-3
3.1.4 Decoding the Solution . . . . .	3-4
3.2 PNS Code Description . . . . .	3-5
3.2.1 Governing Flow Equations . . . . .	3-5
3.2.2 Computational Scheme . . . . .	3-6
3.2.3 Boundary Conditions . . . . .	3-8
3.2.4 Turbulence Model . . . . .	3-9
3.2.5 Decoding the Solution . . . . .	3-9
3.3 Oblique Shock Validation. . . . .	3-11
3.3.1 Perfect Gas . . . . .	3-11
3.3.2 Imperfect Gas . . . . .	3-12
3.4 Isolated Hypersonic Nozzle . . . . .	3-13
3.4.1 Freestream Conditions . . . . .	3-13
3.4.2 Internal Flow Conditions . . . . .	3-14
3.4.3 Nozzle Configuration . . . . .	3-16
IV. Findings . . . . .	4-1
4.1 Case Summary . . . . .	4-1
4.2 Grid Refinement . . . . .	4-2
4.2.1 SCHNOZ . . . . .	4-2
4.2.2 FDS Grid Packing . . . . .	4-2
4.3 FDS vs SCHNOZ Frozen Flow Comparisons . . . . .	4-4

4.4	Viscous Effects . . . . .	4-10
4.5	Finite-Rate Chemistry Effects . . . . .	4-11
4.6	FDS Perfect Gas Trends . . . . .	4-13
4.6.1	FDS Perfect Gas vs. Imperfect Gas . . . . .	4-13
4.6.2	FDS Perfect Gas vs. SCHNOZ Finite-Rate Chem . . . . .	4-14
V.	Conclusions/Recommendations . . . . .	5-1
5.1	Conclusions . . . . .	5-1
5.2	Recommendations . . . . .	5-2
	Bibliography . . . . .	BIB-1
	Appendix A: Governing Equations . . . . .	A-1
	Appendix B: Thermodynamic Models . . . . .	B-1
	Appendix C: Flux-Difference-Splitting . . . . .	C-1
	Appendix D: FDS Decoding . . . . .	D-1
	Vita . . . . .	V-1

## List of Figures

Figure	Page
1.1. Typical hypersonic vehicle with airframe-integrated nozzle . . . . .	1-8
1.2. Expanded view of hypersonic nozzle section . . . . .	1-8
2.1. Capabilities of gas dynamic equations . . . . .	2-9
3.1. Stencil for first-order accurate upwind FDS method . . . . .	3-20
3.2. Stencil for first-order accurate upper solid wall boundary point . . . . .	3-20
3.3. Geometry for oblique shock wave study . . . . .	3-21
3.4. Static pressure distribution along the top wall for shock wave reflection study, FDS MacCormack methods . . . . .	3-21
3.5. Static pressure distribution along the top wall for shock wave reflection study, FDS and SCHNOZ frozen flow solutions . . . . .	3-22
3.6. Shock-on-lip SCRAMjet operation . . . . .	3-22
3.7. Parabolic nozzle contour . . . . .	3-23
4.1. Static pressure distribution along nozzle wall for different grid packing, FDS solution, perfect gas, M=15, 38 deg parabolic nozzle . . . . .	4-20
4.2. Static pressure distribution along nozzle wall for different grid packing, FDS solution, frozen flow, M=15, 38 deg parabolic nozzle . . . . .	4-20
4.3. Static pressure contours (atm), FDS frozen flow solution, M=10, 20.6 deg parabolic nozzle contour . . . . .	4-21
4.4. Static pressure contours (atm), SCHNOZ inviscid frozen flow solution, M=10, 20.6 deg parabolic nozzle contour . . . . .	4-21
4.5. Static pressure distribution along nozzle wall, FDS and SCHNOZ inviscid solutions, frozen flow, M=10, 20.6 deg parabolic nozzle contour . . . . .	4-22

4.6.	Static temperature distribution along nozzle wall, FDS and SCHNOZ inviscid solutions, frozen flow, M=10, 20.6 deg parabolic nozzle contour .	4-22
4.7.	Static pressure contours (atm), FDS frozen flow solution, M=15, 20.6 deg parabolic nozzle contour . . . . .	4-23
4.8.	Static pressure contours (atm), SCHNOZ inviscid frozen flow solution, M=15, 20.6 deg parabolic nozzle contour . . . . .	4-23
4.9.	Static pressure distribution along nozzle wall, FDS and SCHNOZ inviscid solutions, frozen flow, M=15, 20.6 deg parabolic nozzle contour . .	4-24
4.10.	Static temperature distribution along nozzle wall, FDS and SCHNOZ inviscid solutions, frozen flow, M=15, 20.6 deg parabolic nozzle contour .	4-24
4.11.	Static pressure contours (atm), FDS frozen flow solution, M=20, 20.6 deg parabolic nozzle contour . . . . .	4-25
4.12.	Static pressure contours (atm), SCHNOZ inviscid frozen flow solution, M=20, 20.6 deg parabolic nozzle contour . . . . .	4-25
4.13.	Static pressure distribution along nozzle wall, FDS and SCHNOZ inviscid solutions, frozen flow, M=20, 20.6 deg parabolic nozzle contour . . .	4-26
4.14.	Static pressure distribution along nozzle wall, FDS and SCHNOZ inviscid solutions, frozen flow, M=10, 38 deg parabolic nozzle contour . . .	4-26
4.15.	Static pressure distribution along nozzle wall, SCHNOZ viscous and inviscid solutions, frozen flow, M=10, 38 deg parabolic nozzle contour . .	4-27
4.16.	Static temperature distribution along nozzle wall, SCHNOZ viscous and inviscid solutions, frozen flow, M=10, 38 deg parabolic nozzle . .	4-27
4.17.	Static pressure distribution along nozzle wall, SCHNOZ frozen and finite-rate chemistry viscous solutions, M=10, 38 deg nozzle . . .	4-28
4.18.	Static temperature distribution along nozzle wall, SCHNOZ frozen and finite-rate chemistry viscous solutions, M=10, 38 deg nozzle . . .	4-28

4.19.	Static pressure distribution along nozzle wall, FDS perfect and imperfect gas solutions, M=10, 38 deg parabolic nozzle contour . . . . .	4-29
4.20.	Static temperature distribution along nozzle wall, FDS perfect and imperfect gas solutions, M=15, 38 deg parabolic nozzle contour . . . . .	4-29
4.21.	Static pressure distribution along nozzle wall, SCHNOZ finite-rate chemistry and FDS perfect gas solutions, M=10, 20.6 deg nozzle . . . . .	4-30
4.22.	Static temperature distribution along nozzle wall, SCHNOZ finite-rate chemistry and FDS perfect gas solutions, M=20, 20.6 deg nozzle . . . . .	4-30
4.23.	Static temperature distribution along nozzle wall, SCHNOZ finite-rate chemistry and FDS perfect gas solutions, M=15, 20.6 deg nozzle . . . . .	4-31
4.24.	Static temperature distribution along nozzle wall, SCHNOZ finite-rate chemistry and FDS perfect gas solutions, M=20, 20.6 deg nozzle . . . . .	4-31

## Appendix

### Figure

	Page
A.1. Compressibility correction parameters for $k\epsilon$ turbulence model . . . . .	A-6
C.1. General property distribution and Riemann description . . . . .	C-13
C.2. Riemann problem for planar supersonic flow and resulting wave pattern . . . . .	C-13
C.3. Flux differences and splitting . . . . .	C-14



## List of Tables

Table	Page
3.1. Freestream conditions for typical hypersonic trajectory . . . . .	3-18
3.2. Nozzle inlet conditions, FDS inputs . . . . .	3-18
3.3. Nozzle inlet conditions, SCHNOZ inputs . . . . .	3-19
3.4. Nozzle geometry specifications . . . . .	3-19
4.1. Comparison of grid packing efficiencies, FDS perfect gas solutions, M=15, 38 deg nozzle . . . . .	4-17
4.2. Computational planes and CPU time (seconds) comparison for the SCHNOZ and FDS inviscid frozen flow solutions . . . . .	4-17
4.3. CPU time and calculated thrust comparisons of SCHNOZ viscous vs. inviscid solutions, frozen flow, 38 deg parabolic nozzle contour . . . . .	4-17
4.4. CPU time and calculated thrust comparisons of SCHNOZ finite-rate chemistry vs. frozen flow solutions, 38 deg parabolic nozzle contour . . . . .	4-18
4.5. Combustion products, H <sub>2</sub> O, mole fraction at nozzle inlet and exit for SCHNOZ finite-rate chemistry solutions . . . . .	4-18
4.6. CPU time and calculated thrust comparisons of FDS imperfect gas vs. perfect gas solutions, 20.6 deg parabolic nozzle contour . . . . .	4-18
4.7. CPU time (seconds) comparison for the FDS perfect gas and SCHNOZ finite-rate chemistry solutions . . . . .	4-19

### *List of Symbols*

$a$	speed of sound
$a_f$	frozen speed of sound
$a_{max}$	local speed of sound at location of maximum value of turbulent kinetic energy
$C_i$	mass fraction of species $i$
$C_1$	constant in turbulence equations
$C_2$	constant in turbulence equations
$C_\mu$	constant in turbulent viscosity relation
$c_p$	specific heat at constant pressure
$c_v$	specific heat at constant volume
$dE$	difference in $E$ flux vector
$dF$	difference in $F$ flux vector
$e$	specific internal energy; alternating difference switch in MacCormack method
$E$	$E$ flux vector
$f$	convected flow property
$F$	$F$ flux vector
$h$	static enthalpy of mixture; nozzle inlet height
$H$	total enthalpy of mixture
$k$	turbulent kinetic energy
$k_{max}$	maximum value of turbulent kinetic energy at each axial location
$K(M_T)$	correction factor in turbulent viscosity relation
$\ell$	turbulent length scale

$m$	mass of mixture
$M$	Mach number
$M_T$	characteristic Mach number of turbulence
$MW$	molecular weight
$P_i$	pressure in region $i$
$p$	static pressure
$p_c$	corrected pressure
$p_t$	total pressure
$q_\infty$	dynamic pressure
$R$	gas constant of mixture
$R_0$	universal gas constant
$s_i$	entropy in region $i$
$T$	static temperature
$T_i$	temperature in region $i$
$T_t$	stagnation temperature
$u$	axial component of velocity
$v$	radial component of velocity
$V$	velocity magnitude
$x$	spatial axial coordinate
$y$	spatial radial coordinate
$y_L$	$y$ location of lower computational boundary
$y_U$	$y$ location of upper computational boundary
$z$	coefficient for linearized approximate Riemann solver

### *Greek Symbols*

$\alpha$	Mach angle
$\alpha_i$	mass fraction of species i
$\gamma$	specific heat ratio
$\gamma_f$	frozen specific heat ratio
$\Delta\xi$	axial step size in transformed coordinate system
$\Delta\eta$	radial step size in transformed coordinate system
$\epsilon$	turbulence energy dissipation rate; shock wave angle
$\eta$	transformed radial coordinate
$\eta_x$	partial derivative of transformed radial coordinate with respect to x
$\eta_y$	partial derivative of transformed radial coordinate with respect to y
$\theta$	flow angle
$\theta_B$	attachment angle for nozzle parabolic wall section
$\mu$	sum of laminar and turbulent viscosity
$\nu$	Prandtl-Meyer angle
$\xi$	transformed axial direction coordinate
$\rho$	density
$\rho e$	total internal energy
$\sigma_i$	flow slope in region i
$\sigma_k$	constant in turbulence equations
$\sigma_\epsilon$	constant in turbulence equations
$\phi_i$	entropy parameter in region i

$\phi_0$	entropy parameter at some reference temperature
$\Psi$	general variable for Riemann problem
$\omega_i$	net rate of production of species i

## Abstract

This study compared the results of two computer programs, a flux-difference-splitting (FDS) Godunov-based scheme and the SCRAMjet Hypersonic Nozzle (SCHNOZ) parabolized Navier-Stokes code using MacCormack's method, applied to a hypersonic nozzle flowfield. Two different nozzle geometries were investigated for three different Mach numbers along a typical hypersonic flight trajectory. A direct comparison between the SCHNOZ and FDS programs was made by numerically solving the steady Euler equations using a frozen flow assumption in the nozzle. Significant areas of interest in comparison of the code results were the accuracy in capturing the flow physics and the required computational time. The frozen flow SCHNOZ program is currently 6 to 10 times more efficient in terms of computational time than the FDS frozen flow program. The SCHNOZ and FDS codes demonstrated comparable accuracy in capturing the flow physics of the nozzle flowfields considered. The implementation of the viscous terms in the SCHNOZ code proved to be ineffectual in modeling the viscous effects in the flowfield. The finite-rate chemistry effects were important for the nozzle inlet conditions considered, as the SCHNOZ finite-rate chemistry model calculated nozzle wall thrusts up to 4% greater than the frozen flow model.

# A Comparison of Computational Fluid Dynamics Computer Programs for Hypersonic Propulsive Nozzle Flowfields

## *I. Introduction*

### *1.1 Background*

The National AeroSpace Plane (NASP) and other trans-atmospheric vehicles have rejuvenated interest in the hypersonic flight regime. The currently proposed propulsive system in the hypersonic regime for NASP-type vehicles is the airframe-integrated Supersonic Combustion RAMjet (SCRAMjet) cycle. Figure 1.1 shows a typical hypersonic vehicle with an airframe-integrated SCRAMjet nozzle. The SCRAMjet nozzle contours are designed to generate sufficient thrust at different flight conditions given a certain vehicle size, weight, and fuel onboard. With the airframe-integrated SCRAMjet, this in turn influences the engine size, vehicle size, and fuel requirements (13:50). Numerous iterations are thus required in the optimization of the vehicle and engine design.

The solution to the hypersonic propulsion design problem will rely heavily upon computational fluid dynamics

(CFD). This reliance on CFD has been driven by the decreasing cost of computers and increasing cost of wind tunnel tests coupled with a limited hypersonic test facility capability (9:657). The hypersonic propulsive environment, with associated high Mach numbers and high temperatures, requires very accurate CFD simulations (7:99). Additionally, the iteration and optimization required in the design process of a hypersonic propulsion system demands an efficient CFD algorithm.

## 1.2 Purpose

Propulsive nozzles for hypersonic vehicles represent an extremely demanding test for CFD codes. The flowfield of a propulsive nozzle, as shown in Figure 1.2, is a complicated structure with expansion waves, shock waves, contact surfaces, and the interaction among all three and surface boundaries such as the nozzle wall or cowl (6:1). Several CFD codes have been developed to resolve the propulsive nozzle flowfield of a hypersonic vehicle. As such, the results of any one CFD code need to be compared with those from other computer codes.

Doty (6) developed a flux-difference splitting (FDS) code using the steady Euler equations and assuming perfect gas to analyze propulsive nozzle flowfields in an effort to optimize nozzle contours. Doty's FDS code was later modified by Schieve (13) to incorporate a calorically



imperfect gas thermodynamic model. A SCRAMjet Hypersonic Nozzle (SCHNOZ) parabolized Navier-Stokes (PNS) computer code was developed by Science Applications International Corporation (SAIC) for the NASP Program (20). The SCHNOZ code includes algorithms for both viscous flow effects and finite-rate chemistry reactions in numerically solving the PNS equations for the flowfield. The purpose of this study was to compare results from the modified FDS code to SCHNOZ code results to determine the most accurate and efficient code in the analysis of a hypersonic propulsive nozzle flowfield.

### 1.3 Scope

This research effort sequentially compared the accuracy and efficiency of Doty's FDS code with the thermodynamic model improvement of Schieve (13) to the SCHNOZ PNS code (20) applied to a hypersonic propulsive nozzle flowfield. The nozzle contour in the study was a two-dimensional, maximum thrust, planar nozzle. Included in the study were nozzle contours determined from Doty's FDS code by Herring to be the optimum nozzle configuration over a typical hypersonic flight trajectory (8) and a more severe expansion nozzle.

The flow in the two-dimensional hypersonic nozzle was assumed to be steady, compressible, and rotational. The fluid in the nozzle was treated as a calorically imperfect,

but thermally perfect, gas where computations of the properties downstream of any discontinuity employed the frozen flow model. The frozen flow model does not account for chemical reactions within the nozzle. This frozen flow assumption was justified by Snelling's finite rate chemistry investigations, which showed that the rapid expansion within the hypersonic nozzle essentially froze the chemical reactions within the nozzle (15:4-4). However, the static temperatures in the flows considered by Snelling were only 2000 K for uniform flow profile studies, and the nozzle inlet profiles considered in this study approached 3000 K. The finite rate chemistry effects become increasingly more important as the temperature increases (1:373-375). Therefore, SCHNOZ code runs were also performed using finite rate chemistry kinetics in the flowfield. Additionally, perfect gas runs were made using the efficient upwind code to demonstrate the ability of the perfect gas model to capture the trends in the hypersonic nozzle flowfield.

The initial internal flowfield of the nozzle was generated from a RAMJET Performance Analysis cycle analysis computer code (11). The internal flowfield cycle analysis solution required the input of the freestream properties at each flight condition. The freestream properties used were determined for a typical hypersonic flight trajectory with a 1000 psf dynamic pressure loading (8).

The analysis of the nozzle CFD code results was made at

three points along the 1000 psf flight trajectory. Flight conditions of Mach 10, Mach 15, and Mach 20 were considered. The desired goal was to determine the most effective and efficient CFD code for use across the entire flight trajectory.

Significant areas of interest in comparison of the CFD code results were the required CPU time, the code accuracy in capturing the flow physics, and the variation of code results for different flight conditions and different nozzle entrance profiles. Additionally, since the SCHNOZ code proved to be very sensitive to grid spacing (13:4-2) the efficiency and accuracy of grid clustering techniques were investigated. The AFIT Computer Lab facilities were used to conduct the computational analysis and comparison with all computations being performed using double precision floating point arithmetic 64-bit SPARCstation 2 machines.

#### 1.4 Approach

Running the SCHNOZ code in the inviscid mode allowed for a comparison between the FDS Godunov-based scheme and MacCormack's scheme in the solution of the steady Euler equations. Prior to the actual nozzle flow analysis, a determination of the trends exhibited by each code was made by comparing the results of the FDS Godunov scheme and the modified MacCormack scheme to a more simple flow situation; the oblique shock wave. The oblique shock wave has an exact

analytical solution which may be compared to the results of the two different schemes. Comparison of the scheme results to the exact solution indicated the ability of each method to capture the true physics of the flow.

Because of the inherent non-linearity of the governing equations and the complicated interactions within the nozzle, no known analytical solution exists for the hypersonic nozzle. It was expected that the full viscous, turbulent, PNS equations modeled in the SCHNOZ program would provide more accurate information on the propulsive nozzle flowfield as it accounted for viscous interactions as well as a turbulence model. For this reason the viscous SCHNOZ code was used as the basis for accuracy comparisons between the codes. Investigations of each flight condition were made operating the SCHNOZ code in both viscous and inviscid modes. The CPU time required for each code solution was measured and used to determine the efficiency of the two codes.

Investigations at each flight trajectory point were made for an isolated nozzle with no external flow interactions. This allowed for a clean comparison between the two codes and the ability of each to resolve the gradients within the nozzle flowfield. For a combined (internal with external) flowfield, both computer programs used non-physical procedures to obtain solutions across the contact surface downstream of the engine cowl. The FDS

program obtained a solution by employing two solid surface boundary conditions and requiring the pressure to match across the surface (6:193). The SCHNOZ program solution is obtained by implementing an embedded grid scheme at an arbitrary distance downstream of the cowl, where the grid spacing is based on the chemical species parameter profile (4:909). For thrust considerations, the isolated nozzle flowfield was shown by Snelling to be equivalent to the combined flowfield for a given cowl geometry (15:4-10). Therefore, the performance of each code on the isolated nozzle was a good indicator of the numerically determined nozzle thrust for each configuration.

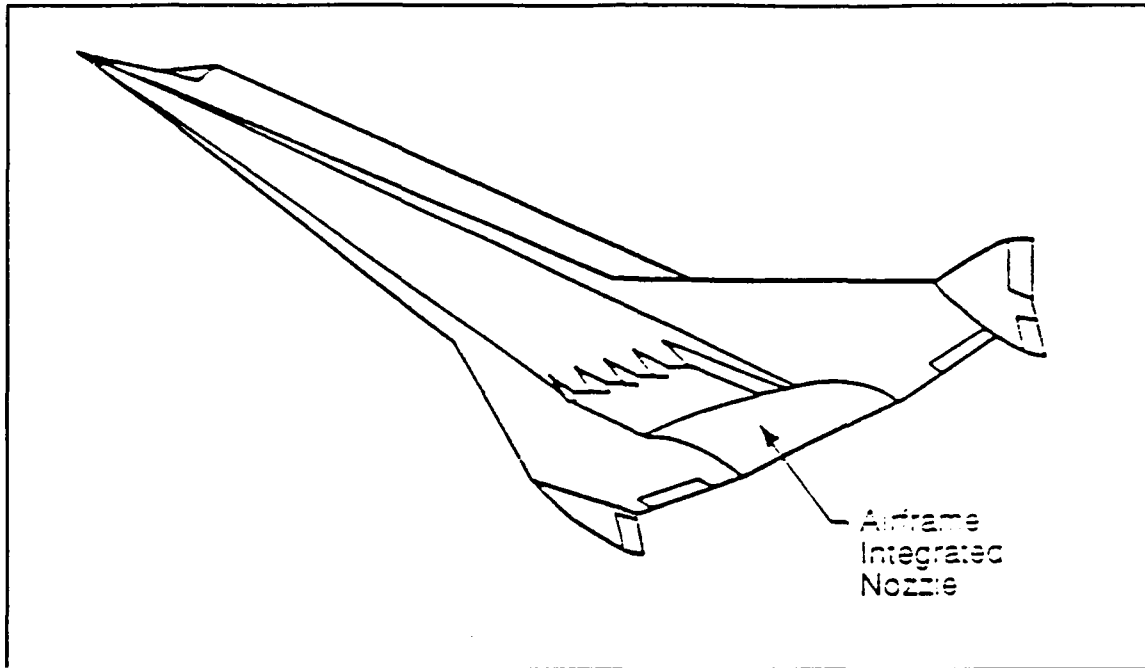


**Figure 1.1.** Typical hypersonic vehicle with airframe-integrated nozzle (6:5)

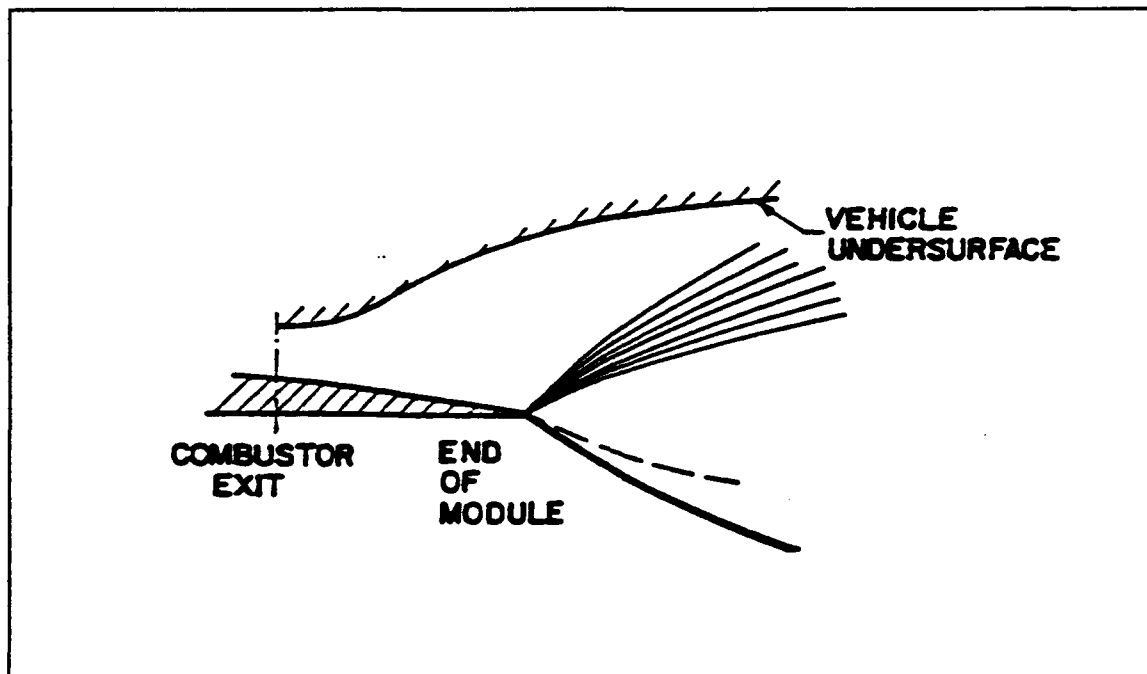


**Figure 1.2.** Expanded view of hypersonic nozzle section (20:2)

## *II. Theory*

### *2.1 Governing Equations*

The governing equations of fluid dynamics and their abilities to solve fluid flow phenomena are summarized in Figure 2.1 (9:659). From the conditions present in the hypersonic propulsive nozzle flowfield discussed previously, the Navier-Stokes equations are necessary to fully solve the flowfield. Full Navier-Stokes equations incorporate the viscous effects of molecular and turbulent dissipation and diffusion (9:659). In the hypersonic environment, radial changes in the viscous terms dominate axial or streamwise changes (1:344) and an accurate solution to the flowfield may be obtained by dropping the streamwise derivatives of viscous terms. The resulting set of equations, with the elimination of all time derivatives, are termed the parabolized Navier-Stokes (PNS) equations. Full discussions of the Navier-Stokes and PNS equations and their numerical implementation are presented in Anderson, Tannehill, and Pletcher (2). The PNS equations employed in the SCHNOZ computer program are presented in Appendix A.

The effects of viscosity and the conduction of heat are not included in the Euler equations. In the hypersonic nozzle design, however, the Euler equations are a valuable tool as the determination of nozzle thrust is dominated by the inviscid pressure effects. With increasing velocities

and the favorable pressure gradient in the expansion of the nozzle, the viscous boundary layer growth is limited, thus having a lessening effect on the overall flow phenomena (2:235-236). The increasing velocity resulting from the nozzle expansion also acts to diminish the free shear layer interactions within the nozzle flow. The Euler equations are capable of capturing the relevant flow phenomena and discontinuities within the hypersonic propulsive nozzle flowfield.

## 2.2 *Thermodynamic Models*

The thermodynamic model employed greatly influences the flow properties downstream of discontinuities within the hypersonic nozzle. The simplest model is the perfect gas. A perfect gas model assumes no intermolecular forces and constant specific heats,  $c_v$  and  $c_p$ , resulting in a constant specific heat ratio,  $\gamma$ . The perfect gas obeys the thermal equation of state (1:381):

$$p = \rho RT \quad (2.1)$$

The perfect gas assumption breaks down when high temperatures are encountered within the nozzle flowfield. In real gases,  $\gamma$  is not a constant, but is dependent on the temperature of the flowfield. A calorically imperfect, but thermally perfect gas model allows for the temperature dependence of the flow by considering the internal structure



of the gas. The calorically imperfect gas assumes that the thermal equation of state, Eq. (2.1), still holds, but accounts for a non-constant  $\gamma$  resulting from increased modes of energy available to the gas molecule; see Appendix B. The calorically imperfect gas assumption is coupled with a frozen flow model which assumes that the molecular composition of the gas remains unchanged throughout the flowfield. The complex chemical mixtures which exit the SCRAMjet combustor can be treated as a mixture of thermally perfect gases. The resulting flowfield properties such as enthalpy and specific internal energy are no longer simple functions of the temperature, but rather are dependent on the chemical composition of the mixture and the functional dependence on temperature of each species contained within the mixture.

In real gases, the flow properties are a function of not only temperature, but pressure and time as well (7:99). The nonequilibrium chemically reacting gas thermodynamic model accounts for the chemical reactions within the flowfield. The nonequilibrium chemically reacting gas allows for a changing molecular composition based on finite-rate chemistry kinetics. As discussed in Appendix B, a finite-rate chemistry kinetics package is coupled with the governing equations of the flow and determines the chemical composition and resulting flow properties based on the reaction rates for a given set of species and chemical

reactions. The nonequilibrium chemically reacting gas is a more complete model of the flow physics, but also more complex to incorporate in a solution procedure.

## 2.3 Computational Methodologies

### 2.3.1 PNS Solvers

PNS equation solvers are in widespread use in the analysis of the hypersonic flow regime (1:360). The popularity of the PNS solvers is attributable to the efficiency in predicting the hypersonic flowfield with a great savings in computational storage and time in comparison to a full Navier-Stokes solution (2:420). Unfortunately, to obtain an accurate solution requires a greater amount of user interaction and adjustment of various input parameters (1:348-349). The parabolization of the Navier-Stokes equations allows for an explicit downstream marching finite-difference solution technique.

A Scramjet Hypersonic Nozzle (SCHNOZ) parabolized Navier-Stokes computer code was developed by Science Applications International Corporation (SAIC) for the NASP Program (20). The SCHNOZ Code is the nozzle analysis component of an integrated system of two-dimensional PNS codes for analyzing SCRAMjet propulsive nozzle flowfields (20:7). SCHNOZ unifies previous work in rocket propulsive nozzles and the extension of the PNS equations to supersonic mixing problems and finite rate chemistry (20:4).

SCHNOZ uses the MacCormack method to explicitly solve the PNS equations in conservative form (20:4). The MacCormack predictor-corrector method determines the downstream flux values based on the average of a predicted and then corrected downstream flux derivative (2:482-485). To dampen oscillations inherent in the MacCormack scheme in the presence of strong discontinuities, a self-adjusting hybrid scheme developed by Harten and Zwas is added to modify the MacCormack scheme (20:24).

To account for chemically reacting flow in the nozzle, SCHNOZ employs a finite-rate chemical kinetics package developed by AeroChem (20:20-21). Additionally, the SCHNOZ code contains two high Reynolds Number turbulence models to handle the turbulent nature of the nozzle inlet flow exiting from the combustor (20:9).

The PNS equations are hyperbolic in nature, thus requiring supersonic flow for a valid, well-posed problem (2:24). The addition of the viscosity effects causes a small subsonic region at the viscous boundary layer interaction region (1:204). This subsonic region is mathematically elliptic and the downstream marching technique of MacCormack's method is invalid in this region (1:204). The SCHNOZ code removes this subsonic portion of the boundary layer and enforces a slip boundary condition, resolving the flow at the wall based on a viscous-characteristic formulation related to the pressure and flow

angle at the boundary (20:13-14).

Snelling (15) used the SCHNOZ code to examine the effects of non-uniform nozzle entrance profiles on pitching moments. Snelling investigated several inlet nozzle profiles on an isolated and combined internal flow/external flow nozzle. In that study Snelling showed that the chemical kinetics considerations are unnecessary extra computational time, producing nearly identical results to the frozen flow model (15:5-1). Snelling also found that the addition of the external flow interaction had little effect on the overall nozzle thrust (15:4-11).

### *2.3.2 Flux-Difference-Splitting*

The solution of discontinuities in the nozzle flowfield is representative of the Riemann problem. The Riemann problem describes the collapse of flowfield discontinuities to a local point of consideration (6:2,11-17). These discontinuities give rise to fluxes that are not present in the initial value line. The differences between these fluxes and the initial values of the flowfield are split along the characteristic waves developed by the local collapse of the discontinuity (6:2). This technique is known as the flux-difference-splitting (FDS) method. Full details on the FDS method and the solution of the Riemann problem using a Godunov scheme are given in reference (6) and summarized in Appendix C.

The MacCormack scheme applied to the Riemann problem and FDS was analyzed by Steger and Warming (17) for the solution of time dependent flow in a shock tube. Similarly, Roe (12) used a density ratio across the discontinuities to influence the fluxes considered in the Riemann problem to solve the unsteady Euler equations. Grossman (7) modified the upwind FDS schemes developed by Van Leer, Steger and Warming, and Roe to incorporate a real-gas equivalent ratio of specific heats based on equilibrium chemical reactions in high temperature flow. Sod (17) provides an excellent survey of the different solution schemes applied to the Riemann problem for the unsteady Euler equations. Chakravarthy (3) provides a comprehensive comparison of upwind schemes based on the FDS method for unsteady flowfields that are integrated in time to the steady state.

However, the determination of the nozzle thrust for a propulsive vehicle requires only the steady-state solution of the flowfield (6:2). The use of the time-dependent schemes mentioned above are not very efficient when advanced to the steady state. It is more efficient to directly solve the steady form of the Euler equations. Pandolfi (10), using a Godunov scheme, applied the unsteady FDS method to the solution of steady supersonic flows.

Doty (6) employed an upwind FDS method based on the Godunov scheme to solve the Riemann problem. Doty's work showed that the shock capturing ability of the first-order

accurate upwind FDS method provided solutions comparable in accuracy to a higher-order MacCormack method, but with a tremendous savings in computational time (6:75).

Herring (8) demonstrated the utility of the upwind FDS code developed by Doty in an optimization study of nozzle contours for a typical hypersonic flight trajectory assuming a calorically perfect gas in the nozzle. Schieve (13) modified Doty's code to use a calorically imperfect (thermally perfect) gas model and showed a difference in nozzle thrust of over 16% compared to the perfect gas model.

	C O N T I N U U M	C O M P R E S S I B L E	N O N L I N E A R	R O T A T I O N A L	V I S C O U S	R A R E F I E D
Boltzmann	X	X	X	X	X	X
Navier-Stokes	X	X	X	X	X	
Euler	X	X	X	X		
Full Potential	X	X	X			
Prandtl-Glauert	X	X				
Laplace	X					

**Figure 2.1.** Capabilites of gas dynamics equations (9:659).

### III. Methodology

#### 3.1 FDS Code Description

##### 3.1.1 Governing Flow Equations

The FDS code of Doty (6) solves the following divergence vector form of the Euler equations:

$$\frac{\partial \mathbf{E}}{\partial x} + \frac{\partial \mathbf{F}}{\partial y} = 0 \quad (3.1)$$

where the  $\mathbf{E}$  and  $\mathbf{F}$  flux vectors are given by

$$\mathbf{E} = \begin{bmatrix} \rho u \\ \rho u^2 + p \\ \rho uv \\ u(\rho e + p) \end{bmatrix}, \quad \mathbf{F} = \begin{bmatrix} \rho v \\ \rho vu \\ \rho v^2 + p \\ v(\rho e + p) \end{bmatrix} \quad (3.2)$$

The vector components represent the continuity, x momentum, y momentum, and energy equations, respectively. The governing vector equation is independent of the thermodynamic models considered in the FDS study and is applicable to both perfect and calorically imperfect gas flows.

##### 3.1.2 Computational Scheme

The governing equations are transformed from physical space to the computational space assuming the following transformation:

$$\begin{aligned} \xi &= x \\ \eta &= \eta(x, y) \end{aligned} \quad (3.3)$$

The governing equation, Eq. (3.1), is transformed in



computational space as:

$$\frac{\partial(\mathbf{E})}{\partial \xi} = \eta_x \frac{\partial(\mathbf{E})}{\partial \eta} - \eta_y \frac{\partial(\mathbf{F})}{\partial \eta} \quad (3.4)$$

Detailed information on the coordinate transformation is presented in reference (6:142-143).

The transformed governing equations are numerically solved in computational space using a first-order accurate FDS method. The FDS method developed by Doty is based on the Godunov initial-value Riemann problem. The Riemann problem and the first-order accurate upwind FDS method are described in detail in Appendix C. Essentially, the Riemann problem is used to resolve discontinuities in the flowfield into numerical fluxes. The resulting Riemann fluxes are propagated along characteristics determined by the local wave angle (6:9).

To axially march the solution from station  $i$  to  $i+1$  in Figure 3.1, the Godunov-based FDS method resolves the Riemann fluxes and then computes flux differences based on the initial value flux at axial location  $i$ . These flux differences are then split based on their direction of propagation such that the resulting flux difference is sent in the physically correct direction.

The stencil for the first-order accurate FDS method is presented in Figure 3.1. Note in Figure 3.1 that the Riemann fluxes are resolved at the grid midpoints,  $j+1/2$  and  $j-1/2$ . The first-order accurate upwind FDS scheme uses

positively biased information from node  $j-1/2$  and negatively biased information from node  $j+1/2$  to advance the solution from node  $(i,j)$  to  $(i+1,j)$  (13:17). The first-order accurate FDS finite-difference approximation to the transformed governing equation, Eq. (3.4), for an interior grid point is given by (6:15):

$$E_j^{i+1} = E_j^i - \Delta\xi\eta_x\{dE_{j+1/2}^* + dE_{j-1/2}^*\} - \Delta\xi\eta_y\{dF_{j-1/2}^* + dF_{j+1/2}^*\} \quad (3.5)$$

It should be noted that the FDS finite-difference equation, Eq. (3.5), is independent of the Riemann problem solution procedure and the thermodynamic model.

### 3.1.3 Boundary Conditions

The interior grid point solution, Eq. (3.5), is not valid at boundaries, as it would require information outside the physical domain. As shown in Figure 3.2, there can be no negatively biased information from a node  $j+1/2$  influencing the solution because of the solid wall upper boundary. The solution procedure for the FDS solid wall boundary is a two step wave-corrector requiring the velocity vector to be tangent to the solid boundary (6:190). A contact surface boundary point, such as would exist for the interaction between the internal nozzle flow and external freestream, essentially uses a coupled solid wall boundary condition. An iterative solution procedure is necessary to

match the pressure and flow angle for the contact contact surface (6:193). Details on the first-order accurate FDS boundary point calculations are presented in reference (6:189-194).

#### *3.1.4 Decoding the Solution*

Once the solution has been marched downstream to the next axial location,  $i+1$ , the primitive flow variables must be extracted from the newly determined **E** and **F** flux vectors so that the Riemann problem may be solved. This allows the solution to continually march downstream in the axial direction. The extraction of the primitive variables from the **E** and **F** flux vector solutions is referred to as decoding the solution. The decode procedure differs depending on the thermodynamic model employed in the calculation. The perfect gas decode procedure is a closed form solution procedure based on the flux vector components and the conservation of stagnation enthalpy. The calorically imperfect gas decode procedure is an iterative process based on temperature that must incorporate the imperfect gas model into the conservation of stagnation enthalpy. Differences in the decode procedure for the two different thermodynamic models are presented in Appendix D.

### 3.2 PNS Code Description

#### 3.2.1 Governing Flow Equations

The SCHNOZ code solves the following conservative form of the PNS equations:

$$\frac{\partial \mathbf{E}}{\partial x} + \frac{\partial \mathbf{F}}{\partial y} + \mathbf{G} = \frac{\partial}{\partial y} \left( \frac{\bar{\mu}}{\sigma_r} \frac{\partial \mathbf{f}}{\partial y} \right) \quad (3.6)$$

where the flux vectors are

$$\mathbf{E} = \begin{bmatrix} \rho u \\ p + \rho u^2 \\ \rho uv \\ \rho uH \\ \rho u\alpha_i \end{bmatrix} \quad \mathbf{F} = \begin{bmatrix} \rho v \\ \rho uv \\ p + \rho v^2 \\ \rho vH \\ \rho v\alpha_i \end{bmatrix} \quad \mathbf{G} = \begin{bmatrix} 0 \\ 0 \\ 0 \\ -\frac{\partial}{\partial y} \left[ \frac{\bar{Pr}-1}{\bar{Pr}} \bar{\mu} \frac{\partial}{\partial y} \left( \frac{u^2}{2} \right) \right] \\ -\dot{\omega}_i \end{bmatrix} \quad \mathbf{f} = \begin{bmatrix} 0 \\ u \\ v \\ H \\ \alpha_i \end{bmatrix} \quad (3.7)$$

The vector components of Eq. (3.7) represent the continuity, x momentum, y momentum, energy equation, and species continuity equations, respectively. The governing vector equation is not independent of the thermodynamic models considered in the SCHNOZ study. The species continuity equation is necessary for finite-rate chemistry considerations. For perfect or calorically imperfect gas frozen flow studies, the species continuity equation is not implemented. Additionally, for inviscid flow calculations of a perfect or calorically imperfect frozen gas, the viscous terms are dropped and the PNS equations reduce to the Euler equations.

The governing equations are transformed from physical space into rectangular computational coordinates,  $\xi$  and  $\eta$ ,

through the following transformation:

$$\begin{aligned}\xi &= x \\ \eta &= [y - y_L(x)] / [y_U(x) - y_L(x)]\end{aligned}\quad (3.8)$$

where  $y_U$  and  $y_L$  represent the upper and lower physical boundaries respectively (20:21).

### 3.2.2 Computational Scheme

The transformed governing equations are numerically solved in the computational domain using the explicit two-step MacCormack algorithm. The MacCormack algorithm spatially marches the solution from an initial data line,  $i$ , downstream to a new axial location,  $i+1$ . The first step of the MacCormack method calculates a downstream predicted value of the  $\mathbf{E}$  flux vector, denoted by  $\mathbf{E}^*$ , using the upstream values of the  $\mathbf{E}$ ,  $\mathbf{F}$ ,  $\mathbf{G}$ , and  $\mathbf{f}$  flux quantities (1:197). The second step of the MacCormack method then uses the predicted flux values,  $\mathbf{E}^*$ ,  $\mathbf{F}^*$ ,  $\mathbf{G}^*$ , and  $\mathbf{f}^*$ , to correct the downstream flux quantities (1:198). The SCHNOZ program employs the following second-order-accurate, central-difference predictor and corrector formulas at an interior grid point,  $(i,j)$ , to advance the solution from an axial location  $i$  to  $i+1$  (15:3-2):

*Predictor Step:*

$$\begin{aligned} \mathbf{E}_j^* = \mathbf{E}_j^i - \frac{\Delta \xi}{\Delta \eta} \{ (1-e) \mathbf{F}_{j+1} - (1-2e) \mathbf{F}_j - e \mathbf{F}_{j-1} - \mathbf{G}_j \Delta \xi \} \\ + \frac{\Delta \xi b^2}{\Delta \eta^2} \{ \mathbf{A}^+ \mathbf{f}_{j+1} - \mathbf{f}_j - \mathbf{A}^- (\mathbf{f}_j - \mathbf{f}_{j-1}) \} \end{aligned} \quad (3.9)$$

*Corrector Step:*

$$\begin{aligned} \mathbf{E}_j^{i+1} = \frac{1}{2} [\mathbf{E}_j^i + \mathbf{E}_j^* - \frac{\Delta \xi}{\Delta \eta} \{ e^* \mathbf{F}_{j+1} + (1-2e) \mathbf{F}_j + (e-1) \mathbf{F}_{j-1} \} \\ - \mathbf{G}_j^* \Delta \xi + \frac{\Delta \xi b^2}{\Delta \eta^2} \{ \mathbf{A}^{*+} (\mathbf{f}_{j+1}^* - \mathbf{f}_j^*) - \mathbf{A}^{*-} (\mathbf{f}_j^* - \mathbf{f}_{j-1}^*) \}] \end{aligned} \quad (3.10)$$

where

$$\mathbf{A}^\pm = \frac{1}{2} \left[ \left( \frac{\bar{u}}{\sigma_f} \right)_j + \left( \frac{\bar{u}}{\sigma_f} \right)_{j\pm 1} \right] \quad (3.11)$$

and for  $\mathbf{f} = u, v, H$ , and  $\alpha_i$

$$\sigma_u = \sigma_v = 1 \quad \sigma_H = \sigma_{\alpha_i} = \bar{P}\bar{R} \quad (3.12)$$

The  $e$  term in Eqs. (3.9) and (3.10) is an alternating switch ( $e = 0$  at even steps;  $e = 1$  at odd steps) used to provide nonbiased convective differencing (20:23).

The basic MacCormack scheme has been shown to overshoot and undershoot flow properties downstream of flowfield discontinuities (20:23, 2:146-147, and 6:24,31). The oscillation of flow properties about a discontinuity is

remedied using the self adjusting hybrid scheme of Harten and Zwas (20:23). The Harten and Zwas hybrid scheme adds a dissipative term to the conservative flow equations of the MacCormack scheme based on the pressure at surrounding grid points (20:23). From a corrected value of the flux variable  $E$ , the addition of a viscous term to the MacCormack solution is implemented to yield the self-adjusting hybrid value,  $\bar{E}$ , using the following finite-difference representation (20:23):

$$\bar{E}_j^{i+1} = E_j^{i+1} + \frac{1}{8}(\theta_{j+1/2}^i \Delta E_{j+1/2}^i - \theta_{j-1/2}^i \Delta E_{j-1/2}^i) \quad (3.13)$$

The  $\theta$  terms are dimensionless parameters varying from 0 to 1, based upon the pressure at the surrounding grid points to provide appropriate levels of damping to the solution (20:23).

### 3.2.3 Boundary Conditions

The SCHNOZ program uses the forward or backward MacCormack algorithm with an Abbett correction procedure to handle solid wall boundary conditions (20:31). The Abbett correction procedure enforces the surface flow tangency condition at the wall. A corrected pressure,  $p_c$ , is determined at the wall by considering the wall to be composed of a series of infinitesimal simple expansion or compression waves for a small change in surface slope,  $\Delta\theta$ .

The corrected pressure is found from (15:3-3):

$$p_c = p - \frac{\gamma p M^2}{\sqrt{M^2 - 1}} \Delta \theta \quad (3.14)$$

where  $p$  and  $M$  in Eq. (3.14) are the values at the boundary determined using the MacCormack algorithm. The corrected pressure is then used to correct the density and the axial and radial velocity components are determined from the actual slope of the wall. More details are given by Wolf et al. (20:33-34).

#### 3.2.4 Turbulence Model

The SCHNOZ program contains two variants of turbulence modelling equations, the  $k\epsilon$  and  $kW$  high Reynolds number versions. The turbulence model used in this study is the common two-equation  $k\epsilon$  eddy viscosity model which models the turbulent kinetic energy,  $k$ , and energy dissipation,  $\epsilon$ , detailed in Appendix A. The  $k\epsilon$  model was chosen because the  $kW$  model has had difficulties in applications to wall bounded shear flows such as those in a nozzle (5:507). Additionally, the implementation of the  $k\epsilon$  model in the SCHNOZ code is determined by a correlation to experimental jet mixing results (5:507).

#### 3.2.5 Decoding the Solution

Unlike the FDS algorithm, the primitive variables are not a computational necessity at every axial location in the



downstream marching of the SCHNOZ program. Advances from one axial position to the next using the MacCormack method are based only on the flux vectors. The extraction of primitive variables from the flux vectors (decoding the solution) is necessary however, to determine the artificial damping of the Harten and Zwas hybrid scheme, which is dependent on the pressure at surrounding nodes. The decode procedure is also used to obtain the primitive variables at desired axial locations. The SCHNOZ program uses a different decode procedure based on the thermodynamic model employed. For the perfect gas model, a simple closed form decode procedure is employed based on the flux vector components. For the thermally perfect frozen flow and the finite-rate chemistry thermodynamic models, a different real gas decode procedure is employed depending on whether the flow is supersonic,  $M > 1$ , or hypersonic,  $M > 5$ .

For supersonic flows, an iterative procedure is employed that uses an assumed pressure value,  $p'$ , to calculate the flow velocity. The total enthalpy and velocity are then used to calculate the enthalpy,  $h'$ :

$$h' = H' - \frac{1}{2} (u^2 + v^2) \quad (3.15)$$

Calculating the species mole fractions,  $\alpha_i$ , and the temperature,  $T'$ , from the assumed value of  $p'$ , the enthalpy is also calculated using the species formulation:

$$h^* = \sum \alpha_i h_i(T') \quad (3.16)$$

The assumed pressure,  $p'$ , is iterated upon until the calculated enthalpy values of  $h'$  and  $h^*$  match to a prescribed tolerance (20:30).

The iteration procedure described above breaks down for the expanding hypersonic nozzle flow where the kinetic flow energy,  $H$ , is orders of magnitude greater than the thermal contribution,  $h$  (20:31). SCHNOZ uses an iterative decode procedure for hypersonic flow conditions that is based on a linear relation between the axial velocity component and temperature (20:75).

### 3.3 Oblique Shock Validation

#### 3.3.1 Perfect Gas

A demanding test of the two numerical methods is the oblique shock reflection which contains large discontinuities in the flowfield properties downstream of the shock wave. The geometry of this flow situation is shown in Figure 3.3. Doty, using a perfect gas assumption, compared the second-order centered MacCormack algorithm to the first-order upwind Godunov based FDS algorithm using a 10 degree ramp shock wave geometry with a Mach 2.2 incoming flow (6:31). Figure 3.4 shows the static pressure distribution along the top wall obtained with the two different methods compared to the exact analytical solution.

Doty found that the second-order accurate MacCormack method did no better than the first-order accurate Godunov based FDS method in capturing the location of the shock (6:24). Additionally, the MacCormack method overshot the exact solution before reaching the correct pressure rise, while the FDS method monotonically approached the correct pressure (6:24).

The MacCormack method implemented by Doty did not incorporate the Harten and Zwas hybrid scheme to remedy the oscillations downstream of the discontinuity. Sod showed that the addition of the artificial viscosity of the Harten and Zwas hybrid scheme smoothed out the MacCormack method in the area of discontinuities while retaining second-order accuracy in the smooth portions of the flow (16:24). The oblique shock reflection geometry verified the ability of the first-order Godunov-based FDS scheme to capture the physics of a strong flowfield discontinuity. This provided the initiative to implement the FDS method in the analysis of the hypersonic propulsive nozzle flowfield.

### *3.3.2 Imperfect Gas*

The MacCormack method as implemented in the SCHNOZ computer program incorporates the Harten and Zwas hybrid damping scheme. A comparison between the imperfect gas FDS method and the SCHNOZ frozen flow inviscid solution was made on the 10 deg oblique shock geometry using the same Mach 2.2

inlet conditions as Doty used to compare the perfect gas FDS and MacCormack methods. To allow for a comparison to an exact analytical solution, the imperfect gas was assumed to be Argon-free air in the standard mole fraction ratios of 0.79  $N_2$  and 0.21  $O_2$ . The analytical solution was determined using an imperfect gas oblique shock wave solver provided by Schieve (13:91-95).

Figure 3.5 shows the static pressure distribution along the upper wall obtained with the two different methods compared to the exact analytical solution. The FDS imperfect gas method and the SCHNOZ frozen flow solution equally capture the the location of the shock and the static pressure downstream of the flowfield discontinuity. Additionally, with the Harten and Zwas damping scheme the second-order MacCormack method no longer overshoots the exact solution and monotonically approaches the correct pressure as does the first-order accurate Godunov-based scheme.

### 3.4 *Isolated Hypersonic Nozzle*

#### 3.4.1 *Freestream Conditions*

The freestream conditions used in this study are those for a typical hypersonic flight trajectory with a constant dynamic pressure,  $q_\infty$ , of 1000 psf. Freestream properties were determined at Mach numbers of 10, 15, and 20 along this trajectory. Assuming the freestream conditions obey perfect

gas relations, the freestream static pressure is found from the definition of Mach number and the constant dynamic pressure:

$$p = \frac{2q_{\infty}}{\gamma M_{\infty}^2} \quad (3.17)$$

The flight trajectory altitude,  $z$ , is interpolated from the 1962 Standard Atmosphere Table assuming  $p = p(z)$ . The remaining freestream properties are calculated using the 1962 atmosphere. The freestream conditions used in this study are tabulated in Table 3.1.

#### 3.4.2 Internal Flow Conditions

The initial conditions for the isolated nozzle investigations were generated from a RAMJET Performance Analysis (RJPA) cycle analysis code (10). The RJPA code simulated a Supersonic Combustion RAMJET (SCRAMjet) engine operating at each flight condition along the hypersonic trajectory. The SCRAMjet was assumed to operate in a shock-on-lip condition with the maximum capture of airflow without spillage (19:3). The shock-on-lip condition is illustrated in Figure 3.6 where the bow shock wave emanating from the forebody compression rests on the engine inlet.

The capture area of the SCRAMjet inlet is driven by airframe geometries and the resulting shock structure upstream of the inlet (19:3). For this study, an effective

bow shock of 8 degrees was used to simulate a 2 degree angle of attack and 6 degree forebody compression on the underside of the hypersonic vehicle. The SCRAMjet inlet and capture areas are then determined at each flight condition for the 8 degree compression.

The RJPA program was run simulating an air-breathing, hydrogen-fueled, SCRAMjet engine cycle using a 14 species gas mixture with some frozen  $H_2$  carried through a constant area combustion process to simulate combustion inefficiency. The RJPA program calculates the following flow properties at several stations in the SCRAMjet engine:  $T$ ,  $p$ ,  $\rho$ ,  $V$ ,  $\gamma_f$ ,  $a_f$ ,  $M_f$ ; the  $f$  subscript denotes frozen flow values. The RJPA program also calculates the molecular weight (MW) of the mixture and the mole and mass fractions of each species in the mixture at specified engine stations. The combustor exit properties calculated by the RJPA program provide the initial conditions for the internal nozzle studies.

The FDS code requires an input value of the gas constant,  $R$ , which was determined using the universal gas constant,  $R_0$ , and the MW.

$$R = \frac{R_0}{MW} \quad (3.18)$$

This value of  $R$  is used as the initial condition for both perfect and imperfect gas frozen flow analyses and finite-rate chemistry flows. The MW and  $R$  values remain constant for the perfect gas and frozen flow models as the molecular

composition remains fixed. The finite-rate chemistry flow allows for chemical reactions and hence a change in MW and the gas constant,  $R$ . The ratio of specific heats,  $\gamma_f$ , determined from the RJPA analysis is used as an initial condition of the internal nozzle for all flows considered. The differences between the perfect gas, calorically imperfect frozen gas, and finite-rate chemistry assumptions do not effect the initial conditions, but become apparent in the downstream expansion of the flow in the nozzle; see Appendix B. The nozzle inlet parameters for the FDS code are tabulated in Table 3.2 for each flight condition on the hypersonic flight trajectory.

The internal nozzle inlet conditions for the SCHNOZ code are presented in Table 3.3 for the same flight trajectory points. The SCHNOZ code using the perfect gas assumption requires not only  $R$ , but the MW of the mixture. In essence, the mixture of gases in the nozzle is treated as a perfect gas with a MW equivalent to the MW of the 14 species gas mixture calculated by the RJPA program.

#### 3.4.3 Nozzle Configuration

As shown in Figure 3.7 (6:46), the hypersonic nozzle wall consists of two sections. The first section, A-B, is a circular arc of radius  $r$ , followed by a parabolic section, B-C, with an attachment angle,  $\theta_B$ . For the isolated nozzles used in this study the lower boundary, or cowl wall, E-F, is

a straight wall section.

The parabolic nozzle contour used for this study is the optimal nozzle contour for the entire hypersonic flight trajectory determined from the FDS perfect gas analysis performed by Herring (9). This analysis arrived at a parabolic nozzle contour with an attachment angle of 20.6 degrees. Additionally, a much higher circular arc attachment angle,  $\theta_B = 38$  deg, is considered to examine the ability of each code to compute a flowfield with a shock wave (6:49). The nozzle geometries,  $x/h$  and  $y/h$ , are characteristic of geometries considered for hypersonic propulsive nozzles (6:3). The nozzle geometry parameters for the two nozzles are listed in Table 3.4.

The nozzle geometry utilized in the SCHNOZ code is flipped upside relative to the FDS nozzle geometry, however the pertinent specifications remain the same. The  $x$  and  $y$  coordinates for each wall location are determined from the FDS analysis parabolic contour generator and are used to generate the nozzle wall input to the SCHNOZ code. The SCHNOZ wall contour is then calculated from the  $x$  and  $y$  coordinates using a cubic spline interpolation routine. The cubic spline interpolation can lead to small differences between the two codes in the  $x$  and  $y$  coordinates and nozzle wall angles at each wall location.



**Table 3.1.** Freestream conditions for typical hypersonic flight trajectory

Free stream parameter	$M_\infty = 10$	$M_\infty = 15$	$M_\infty = 20$
altitude, (km)	33.791	39.581	43.934
static pressure, $p$ (N/m <sup>2</sup> )	684.0	304.0	171.0
static temperature, $T$ (K)	233.2	249.2	261.2
density, $\rho$ (kg/m <sup>3</sup> )	0.01022	0.00425	0.00228
velocity, $V$ (m/s)	3061.4	4746.9	6479.9
specific heat ratio, $\gamma$	1.4	1.4	1.4
gas constant, $R$ (J/kg/K)	287.06	287.06	287.06

**Table 3.2.** Nozzle inlet conditions, FDS inputs

Internal Flow Parameter	$M_\infty = 10$	$M_\infty = 15$	$M_\infty = 20$
Mach number	2.0582	3.4736	4.6791
static pressure, $p$ (N/m <sup>2</sup> )	373,566	199,752	133,921
static temperature, $T$ (K)	2986.1	3062.9	3176.3
specific heat ratio, $\gamma$	1.25219	1.25966	1.27186
gas constant, $R$ (J/kg/K)	355.9	365.7	381.2
Species Mass Fraction for Frozen Flow			
$N_2$	0.726652	0.724947	0.722695
$O_2$	0.023287	0.029532	0.035884
Ar	0.012877	0.012877	0.012877
H	0.000701	0.001445	0.002840
OH	0.022336	0.030736	0.040664
$H_2$	0.005085	0.006512	0.008066
NO	0.015743	0.018386	0.024192
$H_2O$	0.188322	0.164449	0.132859
O	0.004994	0.010106	0.019907

**Table 3.3.** Nozzle inlet conditions, SCHNOZ inputs

Internal Flow Parameter	$M_\infty = 10$	$M_\infty = 15$	$M_\infty = 20$
Mach number	2.0582	3.4736	4.6791
static pressure, $p$ (atm)	3.6867	1.9714	1.3217
static temperature, $T$ (K)	2986.1	3062.9	3176.3
axial velocity, $u$ (ft/s)	7789.1	13,537	19,052
radial velocity, $v$ (ft/s)	0.0	0.0	0.0
Gas Mixture Parameters for Perfect Gas Flow			
molecular weight, MW	23.3635	22.7327	21.8060
specific heat ratio, $\gamma$	1.25219	1.25966	1.27186
Species Mole Fraction for Frozen and Finite-Rate Flow			
H	0.016243	0.032577	0.061418
H <sub>2</sub>	0.058920	0.073441	0.087213
H <sub>2</sub> O	0.244184	0.207456	0.160752
N <sub>2</sub>	0.613426	0.595442	0.569337
O	0.007291	0.014355	0.027121
OH	0.030678	0.041072	0.052118
O <sub>2</sub>	0.017000	0.014681	0.024445
NO	0.012253	0.020976	0.017572

**Table 3.4.** Nozzle geometry specifications

Circular arc attachment angle, $\theta_B$ (deg)	20.6	38.0
Inlet height, $h$ (inches)	1.0	1.0
Nozzle circular arc radius, $r$ (inches)	1.0	1.0
Nozzle wall end, $x/h$	100.0	100.0
Nozzle wall end, $y/h$	$\pm 25.0$	$\pm 25.0$
Nozzle wall end angle, $\theta_E$ (deg)	$\pm 10.01$	$\pm 8.04$

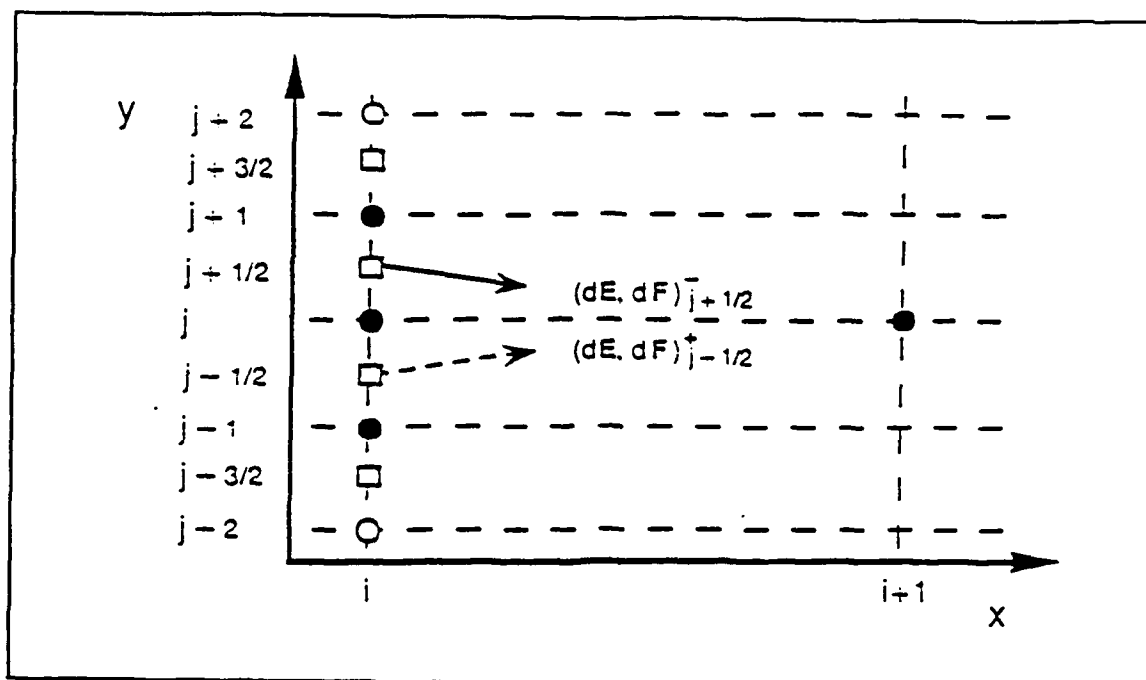


**Figure 3.1.** Stencil for first-order accurate upwind FDS method (6:195).

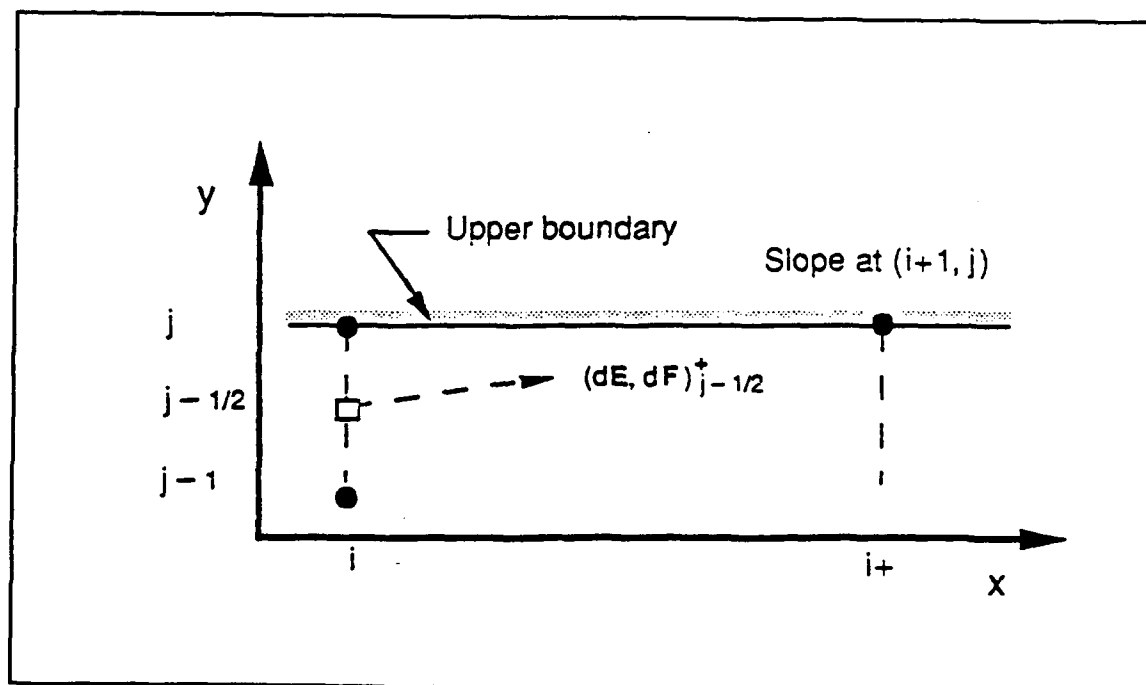


**Figure 3.2.** Stencil for first-order accurate upper solid wall boundary point (6:195).

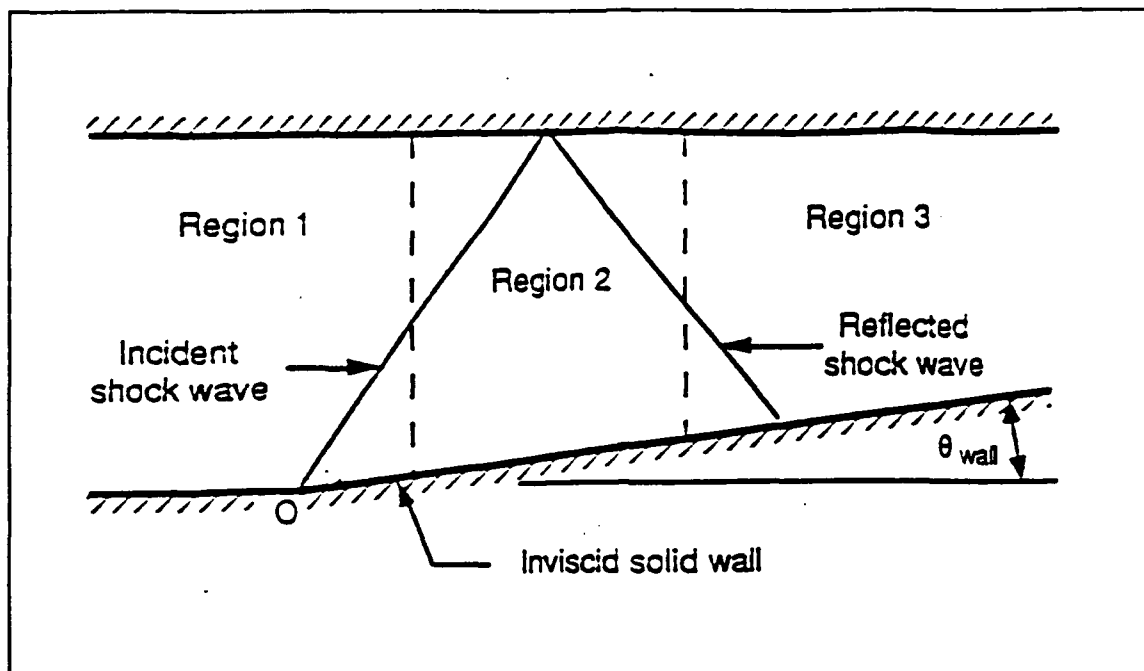


**Figure 3.3.** Geometry for oblique shock wave study (6:30).

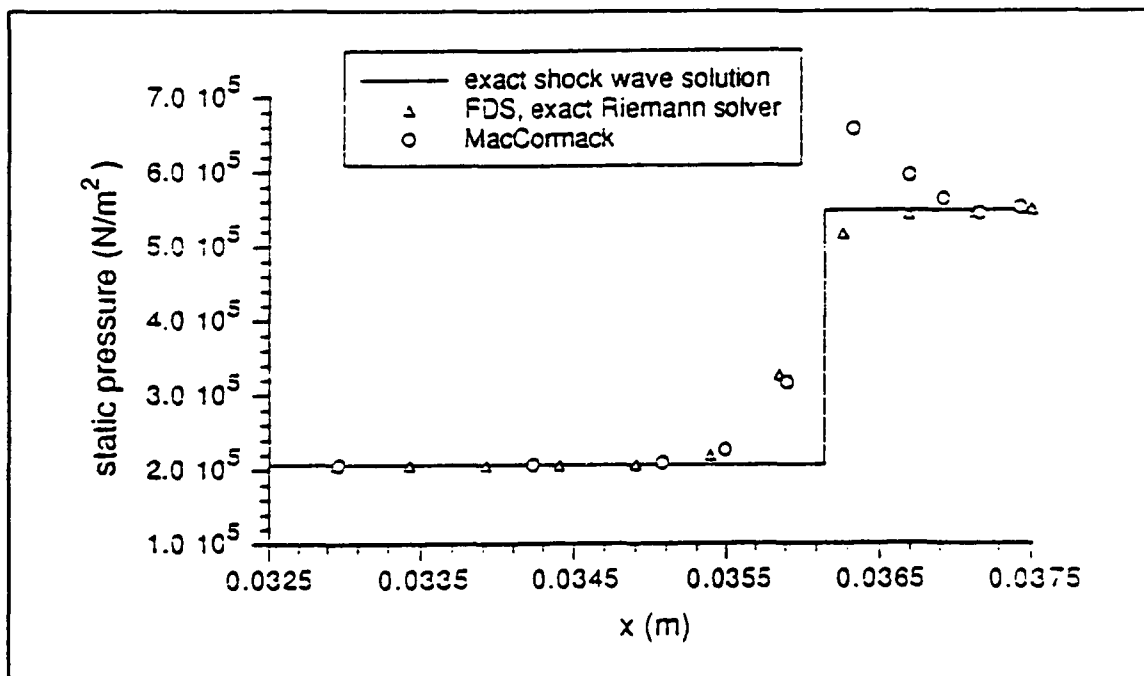


**Figure 3.4.** Static pressure distribution along the top wall for shock wave reflection study, FDS and MacCormack methods (6:31).

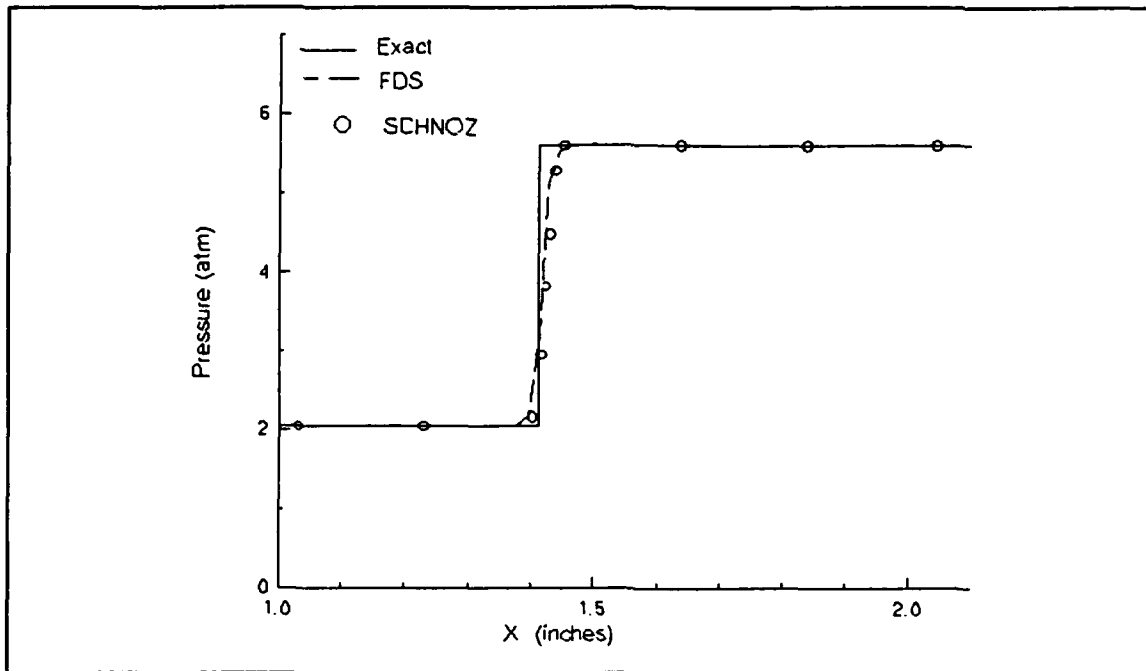


**Figure 3.5.** Static pressure distribution along the top wall for shock wave reflection study, FDS and SCHNOZ frozen flow solutions.

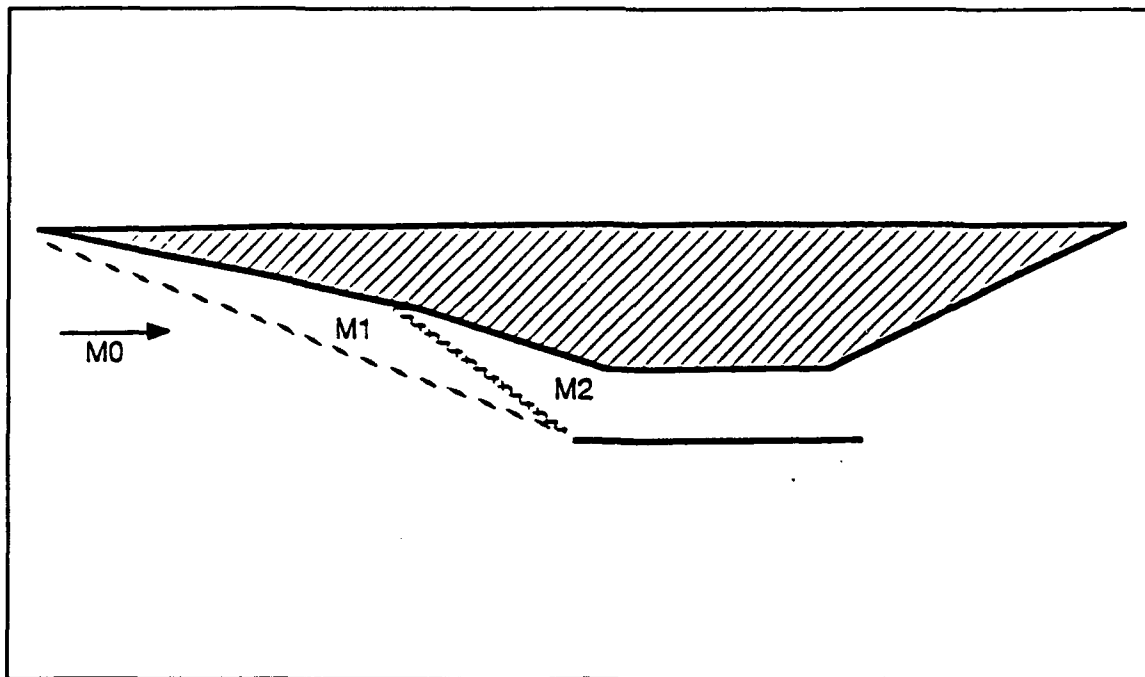


**Figure 3.6.** Shock-on-lip SCRAMjet operation (19:27).

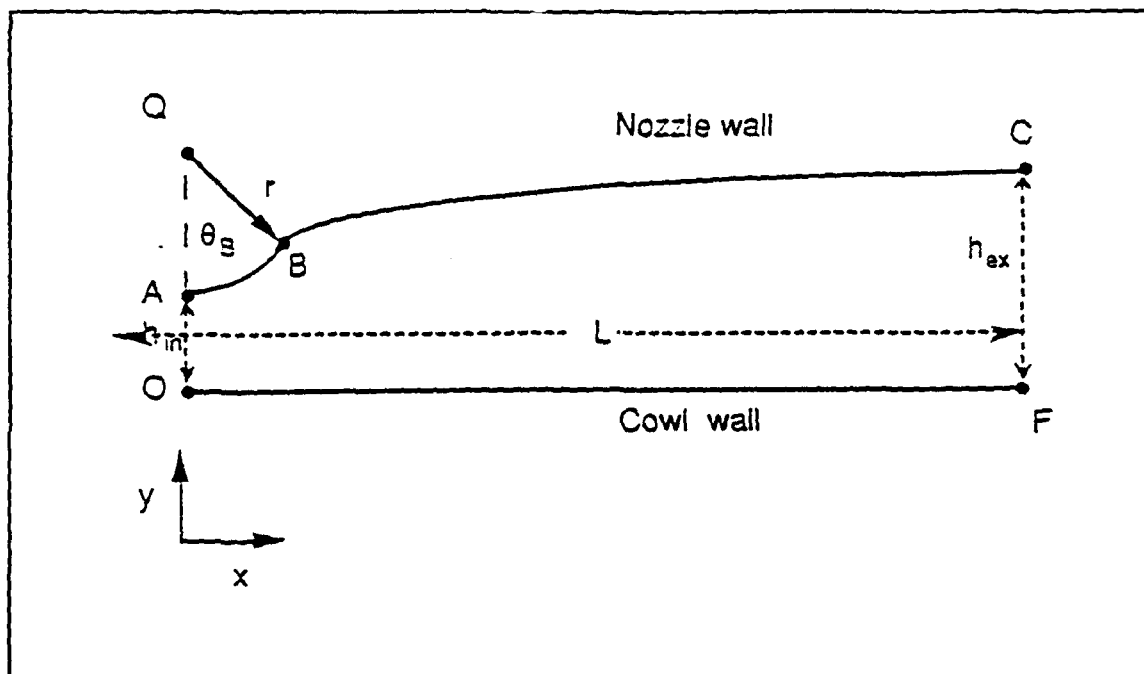


**Figure 3.7.** Parabolic nozzle contour (6:57).

## IV. Findings

### 4.1 Case Summary

Comparisons of the FDS and SCHNOZ codes were made using several different combinations of nozzle geometries, flight conditions, and thermodynamic models. Direct comparisons of the FDS and SCHNOZ codes were made using an inviscid frozen flow assumption for two different parabolic nozzle contours, 20.6 deg and 38 deg, at three different flight conditions, Mach = 10, 15, and 20, along a typical hypersonic trajectory. An investigation of the SCHNOZ implementation of viscosity terms was made by comparing inviscid and viscous code results for the same nozzle geometries and flight conditions. Comparisons of the frozen flow and finite-rate chemistry models in the SCHNOZ code were also made for the same combinations of nozzle geometries and flight conditions. The nozzle geometries and flight conditions were also used to compare perfect gas and frozen flow FDS results. The comparisons are presented in plots of static pressure and temperature distributions along the nozzle wall, pressure contour plots, and tables of CPU time.

## 4.2 Grid Refinement

### 4.2.1 SCHNOZ

The SCHNOZ code proved to be very sensitive to grid fineness in resolving the changing flowfield properties along the nozzle wall (15:4-2). With a coarse grid, 51 points in the radial direction, the MacCormack algorithm was unable to keep track of the rapidly changing flow properties along the nozzle wall (15:4-2). A finer grid, 101 radial points, was required to fully resolve the complex nozzle flowfield. The SCHNOZ program utilizes equally spaced radial grid intervals,  $\Delta y$ . The allowable axial marching step,  $\Delta x$ , is limited by a combination of the Courant-Friedrichs-Lewy (CFL) hyperbolic stability criterion and the parabolic diffusion criterion for viscous flows (20:32).

### 4.2.2 FDS Grid Packing

Grid packing techniques are available in the FDS code that can cluster gridlines toward the nozzle wall by reducing the radial interval,  $\Delta y$ . The grid clustering is dependent on the packing factor, which gives the fractional position of a packed grid point (6:147). Figure 4.1 plots the static pressure distribution along the nozzle wall for the FDS perfect gas solution using a grid packing value of 1.10 and also for no grid packing. Figure 4.2 plots the static pressure distribution along the nozzle wall for the frozen flow FDS solution and the two different grid packing



factors. Figures 4.1 and 4.2 show that grid clustering is necessary to resolve the flowfield properties along the nozzle wall without oscillatory behavior using the FDS code. Computations were made with 101 radial grid points for both the perfect gas and frozen flow thermodynamic models on the 38 deg parabolic nozzle contour at the Mach 15 flight condition. The packing factors were used to cluster the gridlines near the lower and upper walls to capture the rapidly changing properties along these boundaries.

Table 4.1 presents a comparison of the number of computational planes and CPU seconds required as a result of different grid packing factors. The CPU seconds are for computations using double precision floating point arithmetic 64-bit SPARCstation 2 machines. Because of the decrease in the radial interval, the grid packing causes a corresponding decrease in the axial step size,  $\Delta x$ , to meet the CFL stability criterion. No significant change in the wall property distributions were seen with the increased grid packing for a packing factor of 1.05, but a significant increase in CPU time was required. Attempts to use 51 radial grid points and grid packing factors were unsuccessful as the FDS code failed to compute a non-oscillatory solution for these grids. The grid packing factor of 1.10 provided a non-oscillatory solution with the least inefficiency in terms of CPU time and was used throughout the remainder of the study.

#### 4.3 FDS vs SCHNOZ Frozen Flow Comparisons

Figures 4.3 through 4.14 present a comparison between the FDS and SCHNOZ inviscid, frozen flow solutions to the steady Euler equations. The comparison between the two solutions is presented in contour plots of static pressure throughout the nozzle, and property distributions along the nozzle wall. The contour plots and property distribution plots illustrate the particular characteristics of the propulsive nozzle flowfield and demonstrate the ability of each computer program to capture the flow physics in the hypersonic nozzle.

The static pressure contour plot for the FDS imperfect gas solution with the 20.6 deg nozzle attachment angle is illustrated in Figure 4.3 for the Mach 10 flight condition. The static pressure contour plot for the SCHNOZ inviscid, frozen flow solution for the same flight condition and nozzle geometry is illustrated in Figure 4.4. Figures 4.3 and 4.4 show a good agreement between the two solution methods for the general characterization of the nozzle flowfield. Immediately downstream of the combustor exit the flow undergoes a rapid expansion about the nozzle attachment radius (item 1). The initial expansion is reflected off the lower boundary and continually influences the flow downstream in the nozzle. As the rate of change of the slope of the nozzle wall decreases, a recompression is generated in the flowfield (item 2). This recompression is

reflected off the lower boundary and impinges on the nozzle wall (item 3). The reflected compression is then carried throughout the nozzle (item 4).

The calculated pressure distribution along the nozzle wall for both the FDS and SCHNOZ frozen flow solutions is presented in Figure 4.5 for the Mach 10 flight condition and the 20.6 deg nozzle attachment angle. The rapidly expanding flow around the nozzle attachment radius causes a sharp initial decrease in pressure. The pressure rise downstream at an  $X/h$  of between 5 and 10 results from the recompression of the flow due to the change in wall curvature after the parabolic wall attachment point. The drop in pressure downstream of the recompression occurs due to the expanding nozzle geometry and the reflection of the initial expansion. The increase in pressure further downstream at  $X/h=50$  is a result of the reflected recompression wave as illustrated in Figures 4.3 and 4.4. The expansion and pressure drop gradually proceeds downstream of this slight recompression.

The temperature distribution along the nozzle wall for the FDS and SCHNOZ frozen flow solutions for the Mach 10 flight condition and 20.6 deg nozzle geometry is illustrated in Figure 4.6. The temperature distribution along the nozzle wall essentially follows that of the pressure distribution. The temperature decreases in regions of expansion, and increases across the recompressions.

Figures 4.5 and 4.6 show that there is a slight

difference in the pressure and temperature distributions along the nozzle wall for the two different code solutions. The recompression pressure peak is slightly larger in magnitude and located slightly further downstream for the SCHNOZ solutions. The pressure and temperature rise at the reflected recompression,  $X/h=50$ , are more pronounced for the SCHNOZ solution than the FDS solution. The difference between the two results may be attributable to the additional axial steps required in the FDS solution. Table 4.2 presents a comparison of the number of computational planes and CPU seconds required for the two solutions. For the Mach 10 flight condition and the 20.6 deg nozzle attachment angle, the FDS solution requires almost 3 times as many computational steps (1461) as the SCHNOZ solution (562). The increased number of computational steps results from the grid packing utilized in the FDS solution and the CFL stability criterion requirements. The increased number of computational steps adds artificial damping to the flowfield solution, thus diminishing the pressure and temperature rise at the compression peaks. Despite these slight differences in the pressure and temperature peaks, there is a good overall agreement between the two code results.

The static pressure contour plot for the FDS imperfect gas solution with the 20.6 deg nozzle attachment angle is illustrated in Figure 4.7 for the Mach 15 flight condition.

Figure 4.8 presents the same information for the SCHNOZ frozen flow solution. Figures 4.7 and 4.8 show a good agreement between the two solution methods. The rapid expansion about the nozzle attachment circular radius occurs immediately downstream of the nozzle inlet (item 1). The change in nozzle curvature causes a recompression (item 2) which reflects off of the lower boundary (item 3) and is carried downstream (item 4). The bending of the recompression wave between items 2 and 3 is due to the interactions between the recompression wave and the initial nozzle expansion reflecting off the lower solid boundary. Unlike Figures 4.3 and 4.4, the recompression in Figures 4.7 and 4.8 does not reflect off the nozzle wall. Due to the increased velocity in the nozzle for the Mach 15 flight condition, the recompression is carried downstream without reflecting on the nozzle wall.

Figures 4.9 and 4.10 show the pressure and temperature distributions, respectively, along the nozzle wall for the FDS and SCHNOZ frozen flow solutions for the 20.6 deg nozzle attachment angle at the Mach 15 flight condition. Figure 4.9 shows that the initial expansion is much more rapid for the Mach 15 flight condition than the Mach 10 flight condition shown in Figure 4.5. This occurs because of the increased velocity of the Mach 15 combustor exit results. The FDS frozen flow solution calculates a lower pressure and temperature rise at the recompression. Again, the FDS

solution is artificially dampened by the additional computational steps. Table 4.2 shows that the FDS solution, with the grid packing, uses over twice as many computational steps as the SCHNOZ solution. Aside from the slight differences at the recompression, the FDS and SCHNOZ property distributions at the nozzle wall are nearly identical for the Mach 15 flight condition and 20.6 deg nozzle geometry.

The static pressure contour plot for the FDS imperfect gas solution with the 20.6 deg nozzle attachment angle is illustrated in Figure 4.11 for the Mach 20 flight condition. The static pressure contour plot for the SCHNOZ, inviscid frozen flow solution for the same flight condition and nozzle geometry is illustrated in Figure 4.12. Figures 4.11 and 4.12 show a good agreement between the two solution methods for the general characterization of the nozzle flowfield. The initial nozzle expansion (item 1) is more severe for the Mach 20 flight condition because of the greater nozzle inlet velocity. The recompression due the change in nozzle curvature (item 2) is quickly carried downstream and coalesces into a shock wave within the nozzle (item 3).

The calculated pressure distribution along the nozzle wall for both the FDS and SCHNOZ frozen flow solutions is presented in Figure 4.13 for the Mach 20 flight condition and the 20.6 deg nozzle attachment angle. Figure 4.13 shows

that the expansion is more rapid for the Mach 20 flight condition than for the Mach 15 flight condition (Figure 4.9). The rapid expansion is enhanced by the increased nozzle inlet velocity for the Mach 20 flight condition. The FDS frozen flow solution calculates a slightly lower pressure rise from the recompression than the SCHNOZ solution due to the artificial damping induced by the FDS grid packing.

The calculated pressure distribution along the nozzle wall for both the FDS and SCHNOZ frozen flow solutions is presented in Figure 4.14 for the Mach 10 flight condition and the 38 deg nozzle attachment angle. Comparing Figure 4.14 to Figure 4.5, the pressure distribution plot for the 20.6 deg nozzle geometry, shows that the 38 deg attachment angle causes a more rapid and severe expansion about the nozzle attachment radius. The initial expansion about the 38 deg attachment radius achieves a pressure of approximately one-third of that for the expansion about the 20.6 deg attachment radius. The increased attachment angle allows for a greater nozzle expansion. Figure 4.14 shows nearly a 10% difference in the FDS and SCHNOZ calculated magnitudes of the recompression pressure rise. Table 4.2 shows that the FDS solution, with grid packing, uses over twice as many computational steps as the SCHNOZ solution. The artificial damping from the additional computational steps is more pronounced for the 38 deg attachment angle

nozzle, as compared to the 20.6 deg nozzle geometry, because the recompression wave is stronger due to a greater change in nozzle curvature downstream of the nozzle attachment point.

Figures 4.3 through 4.14 show a generally good agreement between the FDS and SCHNOZ frozen flow solutions in capturing the physics of the hypersonic propulsive nozzle flowfield. The maximum difference in the pressure distribution along the nozzle wall is approximately 10%, occurring at the Mach 10 flight condition for the 38 deg nozzle attachment angle. The greatest difference between the two solutions, however, is in the required computational time. Table 4.2 shows that the FDS imperfect gas method requires CPU times between 6.4 and 9.9 times greater than the SCHNOZ frozen flow solution.

#### *4.4 Viscous Effects*

The implementation of the viscosity terms in the SCHNOZ code proved to be ineffective in truly capturing any viscous effects. Figures 4.15 and 4.16 show the static pressure and temperature distributions, respectively, along the nozzle wall for the viscous and inviscid calculations of the 38 deg parabolic nozzle contour at the Mach 10 flight condition. There is no discernable difference between the property distributions for the inviscid and viscous flow calculations. This same pattern was seen in all other nozzle geometries and flight conditions.



Table 4.3 shows the difference in the CPU time and the calculated nozzle thrust for the inviscid and viscous SCHNOZ results. The differences in calculated nozzle wall thrusts between the viscous and inviscid SCHNOZ solutions are less than 0.1% for all flight conditions and geometries. Compared to the inviscid solution, the viscous solution required a factorial increase of up to 1.25 times the computational time. Essentially, the implementation of the viscous terms in the SCHNOZ code provided no additional information to the flowfield solution at the expense of additional CPU time. The ineffectiveness of the SCHNOZ code to model the viscous effects is attributable to the slip flow boundary condition employed to remove the subsonic portion of the boundary layer.

#### *4.5 Finite-Rate Chemistry Effects*

Frozen and finite-rate thermodynamic models were considered at each flight condition to study the effect of chemistry on the calculated nozzle flowfield for both the 20.6 deg and 38 nozzle contours. Figures 4.17 and 4.18 show the pressure and temperature distributions, respectively, along the nozzle wall for the 38 deg parabolic nozzle contour for the Mach 10 flight condition. Figure 4.17 shows that there is a slight difference in the pressure distribution, as the frozen flow calculates a smaller pressure rise downstream of the initial expansion compared

to the finite-rate chemistry results. The difference in the pressure distribution results in a difference in the calculated nozzle thrust. Table 4.4 shows the increase in CPU time and the percent change in the calculated thrust for the finite-rate chemistry runs compared to the frozen flow results. The calculated nozzle wall thrust is greater for the finite-rate chemistry SCHNOZ solutions than the frozen flow solution. The increase in the calculated nozzle wall thrust is due to the increase in the pressure distribution along the nozzle wall for the finite-rate chemistry solutions. The percent change in nozzle thrust is a maximum of 4% at the Mach 20 flight condition and is independent of the two nozzle geometries considered. The solution of the viscous PNS equations including finite-rate chemistry effects, required CPU run times approximately 2.5 times greater than the inviscid SCHNOZ frozen flow computations.

The difference in the temperature distribution is more pronounced than the difference in pressure distribution between the two thermodynamic models. Figure 4.18 shows the increased temperature distribution along the nozzle wall of the finite-rate chemistry solution compared to the frozen flow solution for the Mach 10 flight condition and the 38 degree parabolic nozzle contour. The finite-rate chemistry model allows for dissociation and chemical reactions throughout the nozzle flowfield. As shown in Table 4.5, the mole fraction of the combustion products,  $H_2O$ , increases

from the nozzle inlet to exit. The increase in  $H_2O$  indicates that the combustion process is continuing as the flow expands through the nozzle. The combustion process releases energy into the flowfield. This additional energy results in a higher temperature for the finite-rate chemistry solution than the frozen flow solution.

#### *4.6 FDS Perfect Gas Trends*

##### *4.6.1 FDS Perfect Gas vs. Imperfect Gas*

Figures 4.19 and 4.20 present the static pressure and temperature distributions, respectively, along the nozzle wall for the FDS imperfect and perfect gas solutions to the 38 deg parabolic nozzle contour at the Mach 10 flight condition. The perfect gas calculates both a higher pressure and temperature distribution along the nozzle wall. The calculation of the pressure using the linearized-approximate FDS method was virtually the same for both gas models considered, see Appendix C. However, there is a greater difference in the calculation of temperature because of the variation of the ratio of specific heats,  $\gamma$ , allowed in the imperfect gas model. The variation of  $\gamma$  with temperature for the imperfect gas and the increased modes of molecular energy allow the imperfect gas to more equally distribute the energy conversion across the recompression wave. The perfect gas absorbs a greater percentage of the energy change into the translational mode of energy, thus

resulting in an increase in temperature.

The addition of the imperfect gas model to the FDS algorithm causes a significant increase in computational time. Table 4.6 shows the increase in CPU time and the percent change in the calculated thrust for the imperfect gas FDS results compared to the perfect gas FDS results. CPU run times were up to 20 times greater for the imperfect gas model than the perfect gas FDS. The added run time is caused by the additional iterations required in the solution of the Riemann problem downstream of a discontinuity and the decoding of the Riemann flux vector components.

#### *4.6.2 FDS Perfect Gas vs. SCHNOZ Finite-Rate Chem*

It is interesting to note that the FDS perfect gas assumption results more closely follow the finite-rate chemistry results of the SCHNOZ code than do frozen flow results. Figures 4.17 and 4.18 show that the SCHNOZ finite-rate chemistry model solution calculates slightly higher pressure and temperature distributions than the SCHNOZ frozen flow solution. The higher pressure and temperature distributions occur because of the added energy to the flow from the combustion process continuing throughout the nozzle. Similarly, Figures 4.19 and 4.20 show that the perfect gas FDS solution calculates higher pressure and temperature distributions than the imperfect gas FDS. The higher pressure and temperature distributions occur because

of the increase in the energy absorbed by the translational mode of energy downstream of the flowfield discontinuities.

An adhoc comparison of the FDS perfect gas solutions and SCHNOZ finite-rate chemistry model solutions is presented in Figures 4.21 through 4.24. Figure 4.21 illustrates the pressure distribution along the nozzle wall for the SCHNOZ finite-rate chemistry model solution and the FDS perfect gas solution for the 20.6 deg nozzle geometry at the Mach 10 flight condition. Figure 4.21 shows a good agreement between the two calculated pressure distributions along the nozzle wall. Figure 4.22 shows the temperature distribution along the nozzle wall for the same flight condition and geometry. Except for the differences at the recompression peaks, the FDS perfect gas temperature distribution is offset by a constant amount from the temperature distribution determined from the SCHNOZ finite-rate chemistry model.

Figure 4.23 shows a relatively constant offset in the FDS perfect gas temperature distribution and the SCHNOZ finite-rate chemistry results for the Mach 15 flight condition and the 20.6 deg nozzle geometry. This same constant offset is evident in the two calculated temperature distributions for the 20.6 deg nozzle geometry at the Mach 20 flight condition illustrated in Figure 24. The artificial damping because of the grid packing used in the FDS perfect gas solution contributes to difference in the

temperature distributions at the recompression peaks for Figures 4.22 through 4.24.

Table 4.7 presents the CPU time comparison for the FDS perfect gas and SCHNOZ finite-rate chemistry solutions. The perfect gas FDS algorithm runs 6 to 8 times faster than the SCHNOZ finite-rate chemistry runs. The constant offset in the temperature distributions in Figures 4.22-4.24 indicates that a slight change in the  $\gamma$  value used for the FDS perfect gas solution could yield a more accurate temperature distribution. The choice of a perfect gas  $\gamma$  that is representative of the actual flow physics would allow the perfect gas FDS solution to provide valuable information on the flow phenomena trends exhibited in the nozzle with a tremendous savings in computational time.

**Table 4.1.** Comparison of grid packing efficiencies, FDS perfect gas solutions, M=15, 38 deg nozzle.

Packing fraction	Axial Steps	CPU time (sec)
None	387	34.1
1.10	806	74.2
1.05	1291	119.6

**Table 4.2.** Computational planes and CPU time (seconds) comparison for the SCHNOZ and FDS inviscid frozen flow solutions.

Flight condition	Axial Steps FDS	Axial Steps SCHNOZ	CPU Time FDS	CPU Time SCHNOZ
M=10, 20.6 nozzle	1461	562	2214.8	224.8
M=15, 20.6 nozzle	934	443	1767.1	187.2
M=20, 20.6 nozzle	691	403	1111.6	173.2
M=10, 38 nozzle	1258	561	2105.2	224.3
M=15, 38 nozzle	788	480	1467.1	200.4

**Table 4.3.** CPU time and calculated thrust comparisons of SCHNOZ viscous vs. inviscid solutions, frozen flow, 38 deg parabolic nozzle contour.

Flight condition	factoral increase in CPU time vs. inviscid solution	percent change in nozzle thrust vs. inviscid solution
Mach 10	1.14	0.00
Mach 15	1.18	0.08
Mach 20	1.25	0.02

**Table 4.4.** CPU time and calculated thrust comparisons of SCHNOZ finite-rate chemistry vs. frozen solutions, 38 deg parabolic nozzle contour.

Flight condition	factoral increase in CPU time vs. frozen flow	percent increase in nozzle thrust vs. frozen flow
Mach 10	2.65	3.89
Mach 15	2.47	3.33
Mach 20	2.49	4.06

**Table 4.5.** Combustion products, H<sub>2</sub>O, mole fraction at nozzle inlet and exit for SCHNOZ finite-rate chemistry solutions.

Flight condition	inlet H <sub>2</sub> O mole fractions	exit H <sub>2</sub> O mole fractions
M=10, 20.6 nozzle	0.2442	0.2808
M=15, 20.6 nozzle	0.2075	0.2436
M=20, 20.6 nozzle	0.1608	0.1982

**Table 4.6.** CPU time and calculated thrust comparisons of FDS imperfect gas vs. perfect gas solutions, 20.6 deg parabolic nozzle contour.

Flight condition	factoral increase in CPU time vs. perfect gas	percent change in nozzle thrust vs. perfect gas
Mach 10	15.79	-6.70
Mach 15	19.94	-1.40
Mach 20	17.53	-1.40



**Table 4.7.** CPU time (seconds) comparison for the FDS perfect gas and SCHNOZ finite-rate chemistry solutions.

Flight condition	FDS perfect gas	SCHNOZ finite rate chem	factoral increase in time vs. FDS
M=10, 20.6 nozzle	140.2	702.4	5.01
M=15, 20.6 nozzle	88.6	553.2	6.24
M=20, 20.6 nozzle	63.4	496.8	7.84
M=10, 38 nozzle	121.6	679.0	5.58
M=15, 38 nozzle	75.1	583.7	7.77

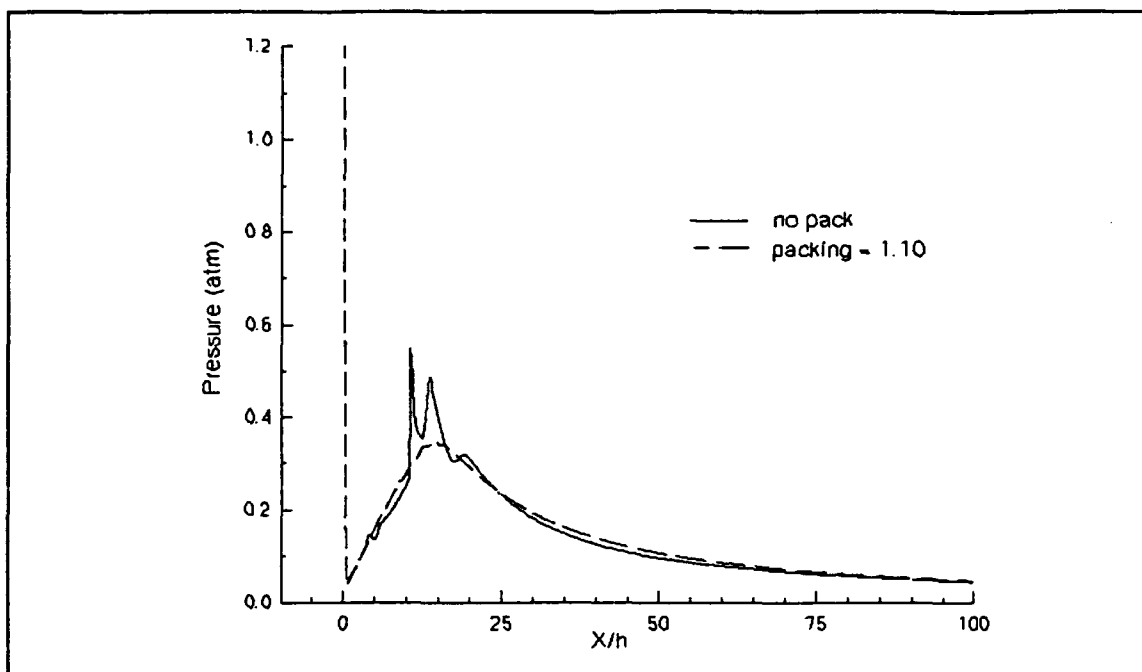


**Figure 4.1.** Static pressure distribution along nozzle wall for different grid packing, FDS solution,  $M=15$ , perfect gas, 38 deg parabolic nozzle.

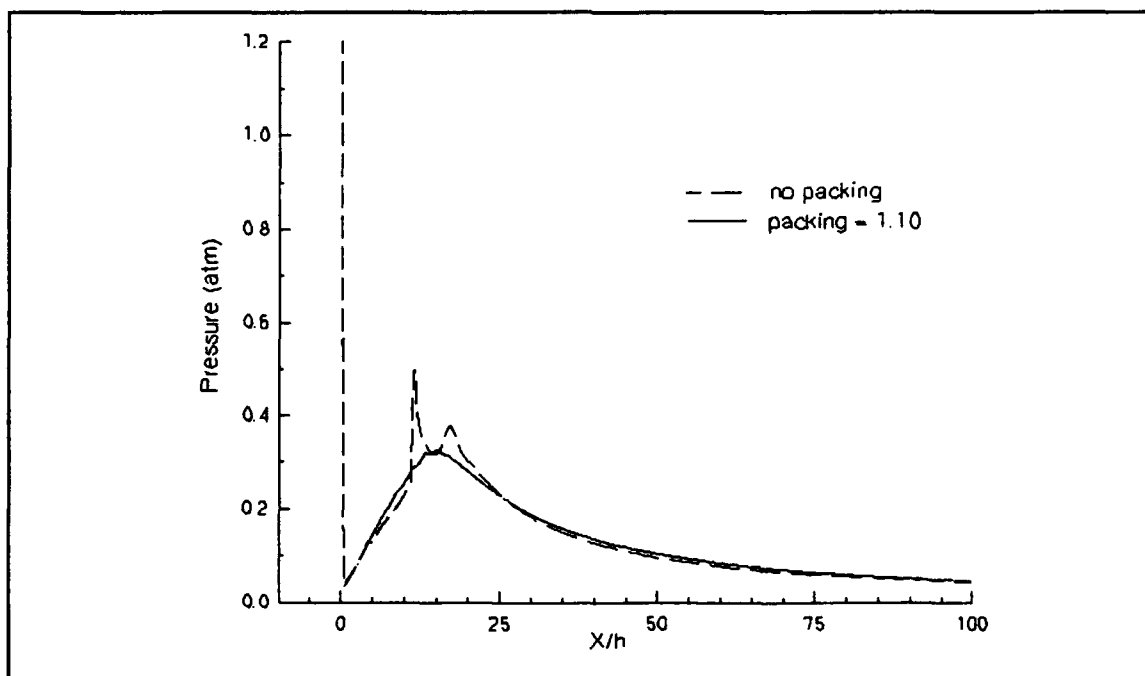


**Figure 4.2.** Static pressure distribution along nozzle wall for different grid packing, FDS solution,  $M=15$ , frozen flow, 38 deg parabolic nozzle.

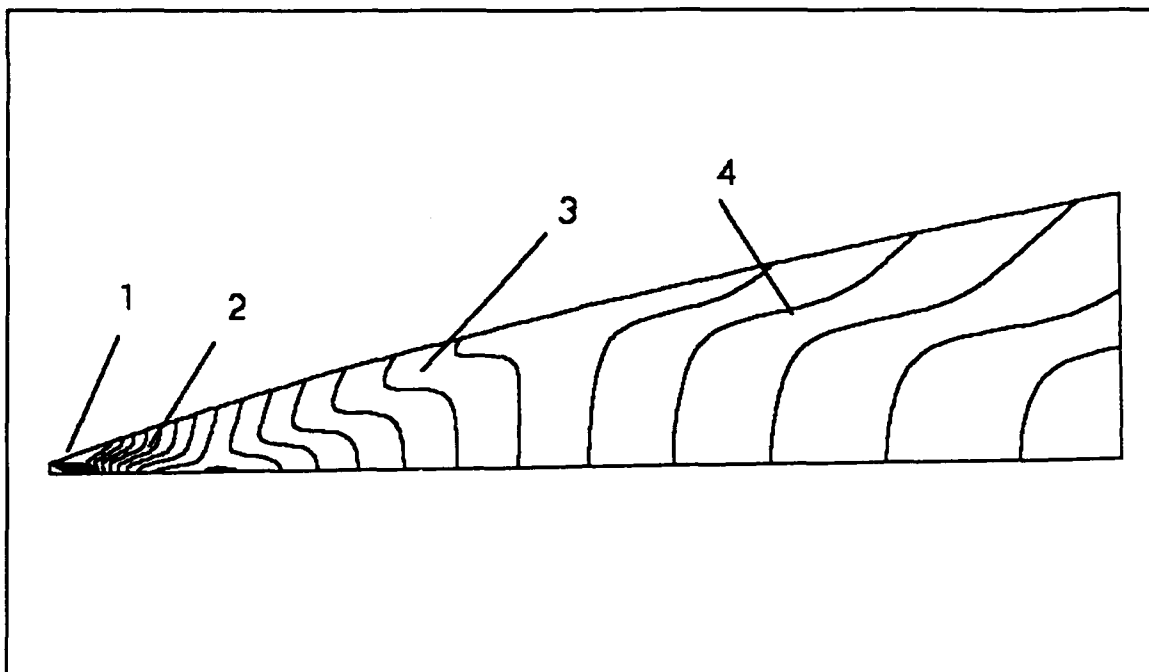


**Figure 4.3.** Static pressure contours (atm), FDS frozen flow solution,  $M=10$ , 20.6 deg parabolic nozzle contour.

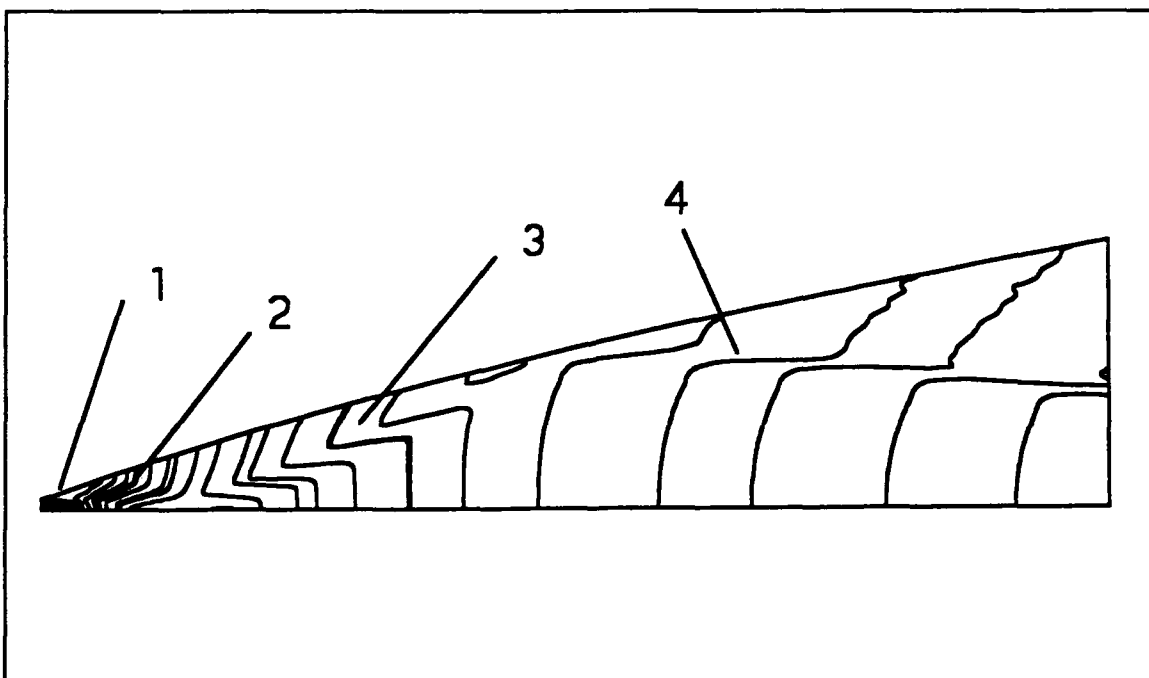


**Figure 4.4.** Static pressure contours (atm), SCHNOZ inviscid frozen flow solution,  $M=10$ , 20.6 deg parabolic nozzle contour.

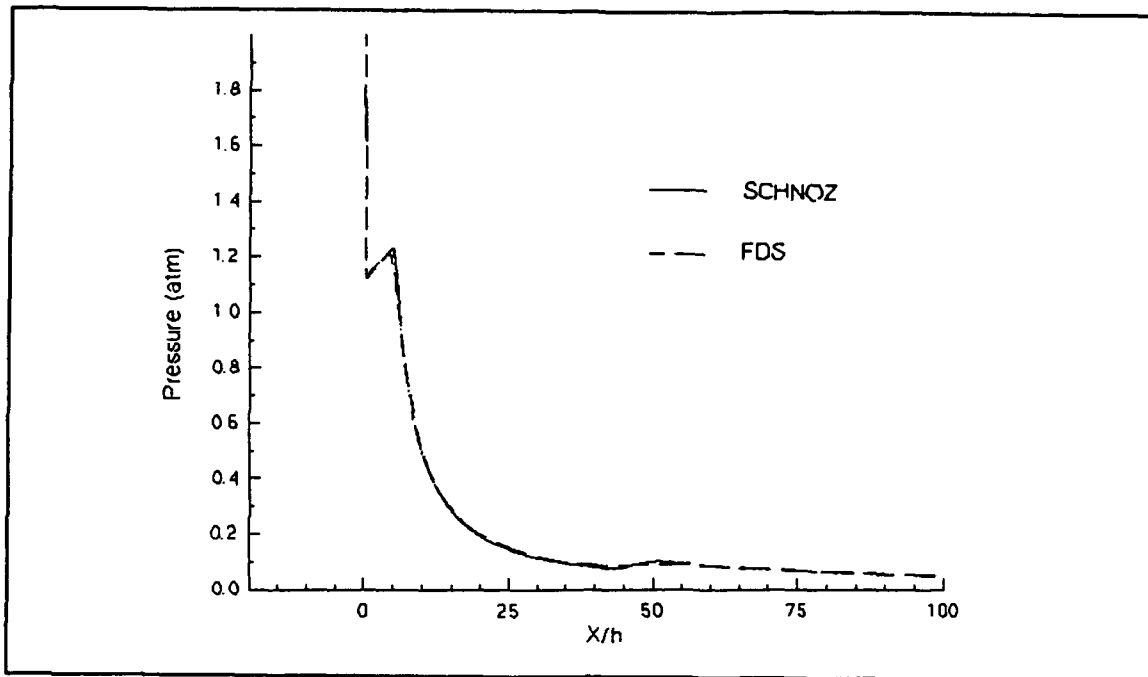


**Figure 4.5.** Static pressure distribution along nozzle wall, FDS and SCHNOZ inviscid solutions, frozen flow,  $M=10$ , 20.6 deg parabolic nozzle contour.

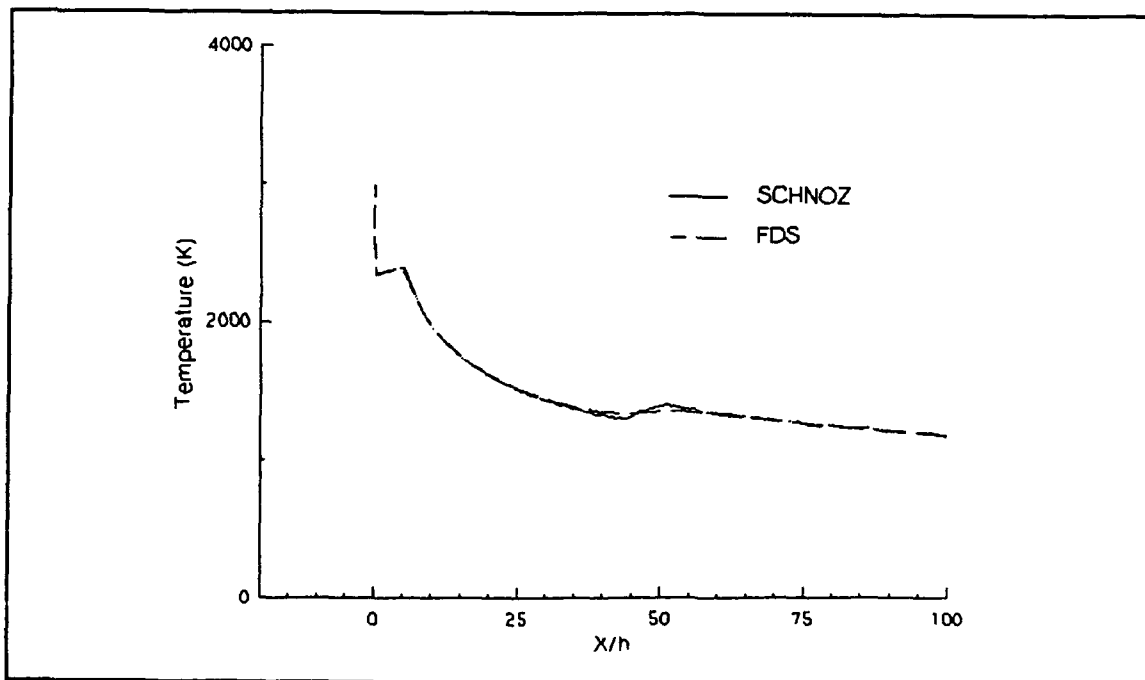


**Figure 4.6.** Static temperature distribution along nozzle wall, FDS and SCHNOZ inviscid solutions, frozen flow,  $M=10$ , 20.6 deg parabolic nozzle contour.

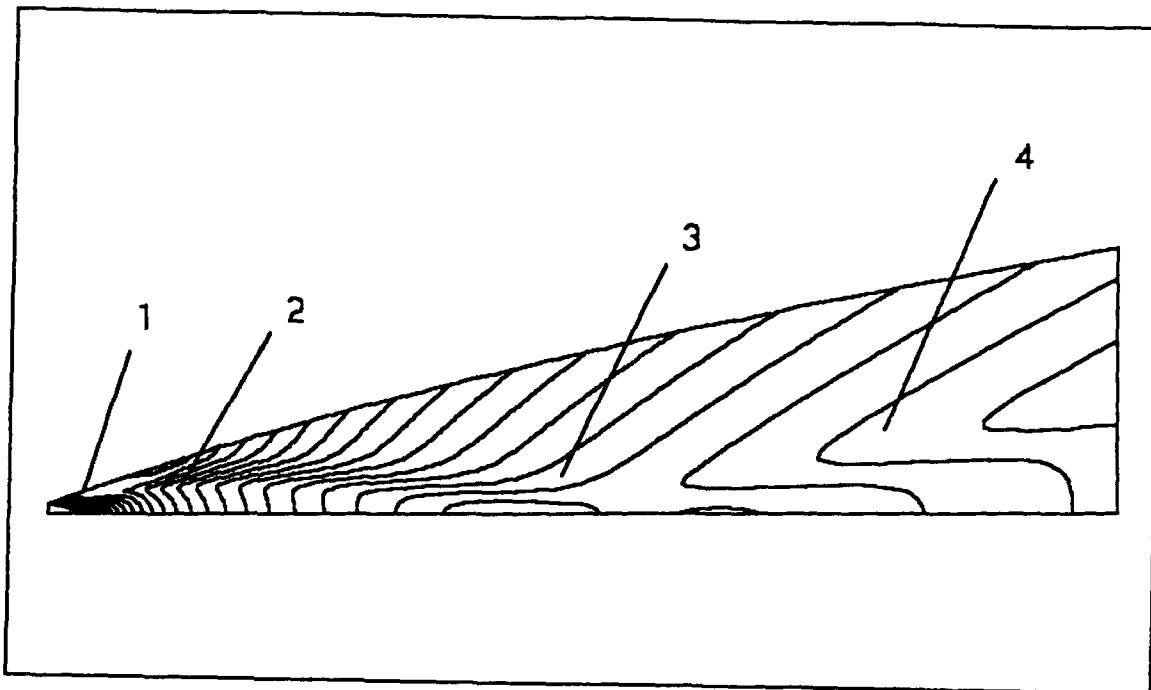


**Figure 4.7.** Static pressure contours (atm), FDS frozen flow solution,  $M=15$ , 20.6 deg parabolic nozzle contour.

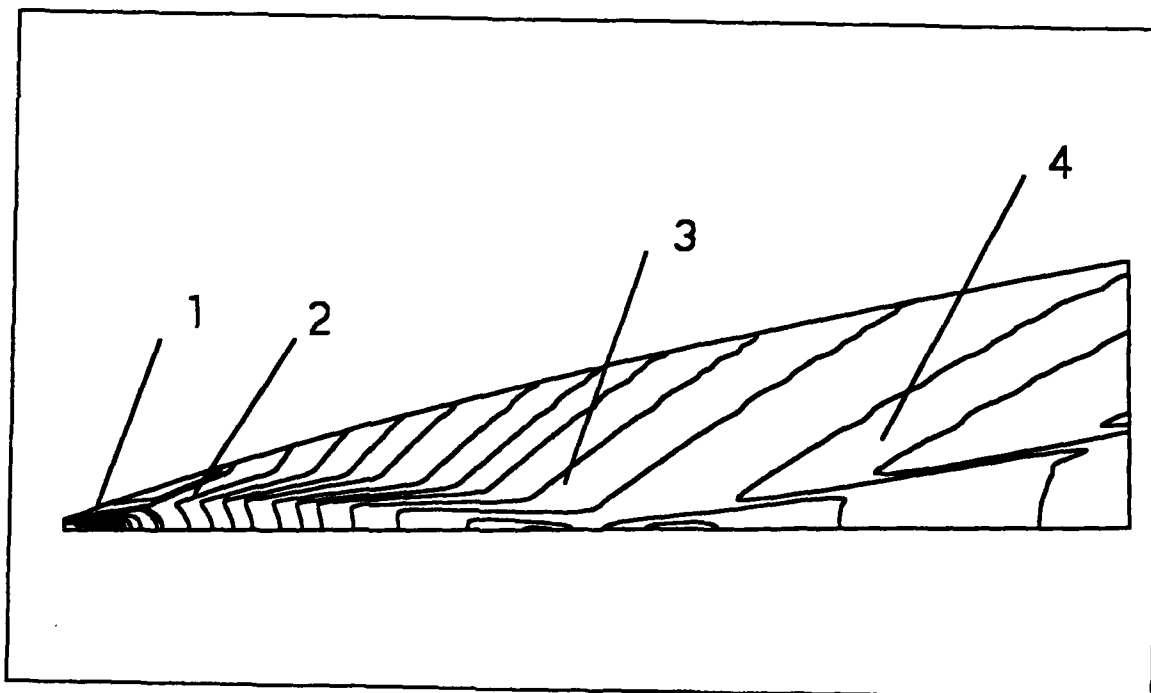


**Figure 4.8.** Static pressure contours (atm), SCHNOZ inviscid frozen flow solution,  $M=15$ , 20.6 deg parabolic nozzle contour.

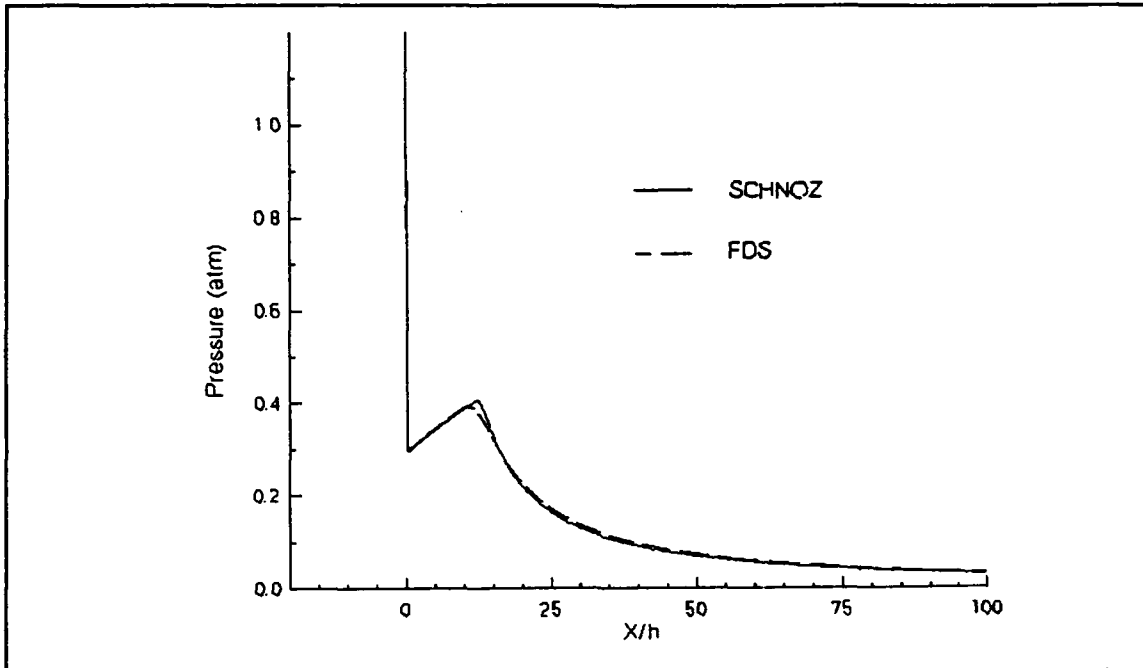


**Figure 4.9.** Static pressure distribution along nozzle wall, FDS and SCHNOZ inviscid solutions, frozen flow,  $M=15$ , 20.6 deg parabolic nozzle contour.

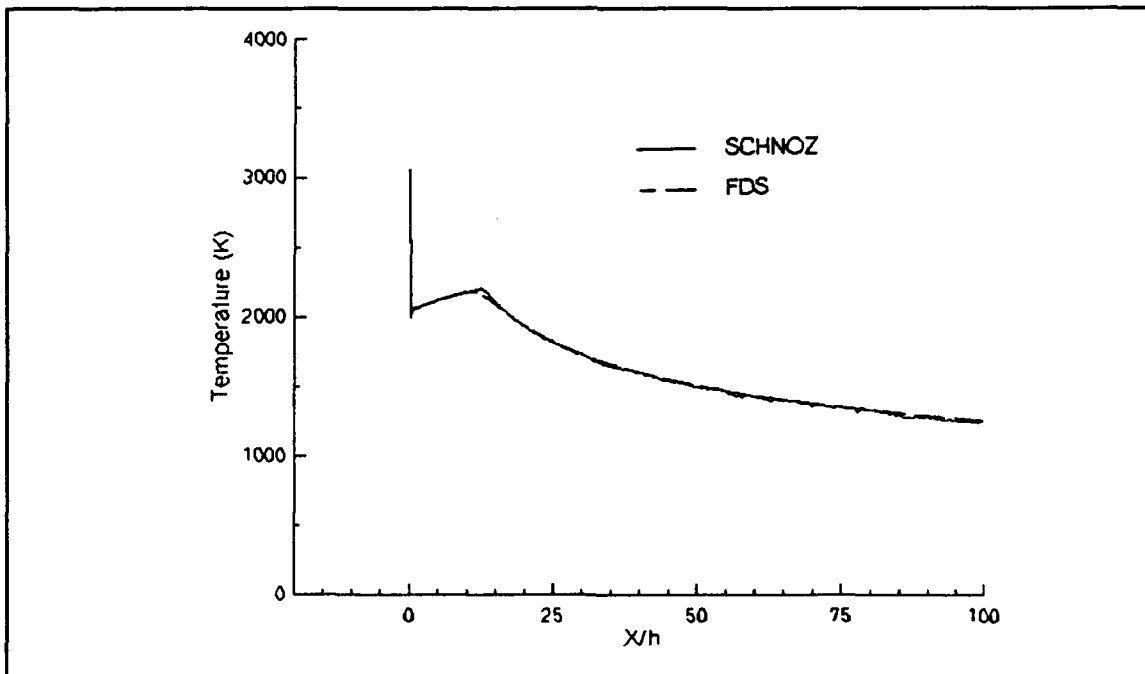


**Figure 4.10.** Static temperature distribution along nozzle wall, FDS and SCHNOZ inviscid solutions, frozen flow,  $M=15$ , 20.6 deg parabolic nozzle contour.

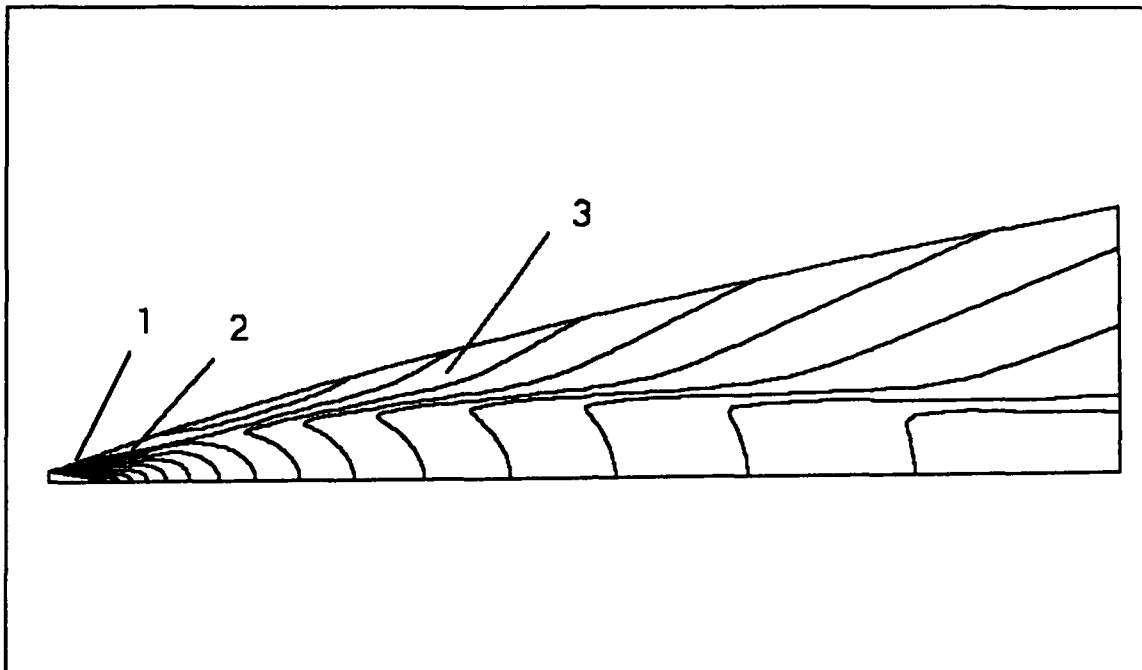


**Figure 4.11.** Static pressure contours (atm), FDS frozen flow solution,  $M=20$ , 20.6 deg parabolic nozzle contour.

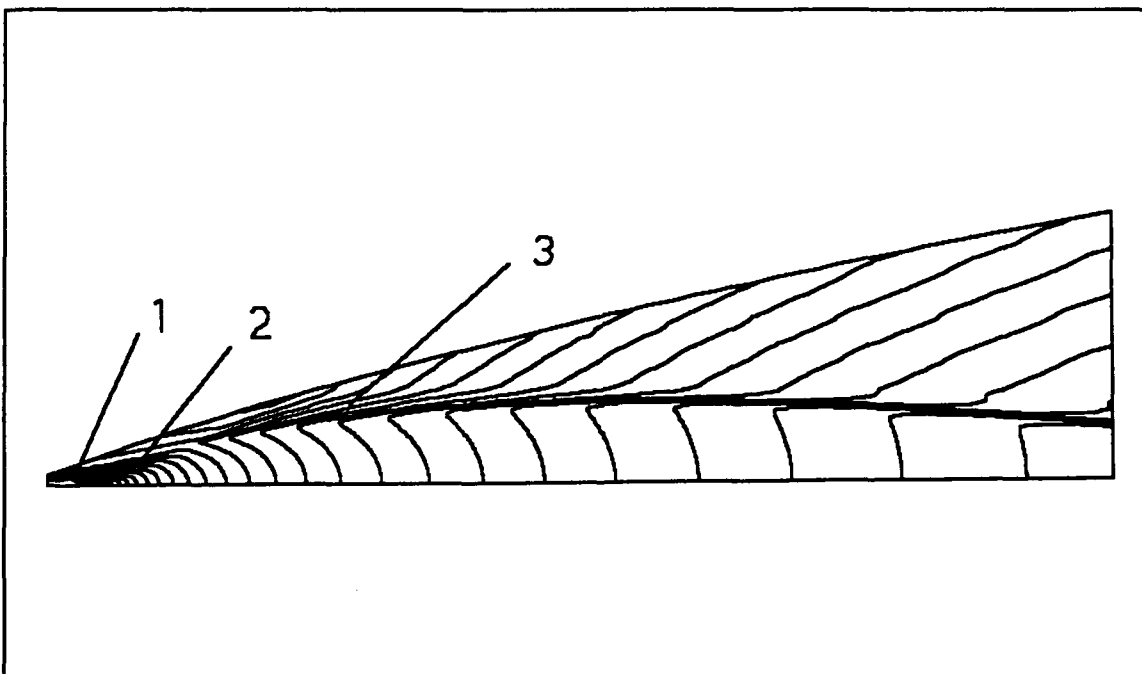


**Figure 4.12.** Static pressure contours (atm), SCHNOZ inviscid frozen flow solution,  $M=20$ , 20.6 deg parabolic nozzle contour.

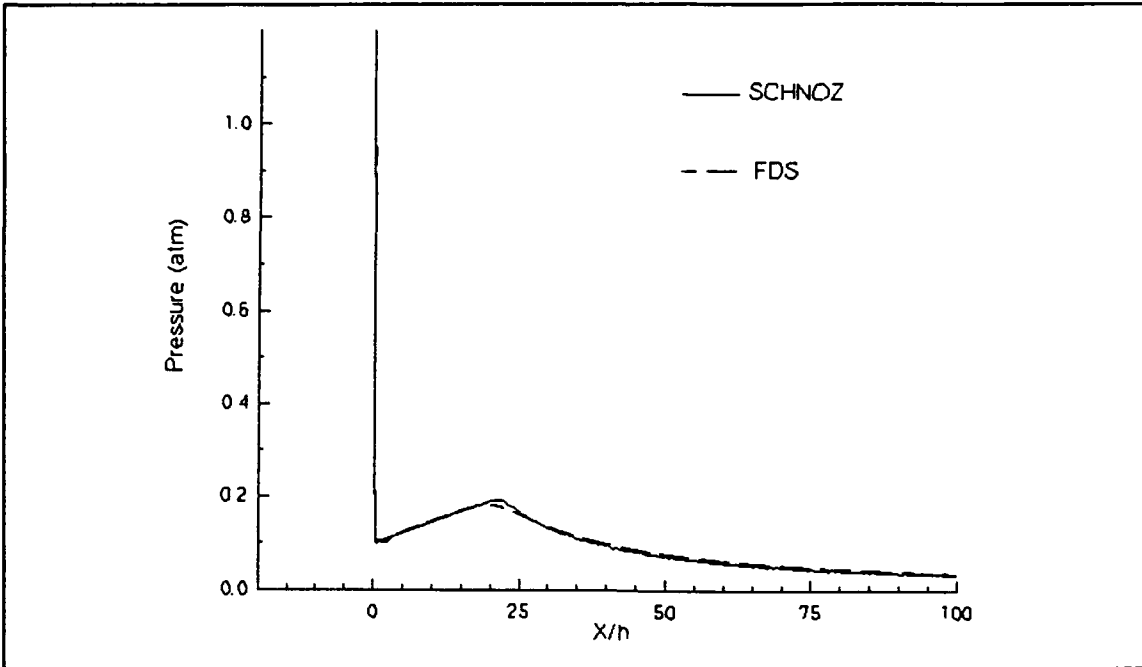


**Figure 4.13.** Static pressure distribution along nozzle wall, FDS and SCHNOZ inviscid solutions, frozen flow,  $M=20$ , 20.6 deg parabolic nozzle contour.

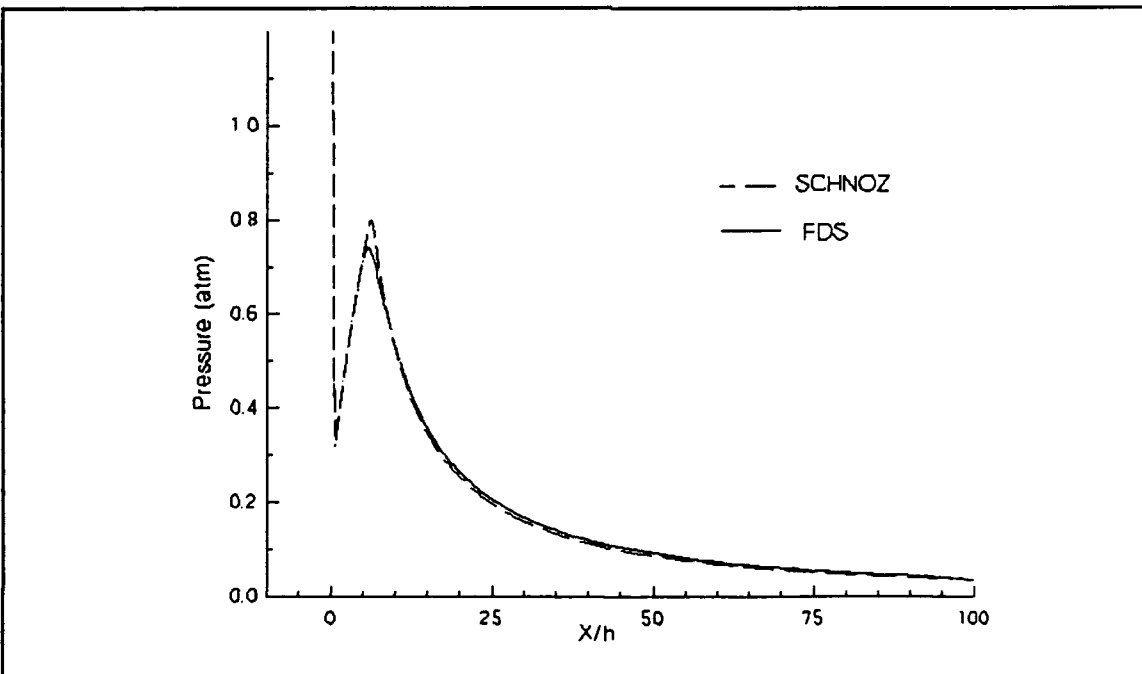


**Figure 4.14.** Static pressure distribution along nozzle wall, FDS and SCHNOZ inviscid solutions, frozen flow,  $M=10$ , 38 deg parabolic nozzle contour.



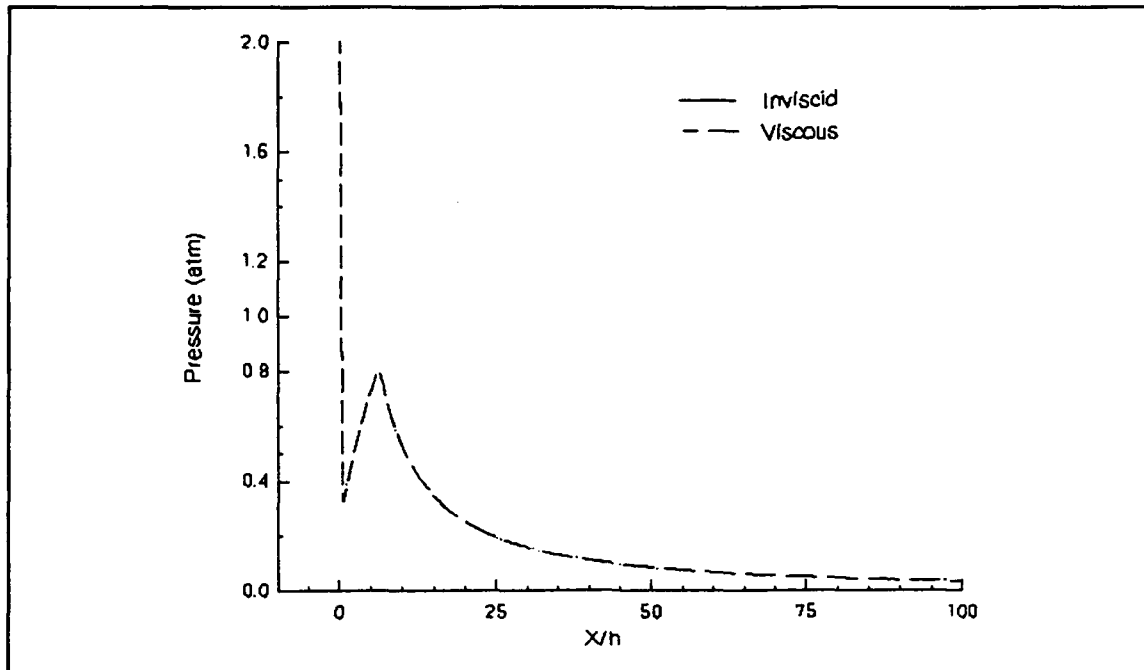


**Figure 4.15.** Static pressure distribution along nozzle wall, SCHNOZ viscous and inviscid solutions, frozen flow,  $M=10$ , 38 deg parabolic nozzle.

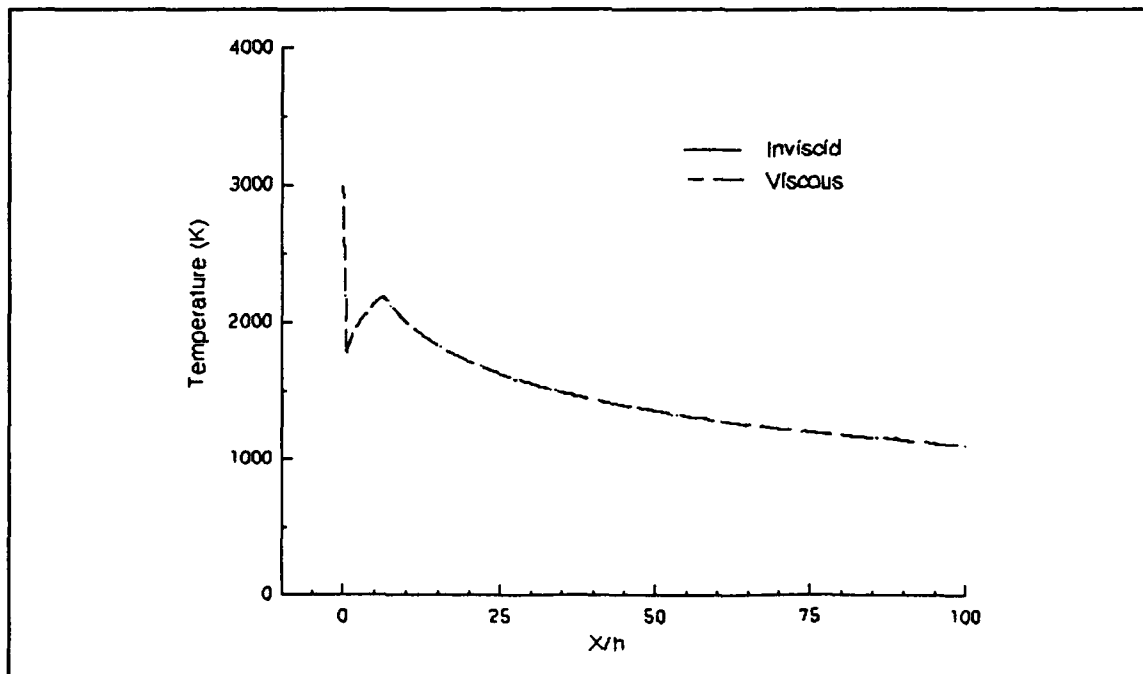


**Figure 4.16.** Static temperature distribution along nozzle wall, SCHNOZ viscous and inviscid solutions, frozen flow,  $M=10$ , 38 deg parabolic nozzle.

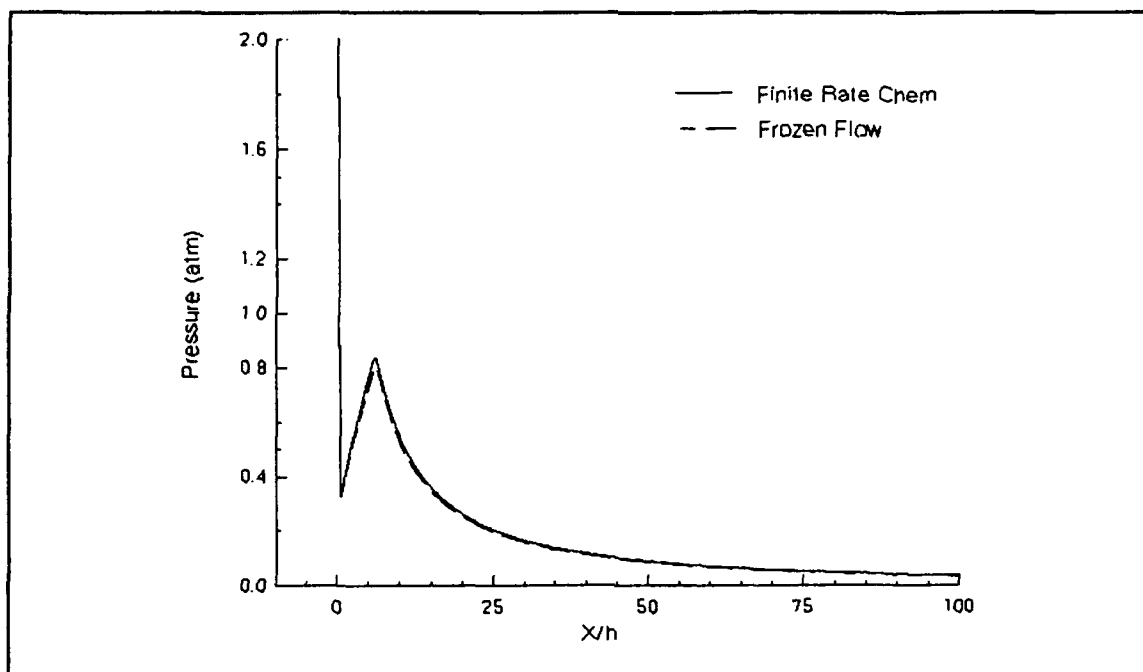


**Figure 4.17.** Static pressure distribution along nozzle wall, SCHNOZ frozen and finite rate chemistry viscous solutions,  $M=10$ , 38 deg nozzle.

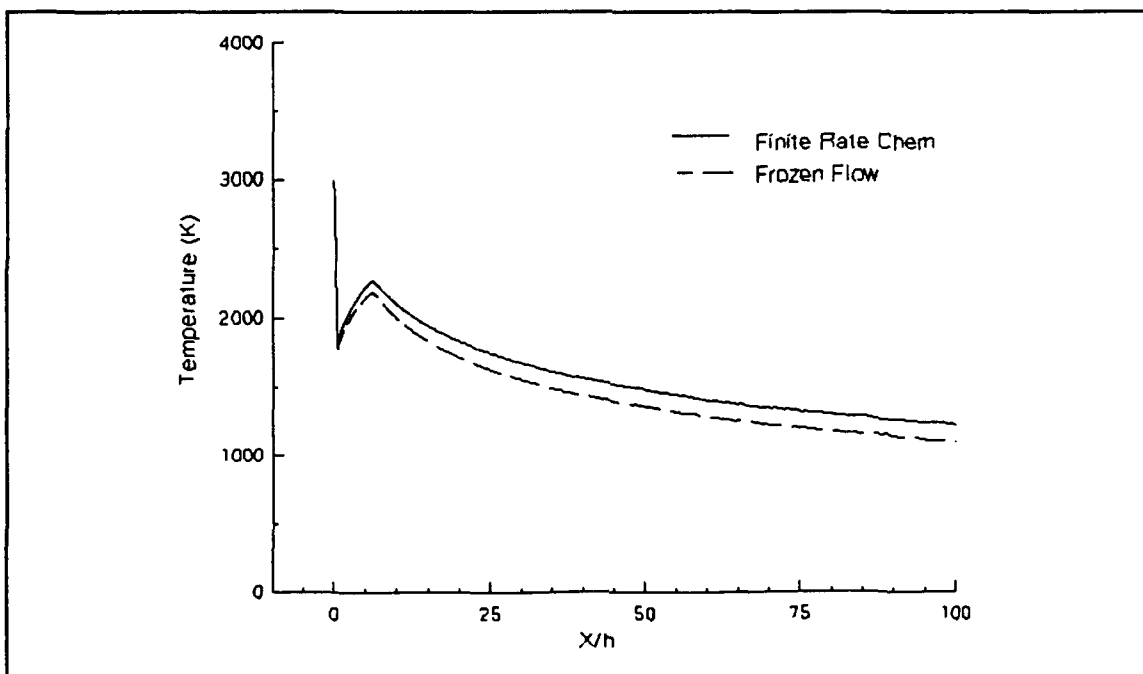


**Figure 4.18.** Static temperature distribution along nozzle wall, SCHNOZ frozen and finite rate chemistry viscous solutions,  $M=10$ , 38 deg nozzle.

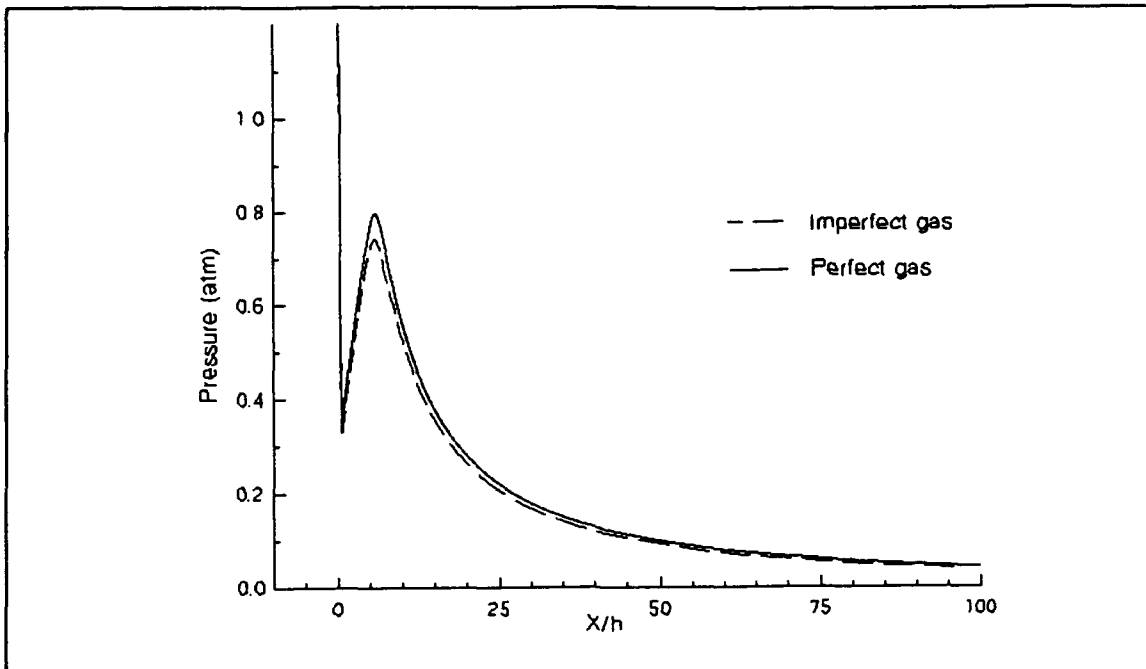


**Figure 4.19.** Static pressure distribution along nozzle wall, FDS perfect and imperfect gas solutions,  $M=10$ , 38 deg parabolic nozzle contour.

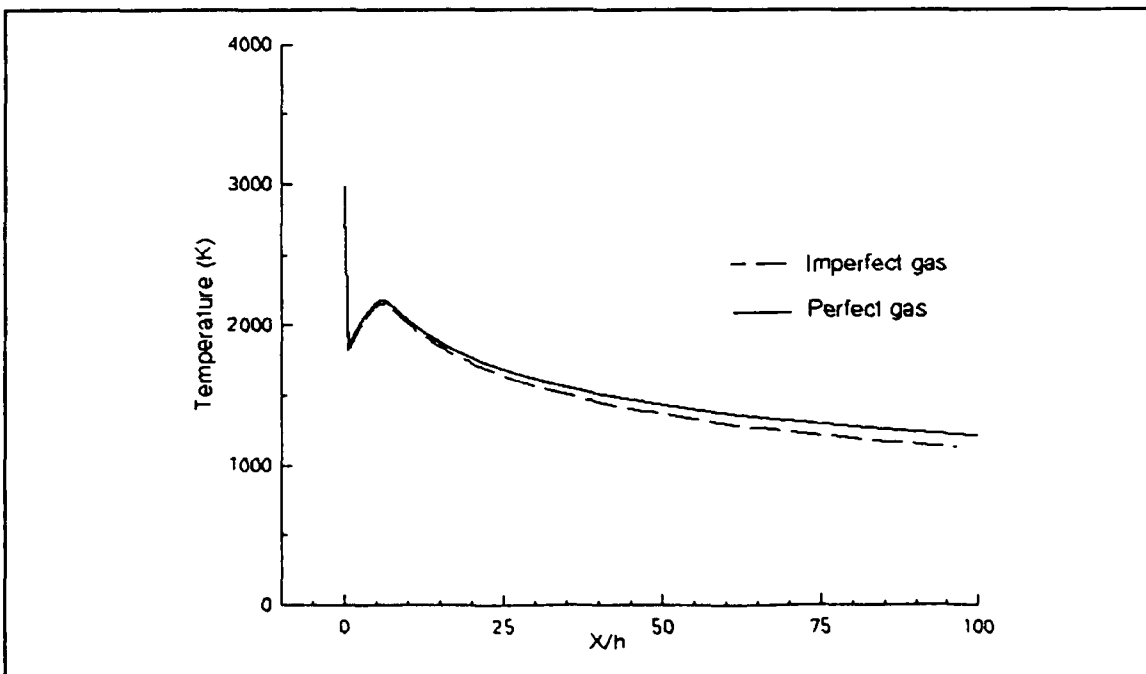


**Figure 4.20.** Static temperature distribution along nozzle wall, FDS perfect and imperfect gas solutions,  $M=15$ , 38 deg parabolic nozzle contour.

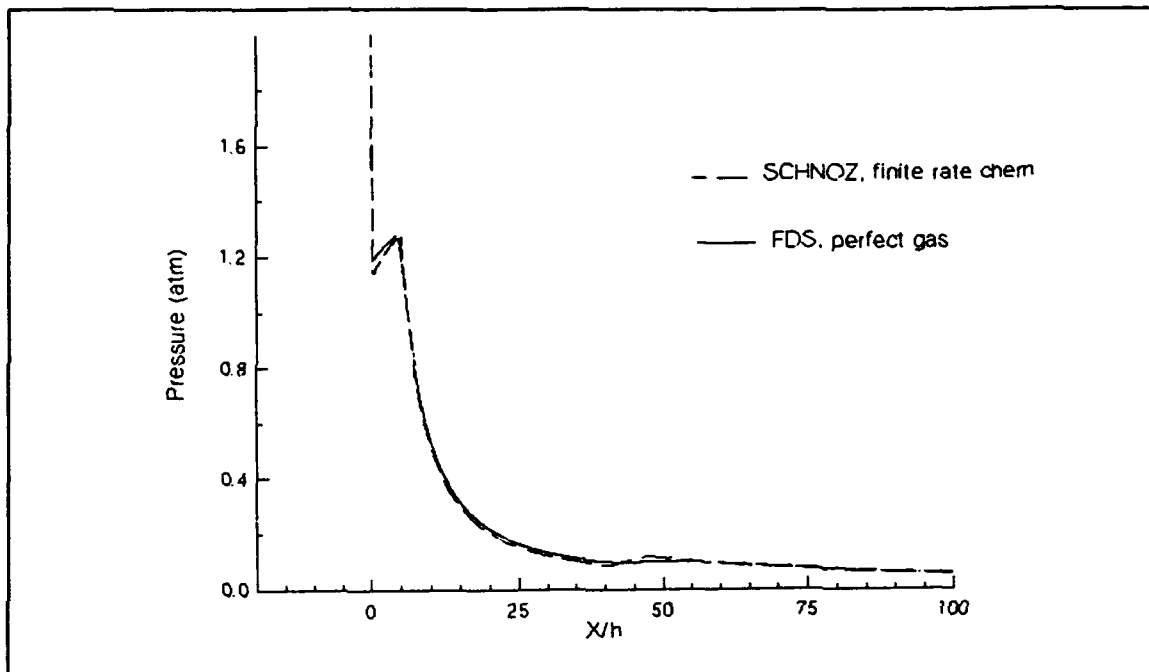


**Figure 4.21.** Static pressure distribution along nozzle wall, SCHNOZ finite-rate chemistry and FDS perfect gas solutions,  $M=10$ , 20.6 deg nozzle.

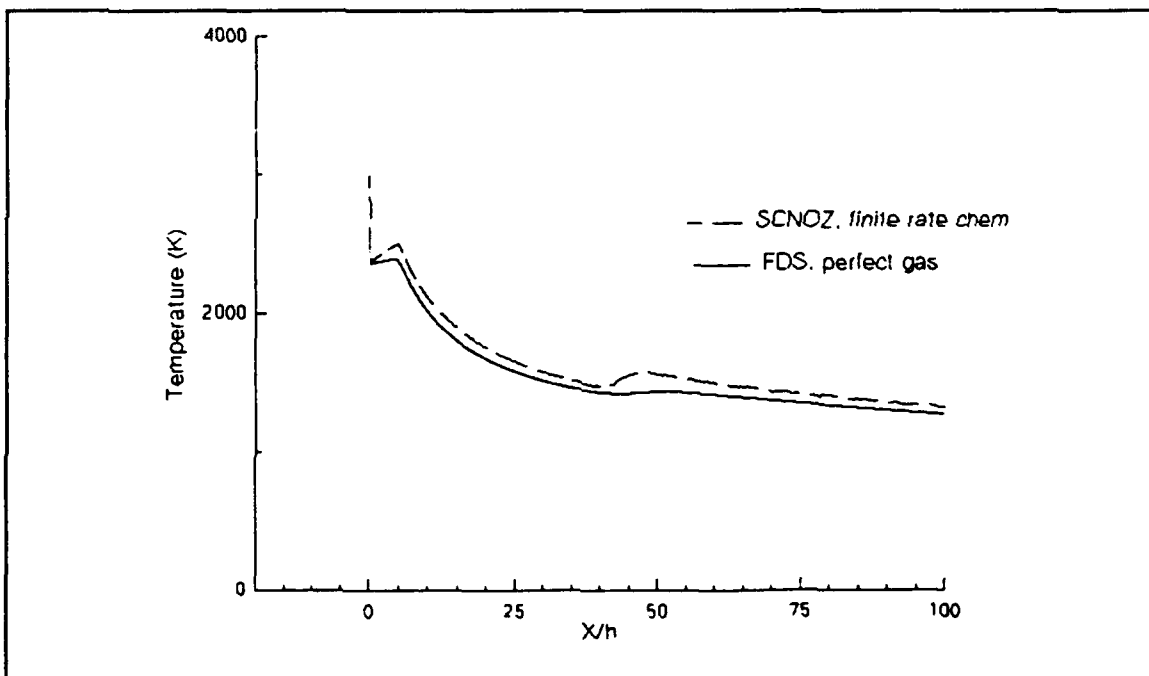


**Figure 4.22.** Static temperature distribution along nozzle wall, SCHNOZ finite-rate chemistry and FDS perfect gas solutions,  $M=10$ , 20.6 deg nozzle.

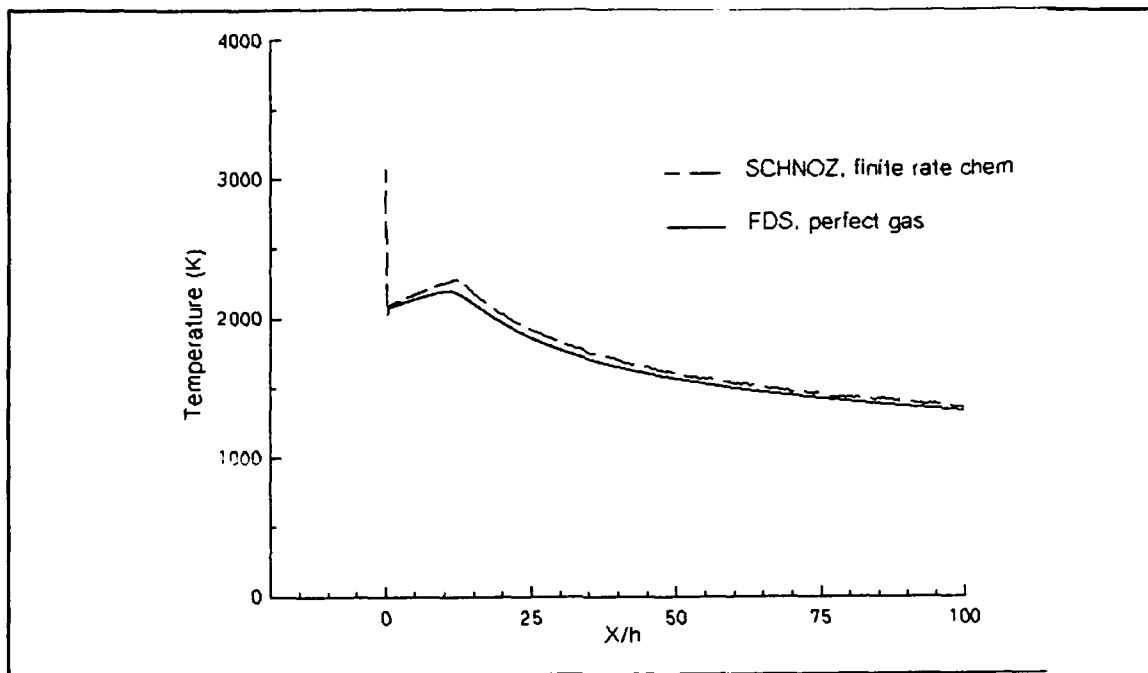


**Figure 4.23.** Static temperature distribution along nozzle wall, SCHNOZ finite-rate chemistry and FDS perfect gas solutions,  $M=15$ , 20.6 deg nozzle.

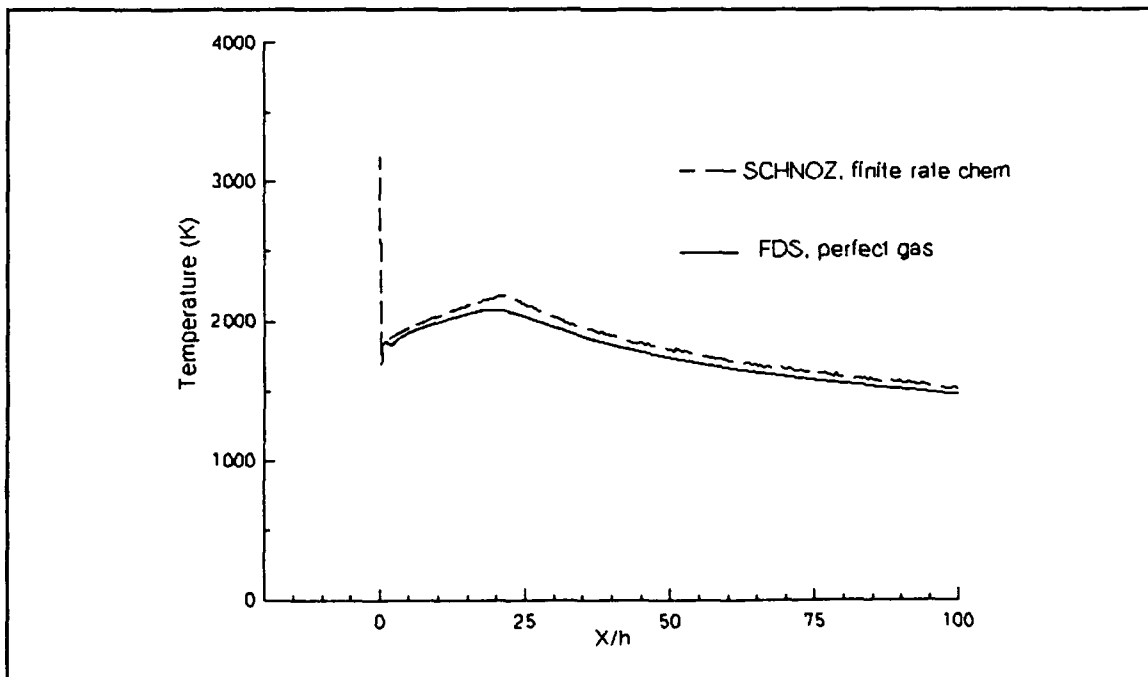


**Figure 4.24.** Static temperature distribution along nozzle wall, SCHNOZ finite-rate chemistry and FDS perfect gas solutions,  $M=20$ , 20.6 deg nozzle.

## V. Conclusions/Recommendations

### 5.1 Conclusions

The overall comparison of the two computational methodologies revealed that currently the SCHNOZ code is more efficient than the FDS frozen flow code for analyzing a given nozzle inlet profile and geometry. The SCHNOZ and FDS code demonstrate a good agreement in modeling the flow physics in the hypersonic nozzle. The inclusion of viscosity, turbulence, and finite rate chemistry models should make the SCHNOZ code more accurate. However, the implementation of the solid wall slip boundary condition to remove the subsonic portion of the viscous boundary layer fails to truly model the effects of viscosity in the nozzle flowfield. The chemistry effects in the nozzle flowfield have a small (less than 5%) effect on the overall nozzle thrust. However, even these small thrust differences are significant in the optimized design of a NASP-type vehicle and the inclusion of finite rate chemistry effects should be incorporated into the computational solution.

The FDS code utilizing the perfect gas assumption is useful and efficient in optimizing a nozzle or cowl geometry for a given inlet condition. The perfect gas FDS results show the proper trends in flow phenomena and flowfield properties, and provide a good ballpark design to analyze by a more accurate method. The added CPU time of the more

accurate FDS frozen flow, compared to the perfect gas, is attributable to the additional iterations required in the solution of the Riemann problem and the flux vector decode. This added CPU time greatly reduces the efficiency of the FDS method. An improved iteration scheme for the frozen gas thermodynamic model for the FDS could should markedly improve its performance in terms of CPU time.

## 5.2 Recommendations

According to the SCHNOZ operator's manual (20), a new version of the SCHNOZ code was to be developed that includes a viscous sublayer model and an option for equilibrium chemistry. Future computations of the nozzle flowfield should be run with this version of the SCHNOZ code or a different PNS code that includes the viscous sublayer model to better capture the viscous flow effects. With proper consideration of the viscous effects on the solution, a study to determine whether the PNS equations are necessary to model the flow physics would prove beneficial.

Continual improvements in computational methodologies and computational capabilities need to be investigated and analyzed to meet the demanding challenges of the hypersonic propulsive nozzle environment. The current version of the SCHNOZ program is not optimized for use on a supercomputer, and the FDS code is not vectorizable because of the nature of the solution to the Riemann problem. Future studies

should be made into the efficiency, in terms of computational time and cost, for a vectorizable PNS code run on a supercomputer.

The true accuracy of the computer codes can only be determined by a comparison to exact solutions. In lieu of unlikely actual flight test data, an unclassified experimental analysis of a simple nozzle geometry should be undertaken to validate the findings and trends of computational runs. Also, computational runs using actual combustor exit data would prove to be of merit in comparison to previously assumed or derived nozzle inlet profiles.



## Bibliography

- (1) Anderson, John D. *Hypersonic and High Temperature Gas Dynamics*. New York: McGraw-Hill, Inc., 1989.
- (2) Anderson, D. A., Tannehill, J. C., Pletcher, R. H. *Computational Fluid Mechanics and Heat Transfer*. New York: Hemisphere Publishing Corp., 1984.
- (3) Chakravarthy, S. R. *Development of Upwind Schemes for the Euler Equations*. NASA CR-4043, 1987.
- (4) Dash, Sanford M., and Wolf, David E. "Interactive Phenomena in Supersonic Jet Mixing Problems, Part I: Phenomenology and Numerical Modeling Techniques," *AIAA Journal*, 22: 905-912 (July 1984).
- (5) Dash, Sanford M., and Wolf, David E. "Analysis of Turbulent Underexpanded Jets, Part I: Parabolized Navier-Stokes Model, SCIPVIS," *AIAA Journal*, 23: 505-513 (April 1985).
- (6) Doty, John H. *Performance Prediction and Design of Maximum Thrust Planar Supersonic Nozzles Using a Flux-Difference-Splitting Technique*. PhD Dissertation. Purdue University, Lafayette, Indiana, 1991.
- (7) Grossman, B. and Walters, R. W. "Flux-Split Algorithms for the Multi-Dimensional Euler Equations with Real Gases," *Computers & Fluids*, 17: 99-112, (1989).
- (8) Herring, Dave. "Design of an Optimum Thrust Nozzle for a Typical Hypersonic Trajectory Through Computational Analysis," MS Thesis, AFIT/GAE/ENY/91D-11. School of Engineering, Air Force Institute of Technology (AU), Wright-Patterson AFB OH, December 1991.
- (9) Long, Lyle N., Khan, M. M. S., and Sharp, H. Thomas. "Massively Parallel Three-Dimensional Euler/Navier Stokes Method," *AIAA Journal*, 29: 657-666 (May 1991).
- (10) Pandolfi, Maurizo. "Computation of Steady Supersonic Flows by a Flux Difference Splitting Method," *Computers and Fluids*, 13: 37-46, (1985).
- (11) Pandolfini, P. *Instructions for Using RAMJET Performance Analysis (RJPA) - IBM-PC Version 1.0*. Contract JHU/APL-NASP-86-2. Laurel, MD: The John Hopkins University Applied Physics Laboratory, November, 1986.

- (12) Roe, P. L. "Approximate Riemann Solvers, Parameter Vectors, and Difference Schemes," *Journal of Computational Physics*, 43: 357-372 (October 1981).
- (13) Schieve, Mark E. "Improvement of the Thermodynamic Model for a Flux-Difference Splitting Algorithm for the Computation of High Speed Flows," MS Thesis, AFIT/GAE/ENY/91D-10. School of Engineering, Air Force Institute of Technology (AU), Wright-Patterson AFB OH, December 1991.
- (14) Sisilian, J.P., *Equations of Motion and Two-Equation Turbulence Model for Plane or Axisymmetric Turbulent Flows in Body-Oriented Orthogonal Curvilinear Coordinates and Mass-Averaged Dependent Variables*, NASA CR3025, Aug 1978.
- (15) Snelling, Sandra L. "Effect of Nonuniform Entrance Flow Profile on Hypersonic Nozzle Pitching Moment," MS Thesis, AFIT/GAE/ENY/91D-13. School of Engineering, Air Force Institute of Technology (AU), Wright-Patterson AFB OH, December 1991.
- (16) Sod, G. A. "A Survey of Several Finite Difference Methods for Systems of Nonlinear Hyperbolic Conservation Laws," *Journal of Computational Physics*, 27: 1-31, (April 1978).
- (17) Steger, J. L. and R. F. Warming. "Flux Vector Splitting of the Inviscid Gasdynamic Equations with Applications to Finite-Difference Methods," *Journal of Computational Physics*, 40: 263-293, (April 1981).
- (18) Vincenti, Walter G. and Kruger, Charles H., Jr. *Introduction to Physical Gas Dynamics*. Malabar, FL: Robert E. Krieger Publishing Company, 1965.
- (19) Walton, James T. *An Overview of Airframe Integrated Scramjet Cycle Components and Flow Features*, NASP TM1029, Nov 1988.
- (20) Wolf, David E., Lee, Robert A. and Dash, Sanford M. *Analysis of Aerospace Vehicle Scramjet Propulsive Flowfields: 2D Nozzle Development -- Phase 1*, NASP CR1005, Aug 1987.
- (21) Zhang, H. S. and R. M. So. "A Flux-Coordinate-Splitting Technique for Flows with Shocks and Contact Discontinuities," *Computers and Fluids*, 20: 421-442, (1991).

## Appendix A: Governing Equations

### A.1 Parabolized Navier-Stokes (PNS) Equations

The set of PNS equations implemented in the SCHNOZ code were derived from the full Navier-Stokes equations using time-averaging of density, pressure, and viscous stresses and mass-averaging of the remaining variables (15:2-1). Using Reynold's averaging and ignoring unsteady terms and streamwise derivatives of viscous stress terms, the turbulent Navier-Stokes equations were parabolized (4:907). Ignoring turbulent stress terms in the normal momentum equation and diffusion terms in the energy equation, because of an assumed unity Lewis number (4:907), the resulting planar PNS equations are obtained:

*Continuity:*

$$\frac{\partial(\rho u)}{\partial x} + \frac{\partial(\rho v)}{\partial y} = 0 \quad (\text{A.1})$$

*X-Momentum:*

$$\frac{\partial(p + \rho u^2)}{\partial x} + \frac{\partial(\rho uv)}{\partial y} = \frac{\partial}{\partial y} \left( \bar{\mu} \frac{\partial u}{\partial y} \right) \quad (\text{A.2})$$

*Y-Momentum:*

$$\frac{\partial(\rho uv)}{\partial x} + \frac{\partial(p + \rho v^2)}{\partial y} = \frac{\partial}{\partial y} \left( \bar{\mu} \frac{\partial v}{\partial y} \right) \quad (\text{A.3})$$

*Total Enthalpy:*

$$\frac{\partial(\rho u H)}{\partial x} + \frac{\partial(\rho v H)}{\partial y} - \frac{\partial}{\partial y} \left[ \frac{(\overline{Pr}-1)}{\overline{Pr}} \bar{\mu} \frac{\partial}{\partial y} \left( \frac{u^2}{2} \right) \right] = \frac{\partial}{\partial y} \left( \frac{\bar{\mu}}{\overline{Pr}} \frac{\partial H}{\partial y} \right) \quad (\text{A.4})$$

Full details on the derivation of these equations are available in the work of Sisilian (14) and their application to the SCHNOZ code is presented by Dash (20).

For chemically reacting viscous flows a finite-rate chemistry model is used, and an additional equation is added to the PNS equation set to account for the various species continuity:

$$\frac{\partial(\rho u \alpha_i)}{\partial x} + \frac{\partial(\rho v \alpha_i)}{\partial y} - \dot{\omega}_i = \frac{\partial}{\partial y} \left( \frac{\bar{\mu}}{\overline{Pr}} \frac{\partial \alpha_i}{\partial y} \right) \quad (\text{A.5})$$

where the subscript *i* represents the individual species considered.

## A.2 Turbulence Model

Due to computer limitations and the small space scales of turbulent motion, the effects of turbulent dissipation and diffusion are only computationally feasible using turbulence models (9:659). The SCHNOZ program contains two turbulence models, the *kε* and *kW* high Reynolds number versions. The turbulence model used in this study is the common two-equation *kε* eddy viscosity version which models the turbulent kinetic energy, *k*, and energy dissipation, *ε*. The turbulent viscosity, *μ<sub>t</sub>*, is determined from:

$$\mu_t = C_\mu \rho k^{\frac{1}{2}} \ell = C_\mu \rho \frac{k^2}{\epsilon} \quad (\text{A.6})$$

where the length scale parameter used is the turbulence energy dissipation rate,  $\epsilon$  (5:507). The energy dissipation rate is related to  $k$  and the turbulent length scale,  $\ell$ , through the following relation (15:10):

$$\epsilon = \frac{k^{3/2}}{\ell} \quad (\text{A.7})$$

The parabolized form of the turbulence modelling equations are developed from the full Navier-Stokes equations for the production, transport, and dissipation of  $k$  and  $\epsilon$  with the omission of all axial derivatives (5:507). For planar flow the turbulence equations are then given by:

$$\frac{\partial}{\partial x} (\rho u k) + \frac{\partial}{\partial y} (\rho v k) = \frac{\partial}{\partial y} \left( \frac{\mu_t}{\sigma_k} \frac{\partial k}{\partial y} \right) + \left[ \mu_t \left( \frac{\partial u}{\partial y} \right)^2 - \rho \epsilon \right] \quad (\text{A.8})$$

and :

$$\frac{\partial}{\partial x} (\rho u \epsilon) + \frac{\partial}{\partial y} (\rho v \epsilon) = \frac{\partial}{\partial y} \left( \frac{\mu_t}{\sigma_\epsilon} \frac{\partial \epsilon}{\partial y} \right) + \left[ C_1 \mu_t \left( \frac{\partial u}{\partial y} \right)^2 - C_2 \rho \epsilon \right] \frac{\epsilon}{k} \quad (\text{A.9})$$

The constants used in the parabolized turbulence modelling equations are (15:10):

$$\begin{aligned} C_1 &= 1.43 & \sigma_k &= 1.0 \\ C_2 &= 1.92 & \sigma_\epsilon &= 1.3 \\ C_\mu &= 0.09 \end{aligned}$$

The  $k\epsilon$  model is developed from incompressible

assumptions and overestimates mixing rates for high Mach number flows, such as those in a hypersonic nozzle (5:507). Therefore, a compressibility correction,  $K(M_t)$ , is employed in the SCHNOZ code to arrive at a corrected value of the turbulent viscosity given by:

$$\mu_t = K(M_t) C_\mu \rho \frac{k^2}{\epsilon} \quad (\text{A.10})$$

where  $M_t$  is the characteristic Mach number of the turbulence (5:507). This characteristic Mach number of the turbulence is found from:

$$M_t = \frac{k_{\max}}{a_{\max}} \quad (\text{A.11})$$

where  $k_{\max}$  is the maximum value of  $k$  at each axial location and  $a_{\max}$  is the local speed of sound at each  $k_{\max}$  (5:507). The values of  $K(M_t)$  are determined from comparison with experimental data and are shown in Figure A.1 (5:507).

### A.3 Euler Equations

The Euler equations are the zero viscosity and zero conductivity limits of the Navier-Stokes equations (9:659). The effects of viscosity and the conduction of heat are not included in the Euler equations. The Euler equations as utilized in the FDS computer program of Doty are:

Continuity:

$$\frac{\partial(\rho u)}{\partial x} + \frac{\partial(\rho v)}{\partial y} = 0 \quad (\text{A.12})$$

X-Momentum:

$$\frac{\partial(p + \rho u^2)}{\partial x} + \frac{\partial(\rho v u)}{\partial y} = 0 \quad (\text{A.13})$$

Y-Momentum:

$$\frac{\partial(\rho u v)}{\partial x} + \frac{\partial(p + \rho v^2)}{\partial y} = 0 \quad (\text{A.14})$$

Total Energy:

$$\frac{\partial[u(\rho e + p)]}{\partial x} + \frac{\partial[v(\rho e + p)]}{\partial y} = 0 \quad (\text{A.15})$$

Traditionally, solutions of the Euler equations require significantly less computational time than comparable PNS equation solutions (2:236).

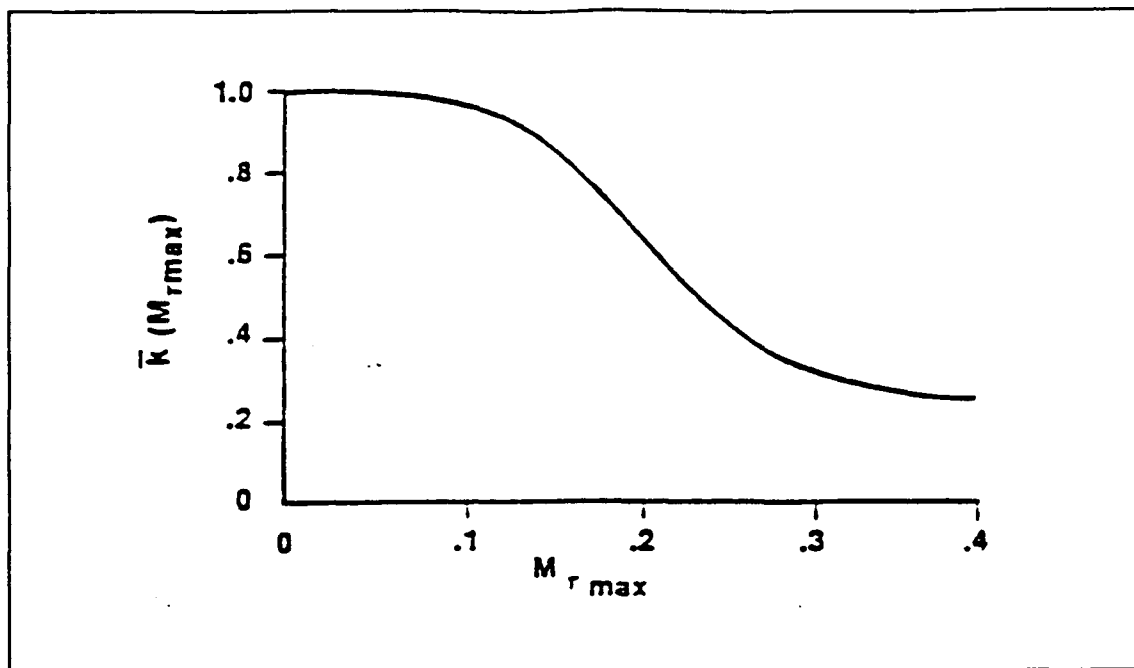


**Figure A.1.** Compressibility correction factor for  $k\epsilon$  turbulence model (20:11)



## Appendix B: Thermodynamic Model

### B.1 Perfect Gas

The thermodynamic model employed greatly influences the determination of flow properties within the hypersonic nozzle. The complexity of the thermodynamic models depend on the degree to which the model actually captures the true physics of the flow (13:51). The simplest model is the perfect gas. A calorically perfect gas model assumes no intermolecular forces and constant specific heats,  $c_v$  and  $c_p$ , resulting in a constant specific heat ratio,  $\gamma$ . The perfect gas obeys the thermal equation of state (1:381):

$$p = \rho RT \quad (\text{B.1})$$

where  $R$  is the gas constant determined by the molecular weight,  $MW$ , of the gas and the universal gas constant,  $R_{univ}$ :

$$R = \frac{R_{univ}}{MW} \quad (\text{B.2})$$

A perfect gas assumes no change in the molecular composition of the gas. Hence,  $R$  remains constant since there is no mechanism to change the  $MW$  of the gas. The enthalpy and internal energy of a calorically perfect gas are functions only of temperature (1:388).

$$h = h(T) = c_p T \quad (\text{B.3})$$

$$\hat{u} = \hat{u}(T) = c_v T \quad (\text{B.4})$$

The total internal energy for a calorically perfect gas is given by:

$$\rho e = \frac{p}{\gamma - 1} + \frac{1}{2} \rho (u^2 + v^2) \quad (\text{B.5})$$

The calorically perfect gas assumption is the most widely used assumption in flow analyses. However, the calorically perfect gas assumption breaks down when high temperatures are encountered within the flowfield. The perfect gas does not account for the internal structure of the molecule, nor does it allow for the dissociation of gaseous molecules with increasing temperature. These shortcomings are addressed by the calorically imperfect gas model and the finite-rate chemistry model, respectively.

## *B.2 Calorically Imperfect Gas*

The next step in complexity is the calorically imperfect gas. The calorically imperfect gas still assumes that intermolecular forces are negligible and obeys the thermal equation of state, Eq. (B.1). The basic difference between the calorically imperfect gas and perfect gas is in the recognition of the proper internal structure of the gaseous molecule and the modes of internal energy which may be excited. The differences in the two assumptions is

illustrated by considering air as a diatomic gas and ignoring the relatively small contributions of the electronic mode of energy (18:136).

In general the specific internal energy, now denoted by  $e$  and not  $u$ , for a gas is additive and represented by (18:128):

$$e_{total} = e_{trans} + \sum_{intern} e_{intern} \quad (B.6)$$

where  $e_{intern}$  represents the internal modes of energy available. For a diatomic gas such as air, the translational, rotational, and vibrational modes of energy are available, even at relatively moderate temperatures (18:222). Using a statistical mechanics derivation Vincenti and Kruger provide the following expressions for the translational, rotational, and vibrational internal modes of energy for a diatomic gas (18:133-135):

$$e_{trans} = \frac{3}{2}RT \quad (B.7)$$

$$e_{rot} = RT \quad (B.8)$$

$$e_{vib} = \frac{R\Theta_v}{e^{\Theta_v/T} - 1} \quad (B.9)$$

where  $\Theta_v$  is the characteristic temperature for vibration. The perfect gas assumption allows only for the translational and rotational internal modes of energy. The specific internal energy for a perfect gas is then given by:

$$e_{perfect} = e_{trans} + e_{rot} = \frac{5}{2}RT \quad (B.10)$$

The calorically imperfect gas, accounting for the internal energy mode of vibration is:

$$e_{total} = e_{trans} + e_{rot} + e_{vib} = \frac{5}{2}T + e_{vib} \quad (B.11)$$

Comparing Eqs. (B.10) and (B.11) shows that the energy of gaseous molecules is spread over more modes of energy for a calorically imperfect gas than for the perfect gas. This difference influences the determination of flow properties downstream of discontinuities. For perfect gas flow across a shock wave, the kinetic energy of the flow in front of the shock is converted to translational and rotational energy downstream of the shock. For the calorically imperfect gas, some of this kinetic energy conversion may be absorbed by the vibrational mode of energy, thus decreasing the amount of energy absorbed by the rotational and translational modes. Since temperature is a direct measurement of kinetic (translational) energy, the increased energy absorbed in the translational mode of the perfect gas, compared to the calorically imperfect gas, causes the perfect gas model to overpredict the temperature downstream of the shock (1:510).

### B.3 Complex Chemical Mixtures

The combustion products of a hydrogen-fueled air-breathing SCRAMjet engine are a complex mixture of gaseous species consisting largely of water and nitrogen. The specific heat for a mixture of  $n$  gaseous species is given by (1:387):

$$C_p = \sum_{i=1}^n C_i c_{p_i} \quad (\text{B.12})$$

where  $C_i$  is the mass fraction of the species. The specific heat of the species,  $c_{p_i}$ , for a mixture of thermally perfect gases is dependent upon the temperature of the mixture (1:388). Using curve fitted JANAF thermochemical data, the least squares coefficients of specific heats, enthalpy, and entropy parameters may be obtained as functions of temperature. In terms of the least squares coefficients,  $c_p$  is written as (13:56):

$$c_{p_i} = (a + bT + cT^2 + dT^3 + eT^4) R_{gas} C_i \quad (\text{B.13})$$

Enthalpy for a thermally perfect gas mixture is given by (1:397):

$$h = h_0 + \int_{T_0}^T C_p dT \quad (\text{B.14})$$

Substituting Eq. (B.13) into Eq. (B.14) yields the least squares coefficients form of enthalpy for species  $i$  (13:57):

$$h_i = \left[ (h_0 + aT + \frac{b}{2}T^2 + \frac{c}{3}T^3 + \frac{d}{4} + \frac{e}{5}T^5) R_{gas} + \frac{h_{T=298}}{MW} \right] C_i \quad (\text{B.15})$$

where  $h_{T=298}$  is the enthalpy of the species at the reference temperature of 298 K.

Entropy for a thermally perfect gas is given by (1:396):

$$\begin{aligned} s &= \int_{T_0}^T C_p \frac{dT}{T} - R \ln \frac{P}{P_0} \\ &= \phi - R \ln \frac{P}{P_0} \end{aligned} \quad (\text{B.16})$$

Again, substituting Eq. (B.13) into the integral portion of Eq. (B.16) yields the least squares coefficient form of the species entropy parameter,  $\phi_i$ , for a species  $i$  (13:57):

$$\phi_i = (\phi_0 + aT + \frac{b}{2}T^2 + \frac{c}{3}T^3 + \frac{d}{4}) R_{gas} C_i \quad (\text{B.17})$$

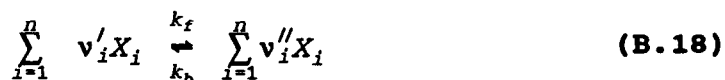
The total specific heat, enthalpy, and entropy of the thermally perfect mixture is then found from the summation of the individual species value. As implemented in the thermally perfect gas model (calorically imperfect), the chemical composition of the mixture remains constant, or frozen, throughout the nozzle.

#### B.4 Finite-Rate Chemically Reacting Flow

The finite-rate chemistry kinetics model accounts for a reacting mixture of gaseous species and the dissociation of gaseous molecules at high temperatures. Dissociation alters the molecular composition and molecular weight of the gaseous mixture and occurs around 2000 K for  $O_2$ , and begins

at 4000 K for  $N_2$  (1:451). The change in molecular composition and molecular weight alters the properties of the flow and the determination of flowfield properties downstream of discontinuities.

For a chemically reacting mixture of  $n$  different gaseous species,  $X_i$ , the general chemical reaction equation is:



where  $\nu_i'$  and  $\nu_i''$  are the stoichiometric coefficients of the reactants and products, respectively. The stoichiometric coefficients are positive for products and negative for reactants. The constants  $k_f$  and  $k_b$  are the forward and reverse reaction rate constants. The net rate of production of a given species  $i$  is given by (1:493):

$$\frac{d[X_i]}{dt} = (\nu_i'' - \nu_i') \left[ k_f \prod_i [X_i]^{\nu_i'} - k_b \prod_i [X_i]^{\nu_i''} \right] \quad (\text{B.19})$$

where  $[X_i]$  denotes the concentration of species  $i$  in moles per unit volume. The rate constants,  $k_f$  and  $k_b$ , are related by the equilibrium constant based on concentration,  $K_c$ , such that (1:493):

$$\frac{k_f}{k_b} = K_c \quad (\text{B.20})$$

where the concentration based equilibrium constant,  $K_c$ , can be found from the equilibrium constant based on partial

pressures,  $K_p$ , using the equation:

$$K_c = \left( \frac{1}{R_{univ}T} \right)^{\sum \nu_i} K_p \quad (\text{B.21})$$

The equilibrium constant based on partial pressures,  $K_p$ , for a given chemical reaction is determined from the Gibbs free energy and temperature (1:406):

$$K_p(T) = e^{-\Delta G^{p=1}/R_{univ}T} \quad (\text{B.22})$$

In Eq. (B.22)  $\Delta G^{p=1}$  is the Gibbs free energy of the products minus the Gibbs free energy of the reactants for a given chemical reaction with all species evaluated at a pressure of one atmosphere and a specified reference temperature (1:402-406). As implemented in the SCHNOZ computer program, values of  $G^{p=1}$  are determined from a thermodynamic datafile in the computer code.

The species concentration,  $[X_i]$ , in Eq. (B.19) can also be written as

$$[X_i] = \rho F_i \quad (\text{B.23})$$

where  $\rho$  is the density of the mixture and  $F_i$  is the mass fraction of species  $i$  divided by its molecular weight:

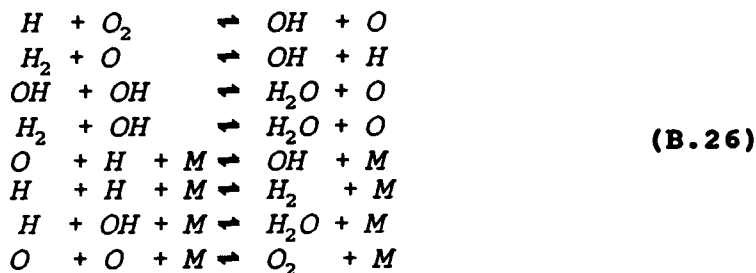
$$F_i = \frac{\alpha_i}{MW_i} \quad (\text{B.24})$$

The net production rate equation, Eq. (B.19), can then be written as



$$\dot{\lambda}_i \equiv \frac{d[X_i]}{dt} = k_f(v''_i - v'_i) \left[ \prod_i (\rho F_i)^{v'_i} - \frac{(R_{univ} T)^{\sum_i v_i}}{K_p} \prod_i (\rho F_i)^{v''_i} \right] \quad (B.25)$$

The chemical reactions implemented in the finite-rate chemistry model of the SCHNOZ code for this study are:



For the reactions considered in Eq. (B.26) M is a third body which can be a molecule of any species present in the mixture. The finite-rate chemistry model in the SCHNOZ code assumes that all third bodies have equal efficiencies in contributing to the reactions (15:2-9). The rate of production of a species i for the system is then the sum of the rates of production of species i for the individual reactions considered (1:496-497).

## *Appendix C: Flux-Difference-Splitting*

### *C.1 Introduction*

The flux-difference-splitting (FDS) method is a technique capable of capturing complicated flows with strong property gradients. The FDS method requires the solution of the Riemann problem at a given axial location to advance downstream in a marching fashion. FDS takes advantage of the wave-like nature of the Riemann problem to split the flow vector fluxes along preferred paths of propagation (6:153). Full details on the solution of the Riemann problem for planar supersonic flow assuming a thermally and calorically perfect gas are provided in reference (6). This solution procedure was modified for a calorically imperfect gas assumption in reference (13). The FDS method is independent of the Riemann problem solution method.

### *C.2 The Riemann Problem*

The Riemann problem is represented in Figure C.1. Godunov proposed that the general flow property,  $\Psi$ , distribution can be modelled as a series of uniform flow regions with a discontinuity occurring half-way between the nodes of interest (6:11). In Figure C.1 the solid line represents the arbitrary  $\Psi$  distribution and the dashed line represents the Godunov regions of uniform flow.

The collapse of the discontinuity to the midpoint,  $j+1/2$ , results in waves that are propagated along characteristics based on the wave angle (6:9) as depicted in Figure C.2. Waves (1) and (3) can be any combination of expansion or compression waves, and wave (2) is a contact surface that separates regions (2) and (4). Flow property discontinuities are present across the waves, however the contact surface, wave (2), cannot support a pressure nor flow angle discontinuity (6:163). The values of flow properties in regions (0) and (6) are known from the initial values or the solution of the previous Riemann problem.

### *C.3 Solution of the Riemann Problem*

The solution of the Riemann problem is the determination of the primitive flow variables,  $p$ ,  $\rho$ ,  $u$ , and  $v$ , in regions (2) and (4) as shown in Figure C.2. Doty (6) details three different methods that may be used to solve the Riemann problem. The first is an exact solution procedure where iterations of non-linear, coupled equations are required for a non-isentropic compression wave and iterations of the non-linear Prandtl-Meyer relations are necessary for simple expansions. Further iterations are required to match the pressure in regions (2) and (4) to satisfy the contact surface boundary. The second method is an exact-approximate solution. This is similar to the exact method but treats compression waves as isentropic. The

isentropic Prandtl-Meyer relations may then be used to solve for flow variables across any wave. The non-linear Prandtl-Meyer relations still require iterative solution techniques as well as further iterations of the entire solution to meet the contact surface pressure requirements. The third method is the linearized-approximate solution and is used exclusively in this study.

The linearized-approximate solution treats all waves as isentropic expansions and compressions which may be solved by the Prandtl-Meyer relations. Furthermore, the Prandtl-Meyer relations are linearized to allow for a closed form algebraic equation requiring no iterations. The linearized-approximate solution to the Riemann problem is dependent on the assumed thermodynamic model. The determination of the primitive variables in region (2) and (4) is more complicated for the calorically imperfect gas and requires an iterative technique for the solution of temperature .

### *C.3.1 Linearized-Approximate Solution, Perfect Gas*

For isentropic, planar, steady flow, the differential form of the compatibility relations, valid along Mach lines is (6:165):

$$\sqrt{M^2-1} \, dp \pm \rho V^2 d\theta = 0 \quad (C.1)$$

where the (+) sign refers to positive characteristics and the (-) sign refers to negative characteristics. Using the

definitions of velocity magnitude,  $V = u^2 + v^2$ , and flow angle,  $\theta = \text{atan}(v/u)$ , and the following relationship,  $\rho = \gamma p/a^2$ , Eq. (C.1) can be rearranged to yield:

$$\frac{dp}{p} \pm \frac{(\gamma u^2/a^2)}{\sqrt{M^2-1}} d(v/u) = 0 \quad (\text{C.2})$$

Introducing the following definitions:

$$z \equiv \frac{(\gamma u^2/a^2)}{\sqrt{M^2-1}} \quad (\text{C.3})$$

$$\sigma \equiv v/u \quad (\text{C.4})$$

$$d[\ln(p)] \equiv \frac{dp}{p} \quad (\text{C.5})$$

a more efficient form of the compatibility equations may be written as:

$$d[\ln(p)] \pm (z) d\sigma = 0 \quad (\text{C.6})$$

Linearizing Eq. (C.6) yields:

$$\Delta[\ln(p)] \pm (z) \Delta\sigma = 0 \quad (\text{C.7})$$

Referring to Figure C.2, a positive wave, wave (3), is required to pass information from region (0) to region (2). Using the (+) sign for the positive wave from Eq. (C.7) and using the regions (0) and (2) in the difference operator gives:

$$([\ln(p)]_2 - [\ln(p)]_0) + (z_0) (\sigma_2 - \sigma_0) = 0 \quad (\text{C.8})$$

Rearranging Eq. (C.8) yields:

$$[\ln(p)]_2 + (z_0)\sigma_2 = [\ln(p)]_0 + (z_0)\sigma_0 \quad (C.9)$$

Similarly, a negative wave is required to pass information from region (6) to (4) and from Eq. (C.7) is expressed by:

$$[\ln(p)]_4 - (z_6)\sigma_4 = [\ln(p)]_6 - (z_6)\sigma_6 \quad (C.10)$$

The pressure and flow angle (or slope,  $\sigma$ ) are required to match across the contact surface. Thus:

$$\sigma_4 = \sigma_2 \quad (C.11)$$

$$p_4 = p_2 \quad (C.12)$$

Equations (C.9), (C.10), (C.11), and (C.12) now constitute a set of four equations with four unknowns. After substitution and rearranging the four equations, an expression for the solution of the flow angle in region (4),  $\sigma_4$ , is obtained in terms of known properties in regions (0) and (6):

$$\sigma_4 = \frac{[\ln(p)]_0 - [\ln(p)]_6 + (z_6)\sigma_6 + (z_0)\sigma_0}{(z_6 + z_0)} \quad (C.13)$$

Equation (C.10) is then solved for  $p_4$ :

$$p_4 = \exp([\ln(p)]_6 + z_6(\sigma_4 - \sigma_6)) \quad (C.14)$$

The density and speed of sound in regions (2) and (4) are determined from isentropic ratios across waves (1) and (3):

$$\frac{\rho_2}{\rho_0} = \left[ \frac{P_2}{P_0} \right]^{1/\gamma} \quad (\text{C.15})$$

$$a_2 = [\gamma P_2 / \rho_2]^{1/2} \quad (\text{C.16})$$

$$\frac{\rho_4}{\rho_6} = \left[ \frac{P_4}{P_6} \right]^{1/\gamma} \quad (\text{C.17})$$

$$a_4 = [\gamma P_4 / \rho_4]^{1/2} \quad (\text{C.18})$$

Conservation of stagnation enthalpy across waves (1) and (3) is used to obtain the velocity components in regions (2) and (4). Recall from Appendix B that for a calorically perfect gas  $h = C_p T$ . Thus, across wave (3):

$$\frac{h_{t_4}}{h_{t_6}} = \frac{C_p T_{t_4}}{C_p T_{t_6}} = \frac{T_4 \left[ 1 + \frac{\gamma-1}{2} M_4^2 \right]}{T_6 \left[ 1 + \frac{\gamma-1}{2} M_6^2 \right]} = 1 \quad (\text{C.19})$$

Equation (C.19) can be solved explicitly for  $M_4$ ; and the velocity components, in terms of the flow slope,  $\sigma_4$ , are (13:62):

$$u_4 = M_4 a_4 \cos[\tan^{-1}(\sigma_4)] \quad (\text{C.20})$$

$$v_4 = M_4 a_4 \sin[\tan^{-1}(\sigma_4)] \quad (\text{C.21})$$

A similar procedure is used to find the primitive flow variables in region (2).

### C.3.2 Linearized-Approximate Solution, Imperfect Gas

The determination of the pressure in region (4), Eq. (C.14) remains valid for a calorically imperfect gas. To determine the remaining primitive flow variables a relation is needed that does not rely on a calorically perfect form of the conservation of stagnation enthalpy.

As outlined in reference (13), the determination of temperature uses relations that take advantage of the assumed isentropic nature of the flow. For a thermally perfect gas, the differential quantity of entropy in a system is (1:397):

$$ds = c_p \frac{dT}{T} - R \frac{dp}{p} \quad (\text{C.22})$$

Integration yields:

$$s = \int_{T_0}^T c_p \frac{dT}{T} - R \ln \frac{p}{p_0} = \phi - R \ln \frac{p}{p_0} \quad (\text{C.23})$$

where the entropy parameter,  $\phi$ , is defined as (13:63):

$$\phi = \int_{T_0}^T c_p \frac{dT}{T} \quad (\text{C.24})$$

Substituting Eq. (B.13) from Appendix B for the specific heat,  $C_p$ , for a mixture of gases, into Eq. (C.24) yields:

$$\phi = \left( \phi_0 + a \ln T + bT + \frac{cT^2}{2} + \frac{dT^3}{3} + \frac{eT^4}{4} \right) R \quad (\text{C.25})$$

A change in entropy across wave (3) is found from Eq. (C.23) and written in terms of the entropy parameters in regions



(4) and (6) as:

$$s_4 - s_6 = \phi_4 - \phi_6 - R \ln \left( \frac{p_4}{p_6} \right) \quad (\text{C.26})$$

For isentropic flow, Eq. (C.26) reduces to

$$\phi_4 = \phi_6 + R \ln \left( \frac{p_4}{p_6} \right) \quad (\text{C.27})$$

where  $\phi_6$  is found using Eq. (C.25) based on the known parameters in region (6). Once Eq. (C.27) is solved for  $\phi_4$ , Eq. (C.25) may be iteratively solved for the temperature,  $t$ . The thermal equation of state is then used to solve for the density in region (4).

The conservation of stagnation enthalpy is used in a different form than for the perfect gas to determine the velocity components in region (4). Conservation of stagnation enthalpy across wave (3) provides for the determination of the stagnation enthalpy in region (4):

$$h_{t_4} = h_6 + \frac{1}{2} (u^2 + v^2)_6 \quad (\text{C.28})$$

The static enthalpy,  $h_6$ , is a function of  $T_6$  and is found using the methods described in Appendix B and the velocity components,  $u_6$  and  $v_6$ , are known. Using the definition of the slope,  $\sigma = v/u$ , Eq. (C.28) can be rewritten as:

$$h_{t_4} = h_4 + \frac{1}{2}u_4^2(1+\sigma_4^2) \quad (C.29)$$

Solving for the axial velocity component in region (4),  $u_4$  gives:

$$u_4 = \sqrt{\frac{2(h_{t_4}-h_4)}{1+\sigma_4^2}} \quad (C.30)$$

The radial component of velocity,  $v_4$ , is then computed using the slope in region (4):

$$v_4 = u_4\sigma_4 \quad (C.31)$$

The Mach number is then computed :

$$M_4 = \frac{V_{mag}}{a_4} \quad (C.32)$$

#### C.4 Riemann Fluxes

After solving the Riemann problem, the primitive variables are combined to form the Riemann flux vectors in regions (0), (2), (4), and (6) (6:171). The **E** and **F** flux vectors are presented in section 3.1 and are repeated here for convenience.

$$\mathbf{E} = \begin{bmatrix} \rho u \\ \rho u^2 + p \\ \rho uv \\ u(\rho e + p) \end{bmatrix}, \quad \mathbf{F} = \begin{bmatrix} \rho v \\ \rho vu \\ \rho v^2 + p \\ v(\rho e + p) \end{bmatrix} \quad (C.33)$$

The Riemann fluxes are calculated for each of the components of the **E** and **F** vectors. For example, the first component of

the **E** vector,  $E1$  is  $\rho u$  and is computed in each of the Riemann regions (0), (2), (4), and (6):

$$(E1)_0 = \rho_0 u_0 \quad (C.34)$$

$$(E1)_2 = \rho_2 u_2 \quad (C.35)$$

$$(E1)_4 = \rho_4 u_4 \quad (C.36)$$

$$(E1)_6 = \rho_6 u_6 \quad (C.37)$$

The remaining Riemann flux vector components are found in a similar manner.

#### C.5 Calculation of the Flux Differences

The Riemann flux differences are the differences in the Riemann flux vector components taken across waves (1), (2) and (3). For example, the difference of the Riemann fluxes for the first component of the **E** vector,  $dE1$ , across waves (1), (2) and (3) are:

$$(dE1)_{\text{wave1}} = (E1)_2 - (E1)_0 \quad (C.38)$$

$$(dE1)_{\text{wave2}} = (E1)_4 - (E1)_2 \quad (C.39)$$

$$(dE1)_{\text{wave3}} = (E1)_6 - (E1)_4 \quad (C.40)$$

The sum of the total contributions across all three waves gives the total contribution at the midpoint of the Riemann region, node  $j+1/2$  (6:182):

$$(dE1)_{j+1/2} = [(dE1)_{\text{wave3}} + (dE1)_{\text{wave2}} + (dE1)_{\text{wave1}}]_{j+1/2} \quad (C.41)$$

The remaining Riemann flux vector components are computed in a similar manner.

#### *C.6 Splitting the Flux Differences*

Referring to Figure C.3 the information is known at node  $j$  on axial plane  $i$ , and the solution is sought downstream at node  $j$  on axial plane  $i+1$ . The solution of the Riemann problem calculated the fluxes at the midpoints  $j+1/2$  and  $j-1/2$ . The Riemann flux differences were calculated and are now split along their direction of propagation to determine which information from Riemann nodes  $j+1/2$  and  $j-1/2$  will reach node  $j$  at plane  $i+1$ .

Following the method detailed by Doty (3:183-186) the flux differences are propagated in a direction determined by streamlines and characteristics. At node  $j+1/2$ , if the slope of waves (1), (2), or (3) is negative, the Riemann flux differences across those waves contribute to the solution at the downstream node  $(i+1, j)$  (6:185). Conversely, at node  $j+1/2$ , if the slope of waves (1), (2), or (3) is positive, the Riemann flux differences across those waves do not contribute to the solution at  $(i+1, j)$  but, would contribute to the solution at node  $(i+1, j+1)$ . Similarly, at Riemann node  $j-1/2$ , if the slope of waves (1), (2), or (3) is positive, The Riemann flux differences across those waves contribute to the solution at node  $(i+1, j)$ . The Riemann flux differences are essentially split

into positive and negative contributions at each Riemann node.

The contributions at the downstream node (i+1,j) are found by summing the positive contributions of the Riemann flux differences from node j-1/2 and the negative contributions of the Riemann flux differences from node j+1/2:

$$dE_{j+1/2}^- = [dE_{j+1/2}^{wave3}]^- + [dE_{j+1/2}^{wave2}]^- + [dE_{j+1/2}^{wave1}]^- \quad (C.42)$$

$$dE_{j-1/2}^+ = [dE_{j-1/2}^{wave3}]^+ + [dE_{j-1/2}^{wave2}]^+ + [dE_{j-1/2}^{wave1}]^+ \quad (C.43)$$

where the positive or negative signs denote positively or negatively sloped flux differences. It is possible that all, some, or none of the Riemann flux differences at a Riemann midpoint node may contribute to the downstream solution at a Riemann node, depending on their characteristic slope. The same procedure is applied to the  $\mathbf{F}$  vector. Further details on the splitting of the flux differences are presented in Appendix J of reference (6).

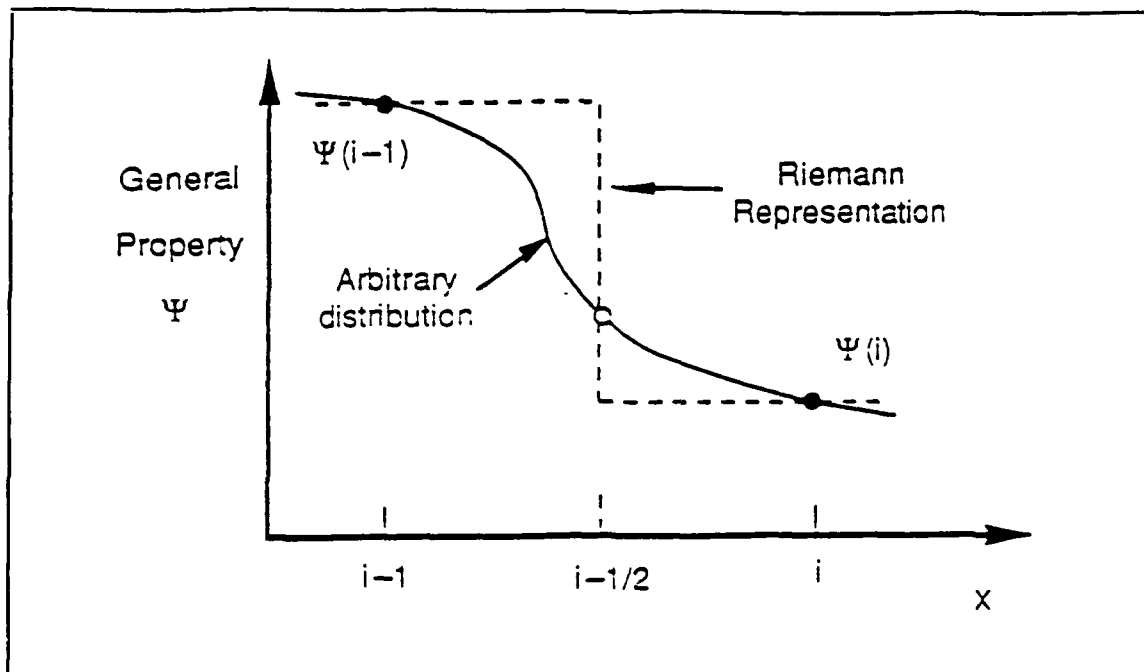


**Figure C.1.** General property distribution and Riemann description (6:135).

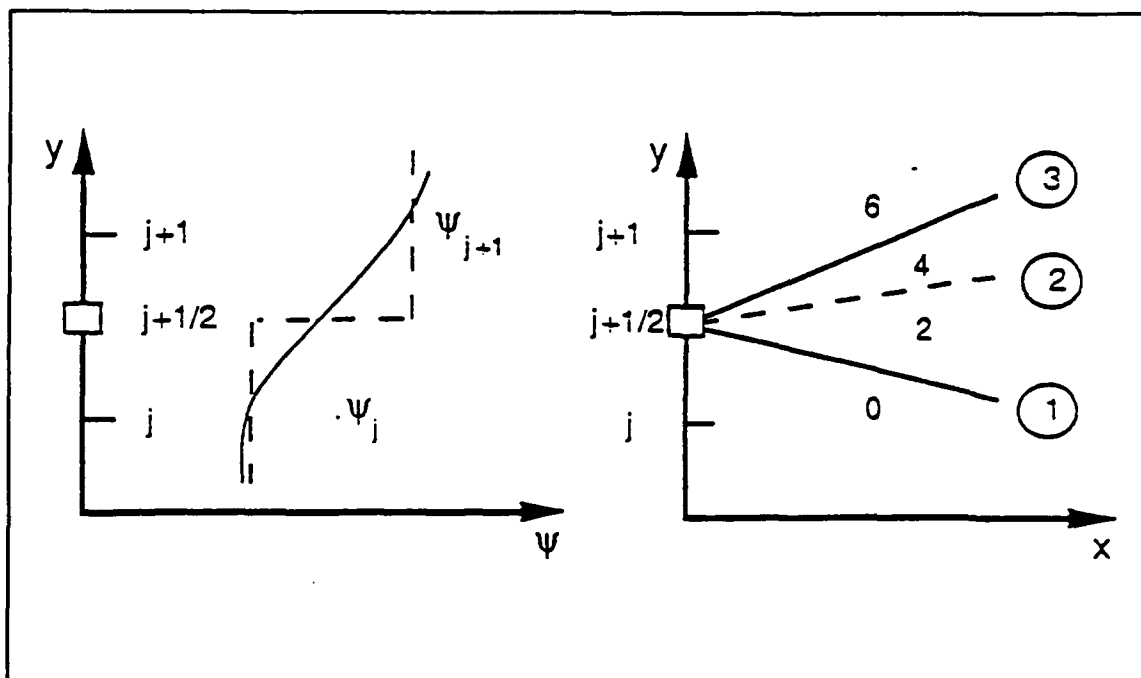


**Figure C.2.** Riemann problem for planar supersonic flow and resulting wave pattern (6:174).

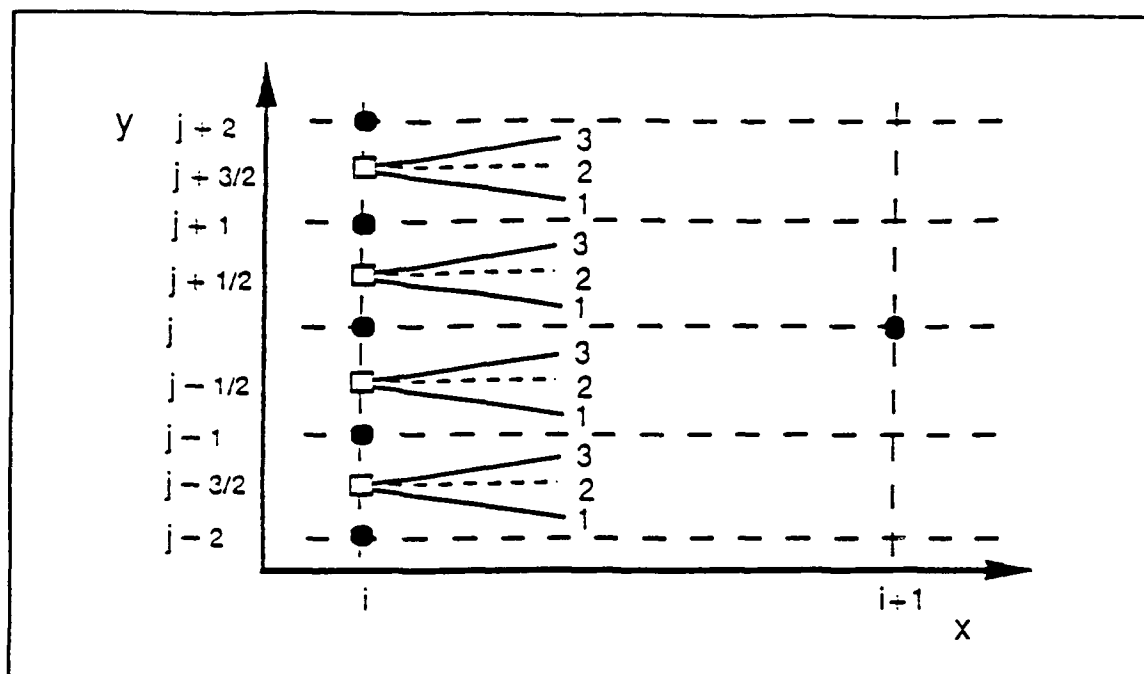


**Figure C.3.** Flux differences and splitting (6:187).

## *Appendix D: FDS Decode Procedures*

### *D.1 Introduction*

The upwind FDS algorithm solves the downstream **E** and **F** flux vectors based on the solution of the Riemann problem generating Riemann fluxes that are then split along their physically correct path of propagation as discussed in Appendix C. To continually march the solution from plane  $i$  to  $i+1$  the values of the primitive variables are required at each plane to solve the Riemann problem. A decode procedure is required at each axial plane to extract the primitive variables from the calculated flux vectors. This decode procedure is dependent upon the thermodynamic model utilized in the flowfield solution.

### *D.2 Perfect Gas Decoding*

The perfect gas decode procedure is detailed in reference (6) and summarized herein. The four components of the **E** vector,  $E_1$ ,  $E_2$ ,  $E_3$ , and  $E_4$ , are known from the spatial marching of the FDS algorithm. The decoding of the **E** vector, see Eq. (3.2), requires the simultaneous solution of five equations for the five unknowns  $\rho$ ,  $u$ ,  $v$ ,  $p$ , and  $e$  contained in the **E** flux vector.

The  $\rho e$  term contained in the  $E_4$  component can be written in terms of the internal energy and flow energy:



$$\rho e = \rho \hat{u} + \frac{1}{2} \rho (u^2 + v^2) \quad (D.1)$$

For a perfect gas the specific internal energy,  $\hat{u}$ , is written as (1:388):

$$\hat{u} = c_v T \quad (D.2)$$

where  $c_v$  for a perfect gas can be written in terms of the gas constant,  $R$ , and the ratio of specific heats,  $\gamma$ , as:

$$c_v = \frac{R}{\gamma - 1} \quad (D.3)$$

Using the thermal equation of state and the relations for  $\hat{u}$  in Eq. (D.2) and  $c_v$  in Eq. (D.3), the expression for the term  $\rho e$  in Eq. (D.1) can be rewritten as:

$$\rho e = \frac{p}{\gamma - 1} + \frac{1}{2} \rho (u^2 + v^2) \quad (D.4)$$

Using Eq. (D.4) for the  $\rho e$  term, the E4 component is given by:

$$E4 = u \left[ \left( \frac{p}{\gamma - 1} + \frac{1}{2} \rho (u^2 + v^2) \right) + p \right] \quad (D.5)$$

Expanding Eq. (D.5) and rearranging yields:

$$E4 = u p \left[ \frac{\gamma}{\gamma - 1} \right] + \frac{1}{2} \rho u (u^2 + v^2) \quad (D.6)$$

The E2, E3, and E4 components can be written in terms of the E1 component,  $\rho u$ , to give:

$$E2 = (E1) u + p \quad (D.7)$$

$$E3 = (E1) v \quad (D.8)$$

$$E4 = u \left[ \frac{\gamma}{\gamma-1} \right] + \frac{1}{2} (E1) (u^2) + \frac{1}{2} (E1) (v^2) \quad (D.9)$$

Solving Eq. (D.8) for the radial velocity,  $v$ , gives:

$$v = \frac{E3}{E1} \quad (D.10)$$

Similarly, Eq. (D.8) can be solved for the pressure,  $p$ :

$$p = E2 - (E1) u \quad (D.11)$$

Eqs. (D.10) and (D.11) can now be substituted into the  $E4$  component equation, Eq. (D.9) to yield an expression that is solely a function of the known  $E$  vector components and one unknown,  $u$ :

$$E4 = u \left[ \frac{\gamma}{\gamma-1} \right] \left[ (E2) - (E1) u + \frac{1}{2} (E1) (u^2) + \frac{1}{2} (E1) \left[ \frac{E3}{E1} \right]^2 \right] \quad (D.12)$$

Casting this expression as a quadratic equation yields:

$$\left[ \frac{\gamma+1}{2(\gamma-1)} (E1) \right] u^2 - \left[ \frac{\gamma}{\gamma-1} (E2) \right] u + \left[ (E4) - \frac{1}{2} \frac{(E3)^2}{(E1)} \right] = 0 \quad (D.13)$$

This quadratic equation is then used to find the value of the axial velocity,  $u$ :

$$u = \frac{-b + \sqrt{b^2 - 4ac}}{2a} \quad (D.14)$$

where:

$$a = \frac{\gamma+1}{2(\gamma-1)} (E1) \quad (D.15)$$

$$b = \frac{\gamma}{\gamma-1} (E2) \quad (D.16)$$

$$c = (E4) - \frac{1}{2} \frac{(E3)^2}{(E1)} \quad (D.17)$$

The remaining primitive flow variables are then found from:

$$v = \frac{E3}{E1} \quad (D.18)$$

$$p = E2 - (E1) u \quad (D.19)$$

$$\rho = \frac{E1}{u} \quad (D.20)$$

$$\rho e = \frac{p}{\gamma-1} + \frac{1}{2} \rho (u^2 + v^2) \quad (D.21)$$

The perfect gas decode procedure is then complete.

### D.3 Imperfect Gas Decoding

The imperfect gas decode procedure development follows the procedure presented in reference (13). The difference in the decoding of the  $E$  vector for the calorically imperfect gas is that the internal energy term,  $\rho e$ , in the  $E4$  component must be consistent with the imperfect gas assumption (13:75). Specific internal energy,  $\hat{u}$ , for the calorically imperfect gas is given by (1:395):

$$\hat{u} = h - RT \quad (D.22)$$

The total internal energy for the imperfect gas is then found by substituting Eq. (D.22) into the  $\rho e$  expression, Eq. (D.1) to yield:

$$\rho e = \rho h - p + \rho \frac{1}{2} (u^2 + v^2) \quad (D.23)$$

Substituting Eq. (D.23) into the E4 component gives:

$$E4 = \rho u h + \frac{1}{2} \rho u (u^2 + v^2) \quad (D.24)$$

Substituting the E1 component,  $\rho u$ , and the E3 component,  $\rho u v$ , into Eq. (D.24) gives the following form of the E4 component:

$$E4 = h(E1) + \frac{1}{2} (E1) u^2 + \frac{1}{2} \frac{(E3)^2}{E1} \quad (D.25)$$

Eq. (D.25) is now a function of the axial velocity,  $u$ , and the enthalpy,  $h$ . The enthalpy is a function of temperature which is determined from the least squares coefficient as discussed in Appendix B. The thermal equation of state, which is still valid for the calorically perfect gas, and the E1 component are combined to yield an expression for  $u$ :

$$u = \frac{(E1) RT}{p} \quad (D.26)$$

Solving the E2 component for  $p$  and substituting the result into Eq. (D.26) yields:

$$u = \frac{(E1) RT}{E2 - (E1) u} \quad (D.27)$$

Rearranging Eq. (D.27) a quadratic for u is developed:

$$(E1) u^2 + (E2) u + (E1) RT = 0 \quad (D.28)$$

which when solved for u yields:

$$u = \frac{E2 + \sqrt{(E2)^2 - 4(E1)((E1)RT)}}{2(E1)} \quad (D.29)$$

The E4 component is now a function only of temperature with both h and u dependent on the temperature value. The temperature, T, is found iteratively using the secant method and Eqs. (D.28) and (D.29) (13:77).

Once the temperature is determined, u is determined from the quadratic relation. The remaining primitive variables are found using the perfect gas decode procedure of Eqs. (D.18) - (D.21).

## *Vita*

Kennedy Boyd Wilson, Jr. was born on June 15, 1965, in Lincoln, Nebraska. He graduated from Manzano High School in Albuquerque, New Mexico in 1983, and attended the U.S. Air Force Academy, graduating with a Bachelor of Science in Engineering Sciences in May 1987. Upon graduation he received a regular commission in the USAF and began his first tour of duty at the NASA Lewis Research Center in Cleveland, Ohio. He worked as an Operations Engineer in the 10' by 10' Supersonic Wind Tunnel. In September 1989, he began his next assignment at the Arnold Engineering Development Center, Arnold AFB, in Tullahoma, Tennessee where he was the Operations Manager for the Engine Test Facility. He entered the School of Engineering, Air Force Institute of Technology, in June 1991.

Permanent Address: 1901 Buffalo Dancer Tr., NE  
Albuquerque, NM 87112

REPORT DOCUMENTATION PAGE			Form Approved OMB No. 0704-0188	
Public reporting burden for this collection of information is estimated to average 1 hour per response, including the time for reviewing instructions, searching existing data sources, gathering and maintaining the data needed, and completing and reviewing the collection of information. Send comments regarding this burden estimate or any other aspect of this collection of information, including suggestions for reducing this burden, to Washington Headquarters Services, Directorate for Information Operations and Reports, 1215 Jefferson Davis Highway, Suite 1204, Arlington, VA 22202-4302, and to the Office of Management and Budget, Paperwork Reduction Project (0704-0188), Washington, DC 20503.				
1. AGENCY USE ONLY (Leave blank)	2. REPORT DATE December 1992	3. REPORT TYPE AND DATES COVERED Master's Thesis		
4. TITLE AND SUBTITLE A COMPARISON OF COMPUTATIONAL FLUID DYNAMICS COMPUTER PROGRAMS FOR HYPERSONIC PROPULSIVE NOZZLE FLOWFIELDS		5. FUNDING NUMBERS		
6. AUTHOR(S) Wilson, Kennedy B. Jr., Captain, USAF				
7. PERFORMING ORGANIZATION NAME(S) AND ADDRESS(ES) Air Force Institute of Technology Wright-Patterson AFB, Ohio		8. PERFORMING ORGANIZATION REPORT NUMBER AFIT/GAE/ENY/92D-27		
9. SPONSORING / MONITORING AGENCY NAME(S) AND ADDRESS(ES)		10. SPONSORING / MONITORING AGENCY REPORT NUMBER		
11. SUPPLEMENTARY NOTES				
12a. DISTRIBUTION / AVAILABILITY STATEMENT Approved for public release; distribution unlimited		12b. DISTRIBUTION CODE		
13. ABSTRACT (Maximum 200 words)  This study compared the results of two computer programs, a flux-difference-splitting (FDS) Godunov-based scheme and the SCRAMjet Hypersonic Nozzle (SCHNOZ) paraabolized Navier-Stoke's code using MacCormack's method, applied to a hypersonic nozzle flowfield. Two different nozzle geometries were investigated at three Mach numbers along a typical hypersonic flight trajectory. A direct compariosn between the SCHNOZ and FDS programs was made by numerically solving the steady Euler equations using a frozen flow assumption in the nozzle. The frozen flow SCHNOZ code is currently 6 to 10 times more efficient in terms of computational time than the FDS frozen flow code. The SCHNOZ and FDS codes demonstrated comparable accuracy in modeling the flow physics. The implememntation of the viscous terms in the SCHNOZ code proved to be ineffectual in modeling the viscous effects in the flowfield. The finite-rate chemistry effects were important for the nozzle inlet conditions considered.				
14. SUBJECT TERMS Hypersonic Nozzle, SCRAMjet, NASP, Riemann Problem, Flux-Difference-Splitting, Thermodynamic Model, Hypersonic Propulsion			15. NUMBER OF PAGES 127	
			16. PRICE CODE	
17. SECURITY CLASSIFICATION OF REPORT Unclassified	18. SECURITY CLASSIFICATION OF THIS PAGE Unclassified	19. SECURITY CLASSIFICATION OF ABSTRACT Unclassified	20. LIMITATION OF ABSTRACT UL	